Technical University of Denmark

DTU

New Materials for Hydrogen Evolution

Bonde, Jacob Lindner; Chorkendorff, Ib

Publication date:
2008

Document Version
Early version, also known as pre-print

Link back to DTU Orbit

Citation (APA):
Bonde, J. L., & Chorkendorff, I. (2008). New Materials for Hydrogen Evolution.

DTU Library
Technical Information Center of Denmark

New Materials for Hydrogen Evolution

Ph.D. Thesis
April 2008

Jacob L. Bonde

Center for Individual Nanoparticle Functionality (CINF)
Department of Physics
Technical University of Denmark

Preface

This thesis is submitted in partial fulfillment of the requirements for the Ph.D. degree from the Technical University of Denmark. The project has been carried out at the Institute of Physics at the Technical University of Denmark, within the Interdisciplinary Center for Catalysis, ICAT and Center for Individual Nanoparticle Functionality, CINF, during the last three years under the supervision of Professor Ib Chorkendorff. Financial support was provided by the Danish Strategic Research foundation.

I would like to thank Professor Ib Chorkendorff for inspiring discussions, for making it possible to venture into the field of electrochemistry and for having a such close collaboration with the theory group of Jens K. Nørskov. Especially I would like to thank the former and current members of the electrochemistry group, Assistant Professor Thomas F. Jaramillo, Post doc. Billie Abrams and Ph.D student Peter Vesborg for inspiring discusssions ranging from electrochemistry and materials science to the next planned social activity.

In connection with the build and many iterations of improving the electrochemistry lab I enjoyed the help and support of Technician John Larsen as well as Hans Christian Sørensen and Dan Schacam.

I also thank Billie Abrams, Klas Andersson and Peter Vesborg who helped to proof read this thesis.

The current and former members of ICAT,CINF,CAMD and CAMP over the years are also thanked for, not only, providing a strong basis for scientific discussion, but also for giving work an important social aspect. Finally I would like thank my beloved wife Josephine and my son Tobias for their loving support.

<div align="center">

Jacob Lindner Bonde
København, April 4th, 2008

</div>

Abstract

This thesis primarily deals with the identification and electrochemical characterization of materials for the hydrogen evolution reaction, where protons and electrons combine to form hydrogen.

Based on computational screening, a BiPt surface alloy was identified as being a potential HER candidate. The BiPt surface alloy was synthesized and identified as being more active for the HER than Pt. A core shell system composed of a Pt skin on an Au core was also investigated and found to have a HER activity that could be increased or decreased depending on the potentials previously applied to the sample.

MoS_2 nanoparticles were identified as being promising HER catalysts. Further investigations on MoS_2 on Au(111) imaged by scanning tunneling microscopy(STM) proved that the active site of these particles was the edge and enabled the quantification of the HER activity. Carbon supported MoS_2 and WS_2 nanoparticles were synthesized and found to have HER activities close to that of Au(111) supported MoS_2. The effect of cobalt promotion of WS_2 and MoS_2 was also investigated and Co was found to promote the HER activity.

Finally Mo_3S_4 clusters were found to catalyze the HER and electrochemical characterization of STM preimaged samples allowed for the quantification of the turn over frequency per Mo_3S_4 cluster.

Resumé

Denne afhandling omhandler primært identifikation og elektrokemisk karakterisering af materialer til brint evolutions reaktionen, hvor protoner og elektroner kombineres til brint.

En computerbaseret screening identificerede en platin bismuth overfladelegering, som værende en potentiel brint evolutions katalysator. Platin bismuth overfladelegeringen blev syntetiseret og identificeret som værende en mere aktiv brint evolutions katalysator end rent platin. Nanopartikler med en kerne af guld og en skal af platin blev også undersøgt. Det blev vist at brintevolutionsaktiviteten kunne hæves og sænke alt efter hvilket elektrokemisk potentiale partiklerne havde set før aktivitets målingen blev foretaget.

MoS_2 nanopartikler blev også identificeret som værende lovende brint evolutions katalysatorer. Senere elektrokemiske målinger på MoS_2 på Au(111) som var blevet afbilledet med et scanning tunneling mikroskop(STM). Besviste at partiklernes kant var aktive del af partiklen. Dette muliggjorde en kvantifisering af evnen til at udvikle brint.

MoS_2 og WS_2 på et kul bæremateriale blev også synthetiseret og aktiviteten for brintudviklingsaktiviteten var sammenlignelig med aktiviteten af MoS_2 på Au(111). Effekten af kobolt promovering af MoS_2 og WS_2 blev også undersøgt og tilsætingen af kobolt viste sig at have en promoverende effekt.

Sidst blev det vist Mo_3S_4 molekuler kunne katalysere brint evoluiotns reaktionen og elektrokemisk karakterisering af STM afbilledede Mo_3S_4 partikler gjorde det muligt at kvantifisere aktiviteten pr. molekule.

Included Publications

Paper 1:
"Biomimetic Hydrogen Evolution"
B. Hinneman, P. G. Moses, J. Bonde, K. P. Jørgensen, S. Horch, J. H. Nielsen , I. Chorkendorff and J.K. Nørskov,
Journal of the American Chemical Society , **127**, 5308 (2005)

Paper 2:
"Computational high-throughput screening of electrocatalytic materials for hydrogen evolution" J. Greeley, T. F. Jaramillo, J. Bonde, I. Chorkendorff and J. K. Nørskov,
Nature Materials, **5**, 909 (2006)

Paper 3:
"Identification of Active Edge Sites for Electrochemical H_2 Evolution from MoS_2 Nanocatalysts"
T. F. Jaramillo, K. P. Jorgensen, J. Bonde, J. H. Nielsen, S. Horch and I. Chorkendorff,
Science, **316**, 100 (2007)

Paper 4:
"Hydrogen Evolution on Nano-particulate Transition Metal Sulfides"
J. Bonde, P. G. Moses, T. F. Jaramillo, J. K. Nørskov and I. Chorkendorff,
Accepted Faraday Discussions, (2008)

Paper 5:
"Hydrogen Evolution on supported incomplete cubane-type $[Mo_3S_4]^{4+}$ electrocatalyst"
T. F. Jaramillo, J. Bonde, J. Zang, B. L. Ooi, J. Ulstrup and I. Chorkendorff,
Submitted Journal of Physical Chemistry C, (2008)

Contents

Chapter 1

Introduction

In recent years the focus on renewable energy sources have been significantly increased due to increasing oil prices and the growing concern for global warming.

Currently the moment most of the world's energy consumption is fossil fuel based, but there is a growing interest in replacing the fossil fuels with renewable resources like solar, wind and biomass. Increasing the amount of renewable energy is not a simple task as renewable energy sources like sun and wind do not provide a stable supply of energy, since the energy is produced when the sun shines or when the wind blows.

One way of stabilizing the energy supply is to use different energy carriers that can be produced when there's a surplus of renewable energy and used when there's a lack of renewable energy. One suggested energy carrier is hydrogen[1] which can be produced from water by electrolysis and made into power, heat and water in a fuel cell.

The catalysts used in for instance fuel cells are usually based on platinum or platinum ruthenium alloys, these catalysts are both scarce and expensive. Only 200 tons of platinum is mined every year[2] and as current state of the art fuel cells use on the order of 1 gram of platinum pr kW of power[3], this corresponds to the platinum needed to produce 2 million cars pr. year each equipped with a 100 kW engine.

The aim of this project is to find and characterize alternative materials for the hydrogen evolution reaction(HER) where protons and electrons recombine to form hydrogen.

$$2H^+ + 2e^- \rightarrow H_2 \tag{1.1}$$

The hydrogen evolution reaction is one of the most studied electrochemical reactions and is often used as the textbook example[4] on the relation between kinetics and surface properties of electrodes. The HER is not only

interesting from a scientific point of view, due to its commercial importance for use in electrolyzers producing hydrogen.

The outline of this thesis is as follows. Chapter 2 will give a brief overview of the relation between electrochemstry and catalysis, followed by and overview of electrocatalyssis with the emphasis electrocatalytic hydrogen evolution. Chapter 3 will be description of the electrochemical methods and the setups used. Chapter 4 is a short description of some the approaches that can lead to a reduction in the use of platinum. Chapter 5 is an overview of the Pt based systems that were investigated during the work on this thesis. Chapter 6 gives an overview of the metal sulfides investigated and the results of the electrochemical investigations of these systems. Finally I have attached the published and submitted papers that where written during this Ph.D study.

Chapter 2

Electrocatalysis

The insight into heterogeneous catalysis has increased tremendously in re-cents years, due to investigations of well defined model systems combined with theoretical DFT calculations. This has revealed the nature of both rate limiting steps and sites governing the overall activity for many differ-ent systems. With these trends it is now possible to make computational screening for new materials with higher activity, selectivity and/or stability and successful screening studies have already been reported [5, 6, 7]. Re-cently theoretical calculations and detailed studies of model systems have also been used in the field of electrocatalysis both for detailed studies of reaction pathways[8] and for the study of activity descriptors[9, 10, 11, 12].

2.1 Electrochemistry and catalysis

Just as in heterogeneous catalysis, electrocatalysis involves converting reac-tants into products without loss of the catalyst. But in electrocatalysis it is possible to drive a reaction out of equilibrium by means of the addition or subtraction of charge. In the following some basic equations relevant for the hydrogen evolution reaction will be derived, more detailed discussions about the derivation and the basics of electrode kinetics can be found in reference[4].
The electrode can transfer charge to or from a reactant. One simple exam-ple is changing the oxidation state of ions in a solution by means of a metal electrode as follows:

$$X^{3+}(aq) + e^-(electrode) \rightarrow X^{2+}(aq) \tag{2.1}$$
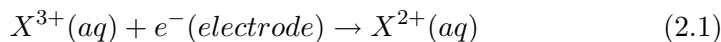
The current for this reaction will then be given by:

$$i = AFk_0c_X{}^{3+} \tag{2.2}$$

3

Where A is the area of the electrode, F is Faraday's constant k_0 is the rate of electron transfer and $c_{X^{3+}}$ is the concentration of the reactant. The current is limited by the concentration of the reactants or the rate of electron transfer. The latter can controlled by applying a potential to the electrode. But in reality an electrochemical reaction can be in equilibrium and the reaction in question can have an activation barrier, just as in heterogeneous catalysis[13]. In general the relation between a potential and an activation barrier is given by:

$$\Delta E = -\frac{\Delta G}{nF} \quad (2.3)$$

Where ΔE is the electrode potential, n is the number of electrons transferred and ΔG is the the free energy of the activation barrier. As the potential of an electrode is a function of the current density drawn, the therm overpotential is defined as being the difference in electrode potential at equilibrium(E_e) and the potential at a given current density(E_i) :

$$\eta = E_i - E_e \quad (2.4)$$

Thus the potential of an electrode should be defined by the change in standard free energy ΔG_0 and the overpotential η as:

$$\Delta V = \Delta G_0 \pm \eta \quad (2.5)$$

In reality however the relation between potential and free energy is not that simple. There are many other sources that affect the potential such as: ohmic drop, diffusion limitations, stability of the material, etc. An important parameter in electrochemistry is the transfer coefficient determining the amount of charge transferred by means of an overpotential. Thus the change in activation energy pr. electron for a given process as function of overpotential is given by:

$$\Delta E = -nF\eta \quad (2.6)$$

In heterogeneous catalysis the rate of a reaction which is equivalent to the current density can be described by an Arrhenius type equation given by:

$$k = \nu e^{\frac{-E_a}{k_b T}} \quad (2.7)$$

k is the rate constant, ν is the prefactor and E_a is the activation energy. If we assume that we have a reversible reaction, such as the oxidation and reduction of an Fe ion, we will have a net rate given by:

$$r = k_c c_O - k_a c_R \quad (2.8)$$

Where k_c is the rate constant for oxidation(anodic) and k_a is the rate constant for reduction(cathodic), c_R and c_O is the concentration of the species

being reduced or oxidized respectively. If we assume that both the oxidation and the reduction reactions are activated by the free energies of ΔG_c and ΔG_a respectively. Then the rate constant for the oxidation and the reduction will be given by:

$$k_c = \nu e^{\frac{-\Delta G_c}{RT}} \tag{2.9}$$

$$k_a = \nu e^{\frac{-\Delta G_a}{RT}} \tag{2.10}$$

In electrochemistry it is possible to change the activation barrier by adding the overpotential η multiplied with the transfer coefficient α. Thus the free energy activation barriers will be:

$$\Delta G_c = \Delta G_{c,eq} + \alpha_c n_e F \eta \tag{2.11}$$

$$\Delta G_a = \Delta G_{a,eq} - \alpha_a n_e F \eta \tag{2.12}$$

$\Delta G_{c,eq}$ and $\Delta G_{a,eq}$ are asummed to be the potential independent activation barriers at equilibrium and $\alpha_c + \alpha_a = 1$. The rate constants for the oxidation and the reduction will be given by:

$$k_c = \nu e^{\frac{-\Delta G_{c,eq} - \alpha_c n_e F \eta}{RT}} \tag{2.13}$$

$$k_a = \nu e^{\frac{-\Delta G_{a,eq} + \alpha_a n_e F \eta}{RT}} \tag{2.14}$$

If we introduce a new constant k_0 wich includes all the parameters that are assumed to be potential independent and assume that the prefactors and activation barriers for the different rate constant are equal. Then the rate constants are given by:

$$k_c = k_0 e^{\frac{-\alpha_c n_e F \eta}{RT}} \tag{2.15}$$

$$k_a = k_0 e^{\frac{\alpha_a n_e F \eta}{RT}} \tag{2.16}$$

The rate constants can now be inserted in equation 2.8 and the net rate equation becomes:

$$r = \frac{i}{n_e F} = k_0 (c_O e^{\frac{-\alpha_c n_e F \eta}{RT}} - c_R e^{\frac{\alpha_a n_e F \eta}{RT}}) \tag{2.17}$$

If we convert the rate into current and introduce the exchange current density $i_0 = k_0 n_e F$ we have the classical Butler Volmer equation:

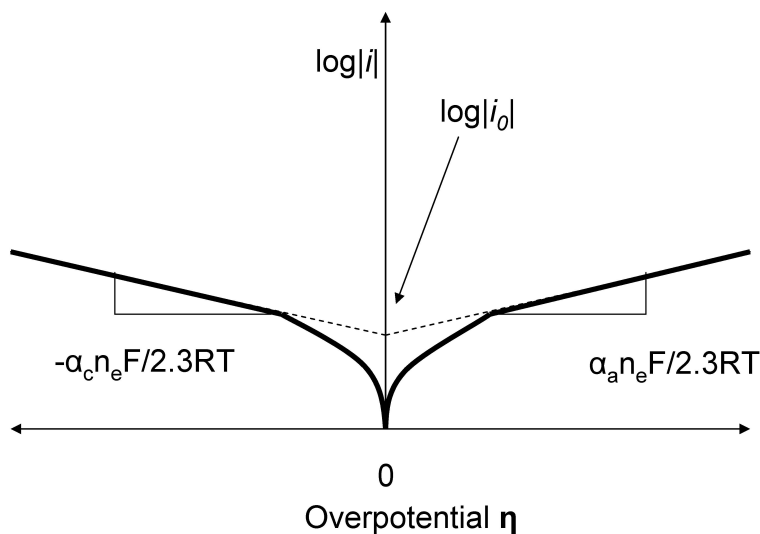$$i = i_0 (c_O e^{\frac{-\alpha_c n_e F \eta}{RT}} - c_R e^{\frac{\alpha_a n_e F \eta}{RT}}) \tag{2.18}$$

Figure 2.1: Tafel plot where $log|i|$ is plotted as a function of the overpotential. The slope in the linear region is the inverse of the Tafel slope. If the linear region is extrapolated to zero overpotential the exchange current density i_0 is given by the intercept with the y-axis.

The Butler Volmer equation is often used to analyze the kinetics and thermodynamics of electrochemical reactions by means of Tafel analysis. The Tafel analysis is used when the reaction is out of equilibrium, meaning that either the anodic or the cathodic current is dominating the current density measured. The logarithm of the current density $log|i|$ can then be plotted as a function of the overpotential η (See Fig. 2.1). This plot can then be used to evaluate the overpotential η as a function of the current density in the linear region of the Tafel plot given by:

$$\eta = a + blog|i| \tag{2.19}$$

Where a is $log|i_0|$ and b is the Tafel slope given by:

$$b = \frac{2.3RT}{\alpha_c n_e F} \tag{2.20}$$

This simple analysis gives two parameters the exchange current density i_0 and the Tafel slope $\frac{2.3RT}{\alpha_c n_e F}$. The exchange current density is comparable to the rate constants used in heterogeneous catalysis and just as in heterogeneous catalysis it is governed both by kinetics and thermodynamics. The Tafel slope gives information on both the kinetics and the thermodynamics. It is often used as a fingerprint showing whether or not the individual measurements are dominated by transport limitations. The Tafel slope is governed by the temperature T and the number of electrons per. unit re-

action n_e and the transfer coefficient *alpha*. If we assume that $\alpha = 0.5$ and that $n_e = 1$ the Tafel slope at 298.15 K is expected to be:

$$\frac{2 \cdot 2.3RT}{F} = 118mV/dec \tag{2.21}$$

If the measured Tafel slope is higher it is difficult to determine the exact reason for the discrepancy as it could be transport/diffusion limitations, cell resistance or that the proposed mechanism is not not the correct one. Since the Tafel slope parameters α and n_e are multiplied it is difficult to determine the exact values of α and n_e from the slope alone.

As the Tafel slope and the exchange current density are linked, a wrongly measured Tafel slope can influence the extrapolated exchange currents density. A high Tafel slope will give a high exchange current density and it is thus important to make sure that the Tafel slope is in the expected region.

2.2 The Hydrogen Evolution Reaction

The hydrogen evolution reaction(HER) is perhaps the most studied electrochemical reaction and is of importance for applications ranging from electrodeposition and corrosion of metals to energy storage via H_2 production.

2.2.1 The Reaction Pathways

The hydrogen evolution reaction is a simple reaction where two protons and two electrons combine to form hydrogen, the reaction is given by:

$$2H^+ + 2e^- \rightarrow H_2 \tag{2.22}$$
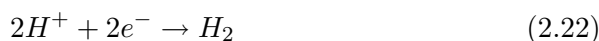
Different reaction paths have been proposed, the initial reaction where a proton and an electron react to form an adsorbed hydrogen atom, is called the Volmer reaction[14]:

$$H^+ + e^- \rightarrow H_{ad} \tag{2.23}$$

This reaction step can then be followed by the Tafel reaction[15], which is a Langmuir-Hinselwood type reaction where two adsorbed H atoms react associatively and desorbs

$$2H_{ad} \rightarrow H_2 \tag{2.24}$$

or the Heyrovsky reaction[16] which is an Eley-Reidel type reaction, where a proton and an electrons react directly with an adsorbed atomic H atom to form Hydrogen.

$$H_{ad} + H^+ + e^- \rightarrow H_2 \tag{2.25}$$

The exact reaction path is not always simple to deduce and it has for instance been found that the same material can exhibit different HER reaction paths on different facets, see example in the following section.

2.2.2 Interpreting Tafel Slopes

Studies of single crystal Pt electrodes performed by Markovic et al [17] have shown that the reaction mechanisms can vary for the different crystal planes. They found that the Tafel slope for the HER on the Pt(110) facet was 28mV/dec. $\approx 2.3RT/2F$. From the slope they interpreted the reaction path to be the Tafel-Volmer. On Pt(100) they found Tafel slopes of 37mV/dec. $\approx 2.3RT/3F$ (low overpotentials) and 112mV/dec $\approx 2(2.3RT/F)$ (high overpotentials). From these slopes they interpreted the reaction path to be the Heyrovsky-Volmer. On the Pt(111) facet they did however not find any conclusive evidence of the exact reaction mechanism as they recorded a Tafel slope of 74mV /dec.

The HER in an electrochemical double layer on Pt(111) has recently been investigated by means of DFT calculations by Skulason et al[18] , who introduced both a potential and water layers in their calculations. They were able to calculate the activation energies for both the Tafel and the Heyrovsky reactions and they found that they were comparable, with the Heyrovsky reaction being most favourable. The small difference in the calculated activation barriers explain the inconclusive observations on Pt(111) by Markovic et al.

In order to make an exact interpretation of the Tafel slope it is crucial to have the correct value of the transfer coefficient α. Usually the transfer coefficient for the HER is assumed to be between 0 and 1 [3] . For Pt the transfer coefficient has been found to be 0.5 according to Gasteiger et al[19]. Skulason et al[18] also calculated the transfer coefficients on Pt(111) for the different HER reactions and reported values of $\approx$0.4 and ≈ 0.65 for the Tafel and the Heyrovsky reaction respectively.

2.2.3 The exchange current density

The exchange current density i_0 for the HER is often the figure of merit when activities of different electrocatalysts are compared to each other. The exchange current density estimate is however not better than the Tafel slope used to extrapolate the current density to zero overpotential. It is thus important to evaluate both the exchange current density and the Tafel slope when different catalysts are compared to each other. For example the exchange current density for Pt ranges over several orders of magnitude depending on the measurements and conditions used. In a recent study

Gasteiger et al.[19] reported exchange current densities of 235-600 mA/cm$_2$ on Pt nanoparticles. This is two orders of magnitude more than the 0.8-1.4 mA/cm$_2$ reported by Markovic et al[17] on Pt single crystals. The two studies were done in very different systems, Markovic et al. measured on single crystals in a rotating disc electrode using a liquid electrolyte(0.05 M H_2SO_4) and Gasteiger et al. measured the activity on a specially prepared membrane electrode assembly.

Gasteiger et al explains the discrepancy as being due to the lack of uncompensated mass transport limitations in their system. Thus care should be taken when the exchange current densities of highly active HER catalysts are evaluated.

2.2.4 The exchange current density and Volcanoes

Volcanoes have been known in heterogeneous catalysis for decades and are based on the Sabatier principle[20]. Stating that optimal catalytic activity is achieved on catalyst with intermediate binding energies(heat of adsorption) of reaction intermidiates. In other words if the the binding is too weak the reactant will not adsorb on the surface and if the binding is too strong the the product will not desorb from the surface. Thus an optimal catalyst is able to adsorb the reactant and desorb the product.
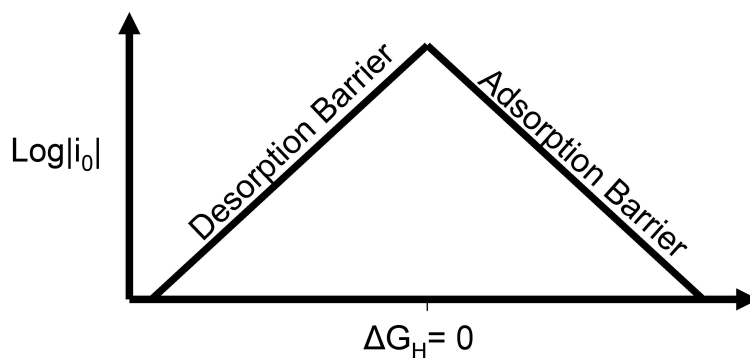

Figure 2.2: Volcano plot illustrating the Sabatier principle. The exchange current density is plotted as function of ΔG_H. If ΔG_H is negative the activity will be governed by the rate of desorption of products and if ΔG_H is positive the rate of the adsorptionof reactant will govern the activity.

The exchange current density for the HER has been studied for decades in order establish a connection between the activity and physical properties of the catalyst. It was first suggested by Parsons[21] that the exchange current density for the HER was governed by the Hydrogen binding free energy ΔG_H. Others have also plotted the exchange current densities as a func-
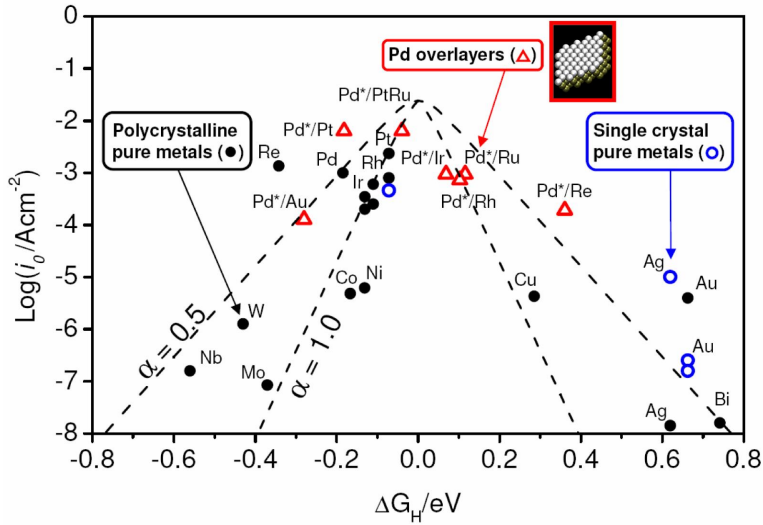
Figure 2.3: Volcano plot of the measured exchange current densities as a function of the DFT values for ΔG_H. The exchange current densities are compiled from [25, 9, 24] and the calculated values ΔG_H values are from [11].

tion of different properties like metal hydride formation energies and work functions[22, 23, 24]. Ultimately all of these volcanoes reflect the Sabatier principle illustrated in Figure 2.2 where the most active HER catalysts has no adsorption barrier or desorption barrier.

Recently this volcano has appeared in a new version where the exchange current density for different metals[9] and Pd overlayers[25] is plotted as function of DFT calculated values of ΔG_H for the corresponding metals and overlayer surfaces. One could argue that the DFT calculations for such systems are simple and thus not accurate enough to describe the complexities of the electrode surroundings. But the descriptor for the HER activity, the calculated values of ΔG_H, scales with the measured values of the exchange current density, see Figure 2.3.

2.2.5 The HER Catalyst

According to Figure 2.3 the most active catalysts for the HER are those of the platinum group metals, the platinum group metals are also special because they are generally stable in corrosive environments[26]. The combination of stability and high activity has led to the use of platinum for various applications in corrosive environments. The catalyst that are currently used in low temperature PEM fuel cells are for instance based on platinum and platinum alloys. Unfortunately the platinum supply is limited and it is thus

crucial to have alternatives that are just as active and stable. Especially as the increasing focus on the hydrogen economy could lead to an increased use of Pt to for instance fuel cells.

Chapter 3

Experimental methods and setups

The experimental methods and setups used in this thesis are a combination of surface science techniques and electrochemical measurements. This combination ensures that we are doing electrochemistry on samples that were well characterized.

3.1 Electrochemical Methods and the Setups

Electrochemical measurements where electrode currents are measured as a function of an applied potential is a strong and versatile tool. These methods can provide information of many different characteristics of a certain electrode setup, such as surface area, reaction kinetics and reaction rates.

3.1.1 Voltammetry

Voltammetry where the potential is ramped with a certain rate while corresponding current is recorded is a very sensitive method. It is possible to measure transfer of charge(current) at the interface between an electrode an an electrolyte. This surface sensitive technique gives the opportunity to study a wide variety of different processes at the electrode interface, but it can at the same time be difficult to identify the process that exactly led to to an increase in current. If a constant potential E is applied to an electrode then the steady state current can consist of different components:

$$i = i_{reaction1} + i_{corrosion} + i_{reaction2} + i_{charge} \tag{3.1}$$

The current can consist of four different current sources, two different reactions, corrosion of the electrode and charging of the electrode, making the exact interpretation difficult. The interpretation is complicated further since the potential applied to the electrode might not be the exact potential
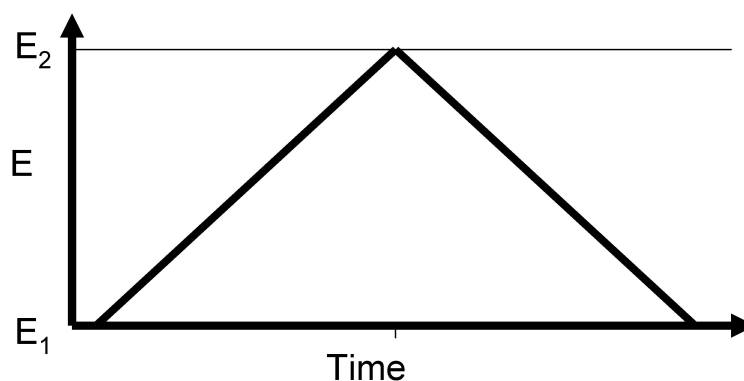
Figure 3.1: The potential ramp used to create a cyclic voltammogram, where the potential is changed between two potentials with a constant rate.

at the electrode-electrolyte interface. There could also be potential losses in both the electrolyte and the electrode due to resistance.

One way to distinguish the different processes from each other is to apply a non constant potential. One simple method is changing the potential linearly from one potential E_1 to another potential E_2 while the current is recorded, if the potential then afterwards is changed from E_2 to E_1 (See Figure3.1) a cyclic voltammogram(CV) can be made.
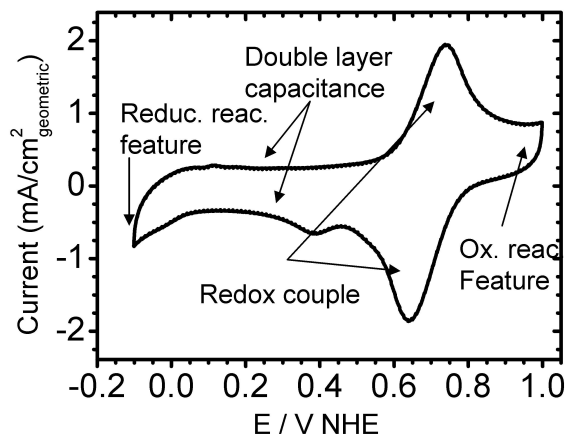
Figure 3.2: Cyclic Voltammogram of an unknown sample illustrating some of the different oxidation and reduction features that can be encountered.

In Figure 3.2 an example of a CV is shown. This samples CV has specific characteristics. On the anodic(towards more positive potentials) and the cathodic(towards more negative potentials) sweeps there are a set of peak centered around 0.7 V vs. NHE. This redox feature shows that charge(electrons) are removed from the electrode during the anodic sweep and added on the reverse sweep. Such a feature could be due to anodic desorption of an adsorbed species followed by cathodic adsorption of the same species. It could also be the opposite where anodic adsorption is followed by cathodic desorption. But many other possibilities for such features exist and usually spectroscopic techniques are coupled with the electrochemical setup to measure the exact source of the redox features. The second feature that can be seen in Figure 3.2 is the double layer capacitance which causes a positive shift of the current at anodic sweeps and a negative shift of the current at cathodic sweeps. The size of the redox couple peak and the double layer capacitance is a function of the scanrate as both features consist of addition and removal of a finite charge. A third feature can be seen at potentials more positive than 0.8 vs NHE. Here the current seem to have a positive shift, which could be due to an oxidation reaction of some species or simply corrosion of the electrode. A fourth feature is seen at potentials more negative than zero vs NHE. Here the current is shifted more negative indicating the possible reduction of protons in hydrogen or another reduction reaction. Many other voltammetric techniques exist, where the potential for instance can be applied as sine curve or as steps. Each of these methods are suitable for the investigations of different phenomena. An overview of different techniques and electrochemistry in general can be found in[4].

15

3.1.2 The Electrochemical Setups

In this thesis we have primarily used two different kinds of electrochemical setups. A setup dsigned for the test of membrane electrode assemblies(MEA) for fuels and a standard three electrode setup. Both setups where coupled to a Biologic WMP2 potentiostat with an impedance option.
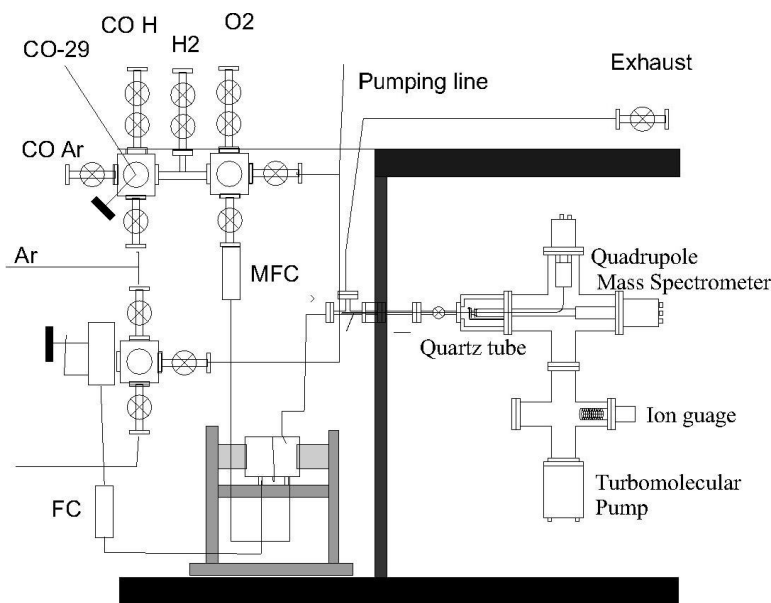

Figure 3.3: The setup used for the test of electrode materials on high surface are supports in a two electrode setup. The electrodes can be tested for reactivity under a variety of gasses.

In Figure 3.3 the fuel cell setup is depicted. This setup was originally designed for isotopic CO exchange measurements[27] and allows for the testing of MEAs under various gases, with the possibility of having the exhaust gases analyzed by a mass spectrometer. This setup was initially used to test electrode materials that were supported on high surface area carbon and made into MEAs. The setup allows for the testing of catalyst for electrochemical reactions like the HER, the hydrogen oxidation reaction(HOR), the HOR in trace amounts of CO and the oxygen reduction reaction(ORR). It has primarily been used for the initial screening of different materials. These materials were tested for stability and ability to catalyze the wanted reactions at reasonable potentials under conditions that resembled those found in commercially available systems. The test of materials in this manner is however quite tedious. This requires careful preparation of the MEAs in order to compare the activities of different catalysts with each other and not the difference in preparation method.
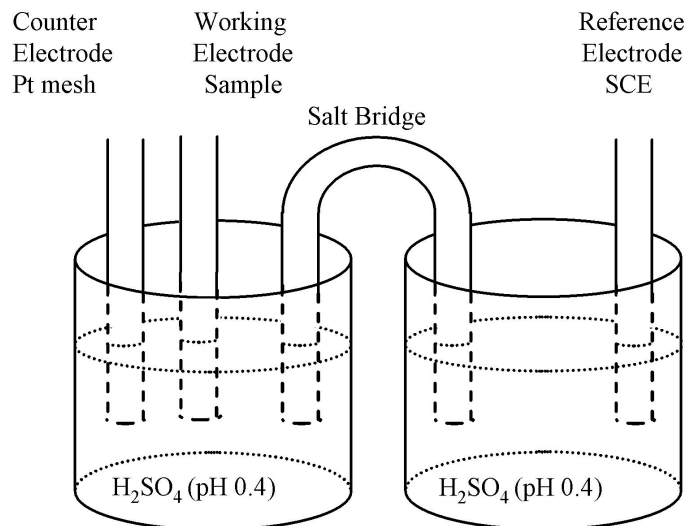
Figure 3.4: Three electrode setup with a SCE reference electrode a counter electrode and a working electrode. The reference electrode is compartmentalized via a salt bridge

The second type of electrochemical setup used is a typical three electrode electrochemical setup consisting of a working electrode(sample) a reference electrode(SCE) and a counter electrode(usually Pt mesh). The reference electrode was compartmentalized via a salt bridge to avoid contamination issues and the electrolyte was usually nitrogen purged. This setup was used to make electrochemical measurements on a variety of different samples ranging from UHV prepared and characterized nanoparticles on single crystals to sheets of different metals. Typically the measurements were conducted in a 0.5 M H_2SO_4 electrolyte, and the pH of the electrolyte was always measured after measurements.

3.2 X-ray Photoelctron Spectroscopy

X-ray Photoelectron Spectroscopy(XPS) was used to give information of the chemical state and composition of the catalysts before and after electrochemical characterization.
XPS is based on the radiation of a sample with X-Rays. If the X-Rays are absorbed by a core electron, the core electron can escape the sample as a photoelectron with a kinetic energy given by:

$$E_{kin} = h\nu - E_B - \varphi_{sample}$$ (3.2)

The energy of the incoming photon is given by $h\nu$, the binding energy of the electron in the sample is with respect to the Fermi energy is given by E_B and the work function of the sample is given by φ_{sample}. The incoming X-rays are usually created by an Al kα or a Mg kα radiation source, with main radiation peaks centered at $h\nu = 1486.6$ eV and $h\nu = 1253.6$ eV, respectively. This means that kinetic energy of the emitted photoelectron can be up to that of the radiation source and thus the inelastic mean free path of the electrons is short, ensuring that this technique is surface sensitive. If the X-ray radiation used is well defined the kinetic energy of the escaping photoelectron will only be a function of φ_{sample} and E_B. As each element has specific major and minor peaks in the XPS spectra, XPS can be used to identify the elements by comparison with a reference database[28]. The intensity of the XPS peaks can be used to quantify the concentration of different elements in a given sample, and often XPS is used to check samples for unwanted impurities. The position of the peaks of the different elements can also be shifted by the local chemical environment of the elements. Finally XPS is a surface sensitive technique since the mean free path of the escaping photoelectrons is on the order of nanometers, thus only photoelectrons from the outmost layers of the sample will escape and be detected.

Chapter 4

Reducing the use of Pt

Many approaches can be used in the search for alternative catalyst and historically a trial and error approach has been successful. Haber for instance tested several thousands of catalyst in several thousands of experiments before he found the optimal catalyst for the Haber-Bosch process[29]. This iron based catalyst is still in use today. In recent years high throughput combinatorial methods have been employed to find and improve catalysts[30]. These methods of trial and error have been and are still successful but it requires significant resources to synthesize and test many different materials in this manner. By means of insight into the different descriptors that govern the activity and the stability, it should however be possible to avoid the major parts of the trial and error test. Since the descriptors can be used to exclude a majority of candidate materials. Ultimately the goal is to be able to design, synthesize, characterize and test materials for given reaction without having to due several iterations of each step.

For the hydrogen evolution reaction it is not only important to find active materials as stability is an issue especially if the catalyst is to be used in acidic environments.

4.1 The Descriptor for HER reactivity

For the hydrogen evolution reaction, the descriptor for the activity is the free energy of hydrogen adsorption ΔG_H [21] and it is possible to calculate the value of this descriptor by means of DFT[9], as described in section 2.2.4. Knowledge about the nature of the descriptor allows one to improve the a property of an already existing catalyst or to find alternative materials with a similar value of this descriptor. In the following section the focus will be on some of the different approaches that have been considered to improve HER activity of Pt and Pd.

4.2   Tuning the Activity of electrocatalysts

The activity of a catalyst is usually determined by the turn over frequency per site, however in reality most of the concern is related to the activity on a per gram basis. It is well known that Pt and Pd which are members of the platinum group metals are good HER catalysts having values of ΔG_H close to zero.

4.2.1   Nanoparticles

The use of a catalyst in the form of nanoparticles has been known for years. One of the major improvements in for instance the fuel cell industry is the use of smaller particles which give a higher surface areas per gram of catalyst. The use of nanoparticles gives an advantage in the form of surface area per gram of catalyst but in recent years it has been found that some nanoparticles are exhibiting improved activity that cannot only be explained by the high surface area. One example of this is room temperature CO oxidation on Gold nanoparticles that was discovered by Haruta et al[31]. This work has been followed up by several groups and in a recent study Janssens et al[32, 33] showed that the activity indeed was correlated with the number of the under coordinated corner sites of the Au nanoparticles. The opposite effect has been reported for the ORR on Pt nanoparticles where small particles appear to be less active on a per surface area basis than small particles[34, 35]. Another effect of nanoparticles that should be taken into account is wetting as some nanoparticles change shape as function of the surrounding conditions. An example of this this effect has recently been observed on Cu nanoperticles[36]. It is thus important to have knowledge about the number of the most active site of the nanoparticles under operating conditions.

4.2.2   Overlayers

Another way to tune the activity of a catalyst is to stress or strain the lattice. Stress or strain will according to d-band model[37], change the position of the d-band center and thus the binding energy of an adsorbed molecule[38]. Strain will cause the d-band center to be lowered with respect to the Fermi level and thus the the binding energy of adsorbates increase. The opposite is the case for the introduction of stress. This effect has been studied by Greeley et al[25], who studied the HER of Pd overlayers on different substrates. They found as predicted by the d-band model that it was possible to change ΔG_H and thus the HER activity by the introduction of stress or strain.

4.2.3 Alloys

The alloying of Pt with other, possibly cheaper metals is well studied for the Oxygen reduciotn reaction(ORR). Pt has been alloyed with almost every transition metal and tested for ORR activity. One of the early studies where performed by Jalan et al[39] who studied the ORR in phosphoric acid fuel cells. They found a relation between the activity and the lattice spacing of Pt, and proposed that alloys of Co or Ni and Pt should be the next promising candidates. Both of these catalysts where in fact later used in PEM fuel cell and both PtCo and PtNi have been investigated both theoretically and experimentially[40, 41] .In the case of PtCo it was, however, later found that the Co corroded away and the surface could basically be considered as a Pt skin on a PtCo alloy[42] where the lattice is slightly stressed. This should cause the oxygen binding energy to be reduced, which according to the model proposed by Nørskov et al[8] should increase the activity.

Chapter 5

Pt based systems

Pt based systems have been extensively studied for the HER and the chance of finding an alternative Pt based system that has not previously been studied is limited. In the following chapter measurements will be presented for two different Pt based systems. The first system is a BiPt surface alloy that was identified by means of high throughput combinatorial screening. The second system is a core shell system with a core of Au and a shell of Pt.

5.1 Computational Screening and a BiPt surface alloy

The value of ΔG_H for the HER can be calculated by means of DFT. In recent years the development of computers and DFT codes have made it possible to perform large scale computational screening of different properties for many different materials. In this section the DFT screening procedures and the non intuitive result of the screening will be presented that were used in **Paper 2**.

5.1.1 Screening procedure

Several approaches can be undertaken when a screening procedure for alternative catalysts is employed. For the HER the main activity parameter to screen for is ΔG_H. In this case ΔG_H was calculated for mono and sub-monolayers of a solute element on a host material.
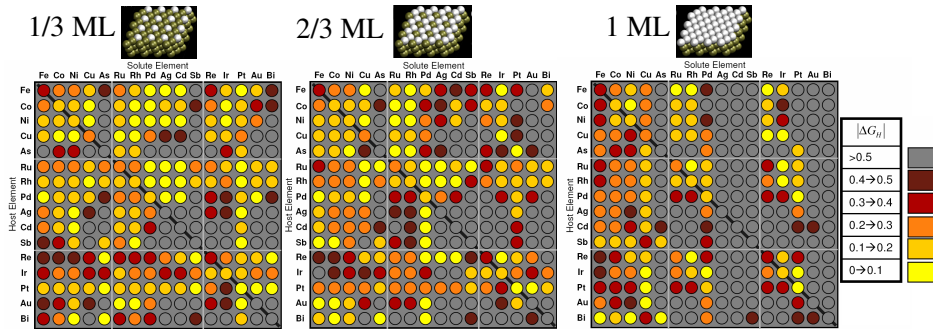
Figure 5.1: The calculated values for the ΔG_H of the combination of 16 metals and semimetals

The initial calculations on the 736 different systems gave approx. 105 systems with a value of ΔG_H close zero. This is illustrated as bright yellow dots in Figure 5.1. In order to narrow the amount of viable candidates further down several stabilty calculations were made. The stability calculations where as follows: 1: The free energy change for surface segregation, i.e. segregation of surface atoms into the bulk. 2: Free energy of infrastructure transformations, i.e. islanding and deformation. 3: Free energy of oxygen adsorption by water splitting, i.e. surface poisoning and oxidation. 4: Free energy of dissolution of the materials from the electrochemical series, i.e. corrosion effects.
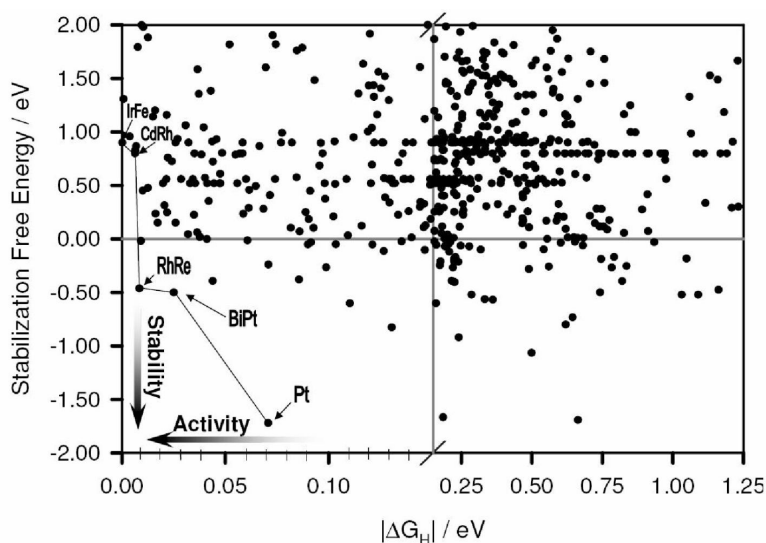
Figure 5.2: Pareto-optimal plot of stability and activity of surface alloys for the Hydrogen Evolution Reaction (HER). The Pareto-optimal line indicates the best possible compromise between activity and stability. The alloys in the lower left quadrant are the moss promising candidates.

In Figure 5.2, the free energy of stability is plotted as a function of the absolute value of ΔG_H . The Free energy of stability is the most pessimistic values from the stability calculations performed[11, 43]. The Pareto optimal candidates, the candidates which are the best comprise between stability and activity, are shown by a Pareto line. The Pareto optimal candidates are, 1/3 ML Bi on at Pt Host(i), 1 ML of Rh on a Re host, 1/3 ML Cd on Re, and 2/3 ML Ir on Fe. Of these candidates we found that 1/3 of a monolayer of Bi on top of Pt was an interesting candidate.

5.1.2 BiPt the non intuitive candidate

A Bi surface alloy on top of a Pt host is an especially intriguing candidate as it is rather counterintuitive to mix an active metal Pt and an inactive semi metal Bi. The respective current densities for Pt and Bi are illustrated on Figure 2.3. Electrocatalysts based on Pt and Bi have been extensively studied for various oxidation and reduction reactions and an overview of these studies has been given by Markovic and Ross[44]. No electrochemical studies of surface alloys of Pt and Bi were mentioned. Feliu and Aldaz did however study a similar system[45] , Bi adatoms on Pt(111) and found that the adsorption of Bi ad-atoms poisoned the HER activity of Pt(111). Despite the previous findings on the BiPt systems it was decided to synthesize a BiPt surface alloy.
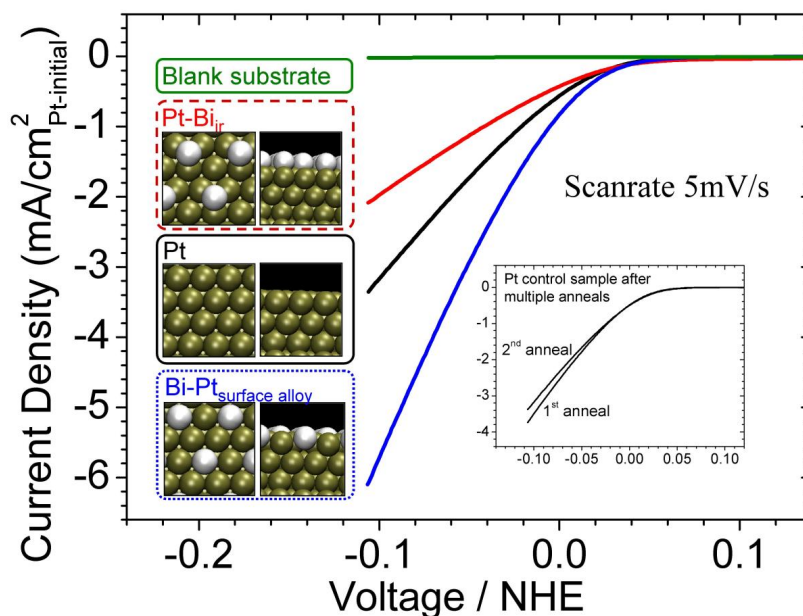
Figure 5.3: The HER measured at different stages of the synthesis: The pure Pt sample with an activity that is expected by platinum. The sample where Bi is irreversibly adsorbed, showing a lower activity that the pure Pt sample, just as measured by Feliu and Aldaz[45]. Finally the BiPt surface alloy showing an increased activity as predicted by the DFT screening. The inset shows the activity of a Pt sample that has seen several heating cycles to 500 °C. The electrolyte was 0.5 M H_2SO_4 and the scanrate was 5 mV/s.

In a surface science stuy by Campbell et al.[46] it had previously been reported that Bi on Pt(111) single crystals formed a surface alloy when heated a to 370 °C. Thus it should be possible to create a surface alloy by means of heating Bi ad-atoms on a Pt host. The first step in the preparation of the surface alloy is to find a clean Pt host material, as the high temperatures will cause any contaminants to segregate to the surface. Initially it was chosen to use electrodeposited Pt on a flourine doped tinoxide coated glass(FTO) substrate. The as deposited Pt was calcined at 500 ^{circ} C and then tested for the HER, Bi was then adsorbed by means of underpotential deposition of Bi from a 1mM Bi^{3+} aqueous solution. The sample then was tested for the HER again before the sample finally was heated to 500 ° C. This led the creation of the BiPt surface alloy skin, and the sample was again tested for the HER.

Figure 5.3, shows the result of the test for HER activity at different stages of the synthesis on the same sample. Initially, the pure Pt sample has the expected activity for a polycrystallline Pt sample. After Bi is irreversibly adsorbed the activity is decreased just as Feliu and Aldaz had previously observed[45]. This sample was then heated and the activity was found to increase again and that to a point where the BiPt surface alloy was in fact more active than the initial Pt sample.
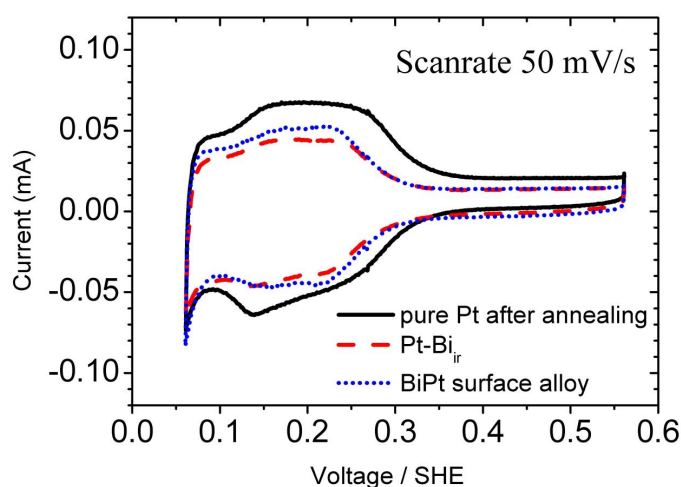

Figure 5.4: The H_{UPD} region of the BiPt sample at different stages of the synthesis, note that the surface area is apparently not increasing.

This was exactly what the DFT screening predicted. In order to make sure that this increase in activity was not due to a roughening of the surface the H_{UPD} region was recorded, see Figure 5.4. As it can be seen the H_{UPD} region is not increased after the different synthesis steps, this indicates that the increase in activity is not due to a simple change in surface area of the sample. A more detailed discussion of this study can be read in **Paper 2**[11].

5.1.3 Hydrogen oxidation and CO tolerance

The BiPt was also tested for the HER and the HOR with or without 100 ppm CO. We opted to test the BiPt surface alloy for CO tolerance because the hydrogen binding energy was lower on BiPt than on pure Pt. As binding energies are usually correlated[47], a lower hydrogen binding should give a lower CO binding energy, which should correspond to a lower CO coverage

and thus a higher level of CO tolerance[27]. In order to test the CO tolerance the BiPt surface alloy was deposited on a high surface area support and made into a membrane electrode assembly.
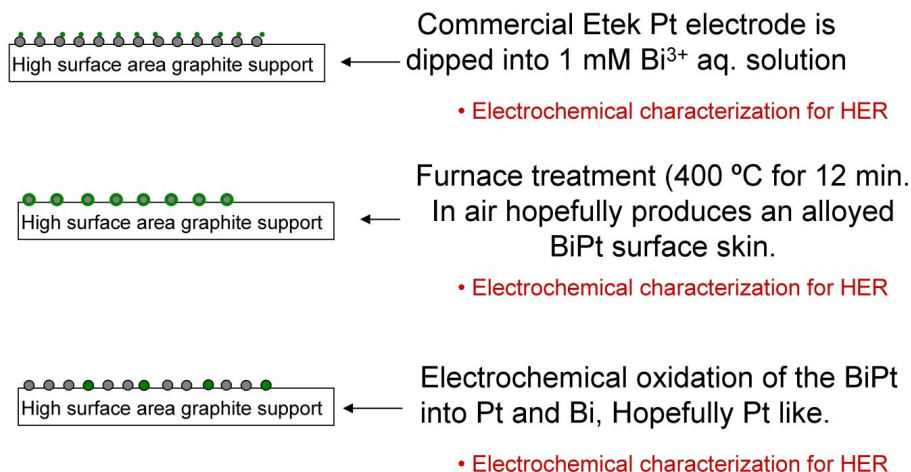

Figure 5.5: The preparation of BiPt on ETEK and the test procedure. A slightly modified version of the preparation procedure from[11] was used, and the as the nanoparticles had a tendency to sinter when heated the same sample could not be tested at different stages of the sythesis.

ETEK Pt was used as the support material for the surface alloy and the Bi_{UPD} method was used to absorb Bi on the Pt nanoparticles as in[35, 45]. The heating procedure was however slightly changed as the sample was heated to 400 °C for 12 minutes to avoid sintering of the Pt nanoparticle and oxidation of the carbon support, See Figure 5.5. The activity of the BiPt surface alloy on Pt nanoparticles could not be evaluated at different stages of the synthesis as they had to be pressed into an MEA in order to be tested. Thus the alloyed sample was always tested with respect to a sample that had seen high anodic potentials where Bi would be oxidized and most likely desorbed into solution[26]. It was found by means of chronoamperometric studies that the BiPt surface alloy was not stable at potentials more anodic than 0.25 V vs. NHE.
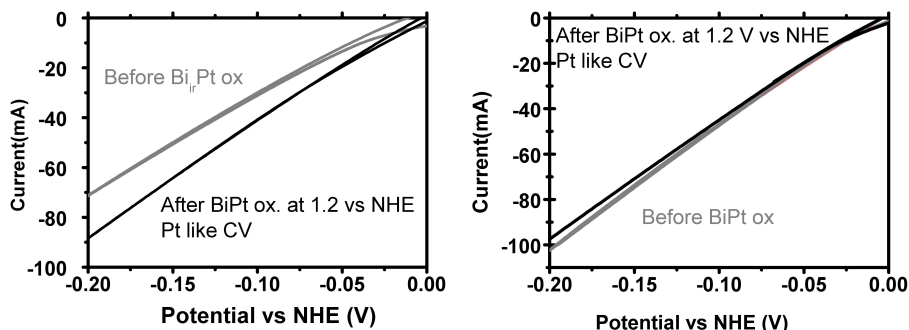
Figure 5.6: Left: HER on ETEK Pt nanoparticles with irreversibly adsorbed Bi. After oxidation at 1.2 V vs. NHE the activity increases, corresponding to the removal of the Bi-adatoms that poisened the HER. Right:HER on ETEK Pt nanoparticles with a surface alloy of BiPt, after oxidaton at 1.2 vs. NHE the HER activity is decreased corresponding to the removal of the more active BiPt surface alloy. Measurements where performed in the Fuel cell setup with a flow hydrogen(20 ml/min.) over both electrodes and with a scanrate of 5 mV/s

In Figure 5.6 the HER on two different samples are measured before and after the removal of Bi by means of oxidation at 1.2 V vs. NHE. It was found that the HER activity increased after oxidation of the sample with adsorbed Bi ad-atoms and decreased after the oxidation of the sample with the BiPt surface alloy. This finding supports the previous findings[11], where it was found that Bi ad-atoms poisoned the HER on Pt whereas a BiPt surface alloy promoted the HER on Pt.
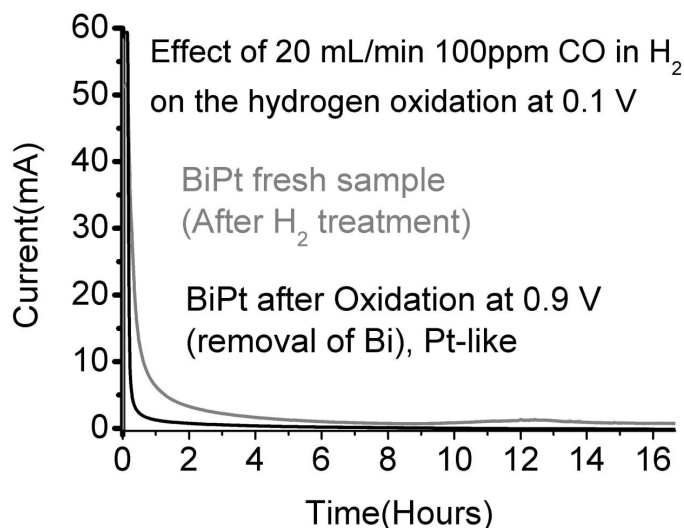
Figure 5.7: Chronoamperommetry study of the HOR in 100 ppm of CO at 0.1 V vs. NHE. The study was conducted on the same sample before and after oxidation at 0.9 V vs. NHE, in the Fuel cell setup. Note how the CO tolerance decreases after the BiPt surface is oxidized at an anodic potential of 0.9 V vs. NHE.

Figure 5.7 shows an initial attempt to study the CO tolerance of the BiPt surface alloy. It can be seen that the BiPt surface alloy is slightly more tolerant to CO than the the same sample that have been subjected to a potential of 0.9 V vs. NHE(where Bi is assumed to be desorbed). From a scientific point of view this effect is interesting, but for commercial purposes the CO tolerance of the BiPt surface alloy is not significant, and as the preparation procedure was rather tedious this system was not investigated further.

5.2 PtAu core shell nanoparticles

Another Pt based system that was investigated was a core shell, composed of a Pt skin on an Au core. Such core shell systems could potentially reduce the amount of used Pt significantly and at the same time this system would not suffer from corrosion issues as both Pt and Au are quite resistant to corrosion[26]. This system will not suffer the corrosion issues found on both Pt alloys like PtNi and PtCo[42]. Is has also recently even been proposed that the addition of Au clusters to Pt will reduce corrosion [48]. Pt overlayers on Au(111) have previously been studied by Besenbacher et al [49], they find that the the reactivity of Pt is increased whit respect to pure Pt. They

explain this finding with the d-band model[37] where stress in the lattice of Pt induces an shift in the position if the d-band and a subsequent change in the reactivity of the surface. For the case of Pt an increase in reactivity is optimal since Pt according to models for both the HER[9] and the ORR[8] is to reactive. But if the amount of Pt used in a core shell system of Pt and Au could be reduced the significantly the lower amount of Pt used would counteract the loss in activity and the system might then be viable anyhow. Since the system were to be tested in in the fuel cell setup described in section 3.1.2 ETEK Au nanoparticles that were supported an xc72 carbon were used as the host material. The Au nanoparticles were mixed with Nafion to form an ink and supported on a Toray paper. Pt was then deposited on the Au nanoparticles in a three electrode cell(0.5 M H_2SO_4), where a Pt mesh counter electrode was used as a Pt source. Consecutive cycling of the potential of the Au working electrode from -0.2 to +1.6 V vs. NHE led to contamination of the Au nanoparticles with Pt and thus the creation of nanoparticles with a core of Au and a shell of Pt. This electrode was then pressed into a MEA together with a commercially available Pt gas diffusion electrode(serving as both the counter and the reference electrode) from IRD fuel cells and mounted in the Fuel cell setup.
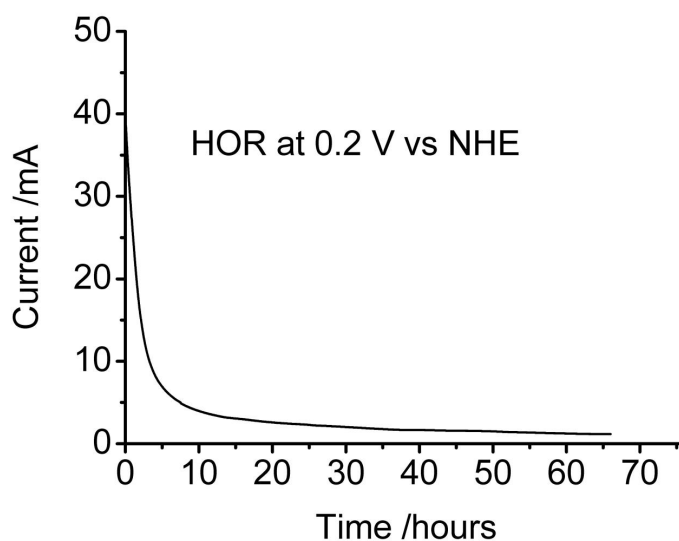

Figure 5.8: Chronoamperommetry of the hydrogen oxidation reaction at 0.2 V vs. NHE on the PtAu core shell particles in the fuel cell setup, note how the HOR activity decreases significantly as a function of time, a hydrogen flow of 20 mL/min. was applied to both electrodes.

Initially the electrode was tested for the HOR reaction in a chronoamper-

ommetry experiment, see Figure 5.8. The HOR activity is initially high, but in time the activity is drastically reduced down to a level where hardly any hydrogen oxidation is occurring. The exact cause of this reduction in activity could be due to several effects like corrosion, poisoning and segregation effects. As the applied potentials are reasonably low and the gases used were pure(N60) the loss in activity is most likely not due to poisoning or corrosion. Thus the cause of the loss in activity could be a surface enrichment of Au, this notion is further supported by theoretical calculations[49, 50] where is was found that is was thermodynamically favorable to have Au on top of Pt.
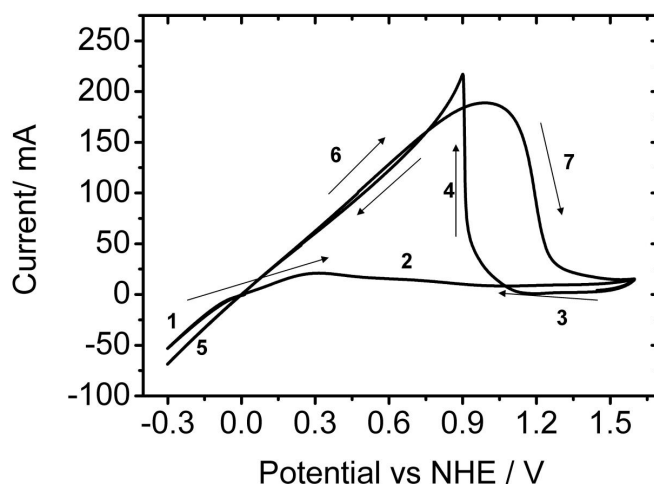

Figure 5.9: Cyclic voltammogram preformed after the deactiviation of at 0.2 V vs. NHE. The initial potential was 0 V followed by a sweep to -0.3 V. Then the potential was cycled between -0.3 V to 1.6 V vs. NHE. Note how the HOR initially is quenched until the potential has been cycled anodically to 1.6 V vs. NHE and an abrupt increase of the HOR can be noticed on the cathodic back sweep. The scanrate was 5 mV/s and the hydrogen flow was 20 ml/min on both electrodes.

Figure 5.9 shows CVs of the sample that deactivated during HOR in figure 5.8. On the first sweep towards the anodic potential of 1.6 V vs. NHE there is hardly any evidence of hydrogen oxidation, as it would be expected if we had a pure Au surface. But on the subsequent cathodic sweep an abrupt increase in the HOR is seen at around 0.9 V vs. NHE and the sample is suddenly behaving more like a Pt sample. This change from the sample being Au like to the sample being Pt like was intriguing and the same sample was then deactivated during HOR at 0.2 V vs. NHE and the change in activity

was investigated by means of CVs that were swept to more and more anodic potentials.
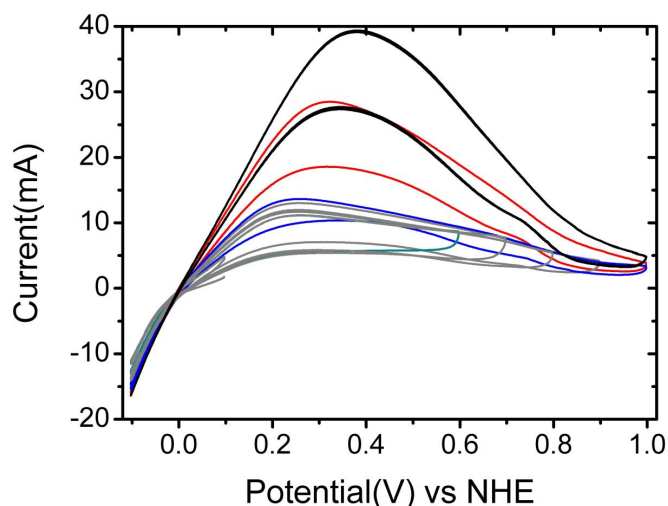

Figure 5.10: Detailed investigation of the onset of the activation of the PtAu system. Again a deactivated system was investigated, but this time several CVs were recorded. In the initial CV the potential was swept between -0.1 V and +0.1 V vs. NHE. The following CVs were swept to more and more anodic potentials, until the sample started to exhibit and increase in the HOR current.The scanrate was 5 mV/s and the hydrogen flow was 20 ml/min on both electrodes.

A more thorough investigation of the onset of the sample becoming Pt-like is shown on Figure 5.10 where the sample gradually is subjected to a more and more anodic potential. The sample behaves Au like and shows no or low HOR activity until the potential has reached 1.0 V vs. NHE where consecutive sweeps show an increase in the HOR activity. We have thus seen how the core shell sample becomes Au like a potentials between -0.2 and 0.2 V vs. NHE. While it becomes more Pt like at potentials above 0.9 V vs. NHE. The switch from being Au like to being Pt like is apparently occurring with different reaction mechanisms a fast mechanism that only required one sweep to 1.6 V vs. NHE and a slow mechanism requiring several sweeps to 1.0 V vs. NHE.
In parallel with this study, a study was also conducted in the three electrode setup, where Au foil or particles are being coated with a thin layer of Pt and this sample shows the exact same characteristic switches from the sample being Pt like to sample being Au like. This sample is currently being

33

investigated by means of XPS, when the sample behaves like Pt or like Au. Currently the following conclusion have been made on the mechanisms in question and the state of the surface at different potentials:

- At moderate anodic potentials up to 1.0 V vs. NHE Au seggregates to the surface covering the Pt skin.

- At 1.6 V vs. NHE Au is probably corroded[26] away from the surface exposing the Pt in one single sweep. Notice that Pt will form a stabilizing oxide at these potentials[26]

- At 1.9 vs. NHE Pt is apparently slowly segregating towards the surface, the driving force could for instance be OH adsorbates that adsorb stronger on Pt than on Au, thus making it more thermodynamically favourable for Pt to be at the surface.

The system is currently under further investigation[51]. The PtAu core shell system is an example of the complexity involved in the design of electrocatalysts in general, as the designed system could be a different system under operating conditions.

Chapter 6

Biomimetic systems

Nature has its own catalysts in the form of enzymes, the common denominator for these enzymes is that they in general are based on abundant materials. Some of these enzymes are indeed able to evolve hydrogen[52] and the enzymes hydrogenases and nitrogenases are examples of these enzymes based on building blocks like Fe, Ni, Mo, S and N. The hydrogenase enzyme is primarily evolving hydrogen[53], whereas the nitrogenases evolves hydrogen as a part of the fixation of nitrogen to form ammonia[54]. Both of these have been found to evolve hydrogen effectively[55, 56, 53] and work has also been done on electrodes where the enzymes[57] or structures resembling these enzymes[58, 56, 59] were tested for the HER.
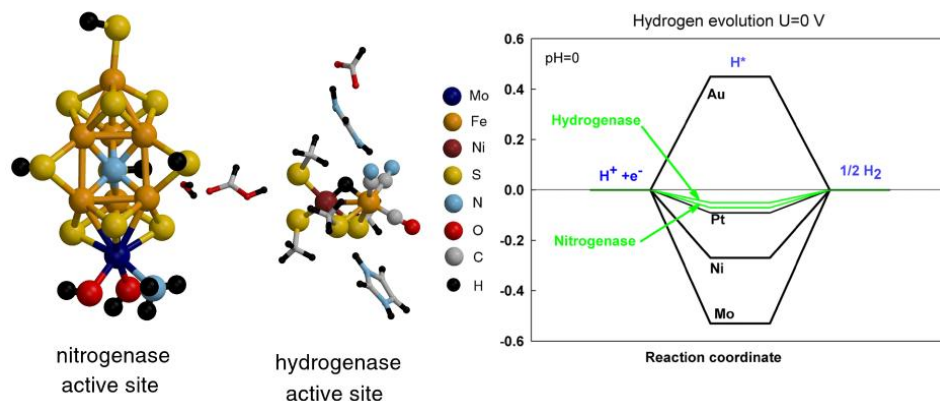

Figure 6.1: The active cite of nitrogenase and hydrogenase and the calculated values for ΔG_H. Note how the hydrogen binding energy on the Pt and the enzymes are similar.

The structure of the active site of both nitrogenase and hydrogenase has also been modelled[60, 61]. This allowed for the calculation of the descriptor for hydrogen evolution, ΔG_H. Figure 6.1 shows the structure of the active site of hydrogenases and nitrogenases, and the corresponding values of ΔG_H.

The calculated values of ΔG_H are close to zero and thus these enzymes should be active for the HER. This finding was indeed promising since the DFT calculated values of ΔG_H apparantly also where a useful descriptor for HER activity of sulfides.

In this chapter the HER activity of different metal sulfides will be discussed, the majority of the discussion is based on the work presented in **Paper 1** and **Paper 3-5**.

6.1 HER on Metal Sulfides

The active site on both the nitrogenase and the hydrogenase contains both metal and sulfur atoms, and for the case of the nitrogenase the hydrogen is bound to an under coordinated sulfur atom. Such undercoordinated sites are also found on several types of inorganic metal sulfides, one of the most studied metal sulfide systems is nanoparticulate MoS_2. MoS_2 based catalysts have been extensively studied, since they are used commercially for the hydrodesulfurization(HDS) process[62]. Recent progress in both STM imaging[63] and modelling[64] of MoS_2 nanoparticles have given important insights into the morphology of supported MoS_2. Bulk MoS_2 consists of stacked S-Mo-S layers, whereas the MoS_2 nanoparticles are found as single S-Mo-S layer hexagonal structures exposing two different kinds of edges, the so-called Mo-edge and the S-edge. It has been shown that the structure of nanoparticulate MoS_2 is a single layered truncated triangle primarily exposing the Mo-edge when supported on Au(111)[63].
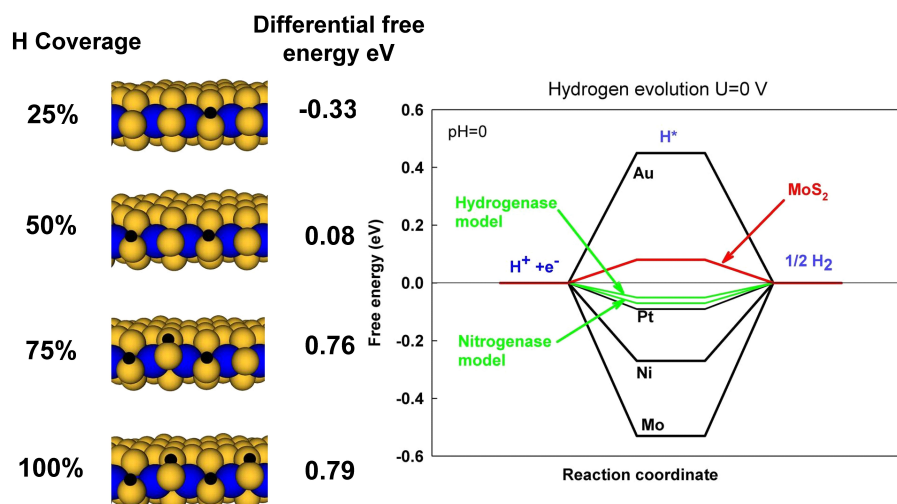

Figure 6.2: The Mo-edge of MoS_2 nanoparticle with different hydrogen coverages on under coordinated sulfur atoms. Note how the active site resembles the active site on the nitrogenase enzyme. The calculated value of ΔG_H on the Mo-edge of MoS_2 is found to be close to zero and it is thus expected that MoS_2 will evolve hydrogen at resonable overpotentials.

Figure 6.2 shows the active site for the HER being the Mo-edge of a MoS_2 nanoparticle and the DFT calculated value of ΔG_H on the Mo-edge. This finding was indeed interesting since MoS_2 in its bulk form has been subject to extensive photo-electrochemical studies[65, 66], and it was the general notion that MoS_2 was not a viable HER catalyst[66]. There were however a few studies of the HER on MoS_2. One study was reported by Nidola et

al[67] who found that the HER activity and the stability of a NiS coating increased when MoS_2 was added. The increased activity was described as being due an increase in "'true surface area"'. Another HER study on MoS_2 was reported by Sobczynski[68] who studied MoS_2 supported on SiO_2 and found that hydrogen was evolved from an acidic V^{2+} solution when MoS_2 supported on SiO_2 was added. The amount of hydrogen was found to be comparable with the amount of hydrogen evolved when SiO_2 supported Pt was added. It was concluded that MoS_2 and Pt had similar hydrogen evolution activity. None of these studies tried to measure an overpotential or to normalize their currents as a function of for instance surface area or number of active sites.

6.1.1 Initial Studies on MoS_2

To test whether or not MoS_2 is a viable HER catalyst, MoS_2 on a high surface area Daihope carbon was tested in a MEA. Where Pt was used as both the counter and the reference electrode and the MoS_2 was used as a working electrode. See **Paper 1** for more details[10]. The MEA was then tested in the fuel cell setup and a mass spectrometer was used to verify that hydrogen indeed was evolved.
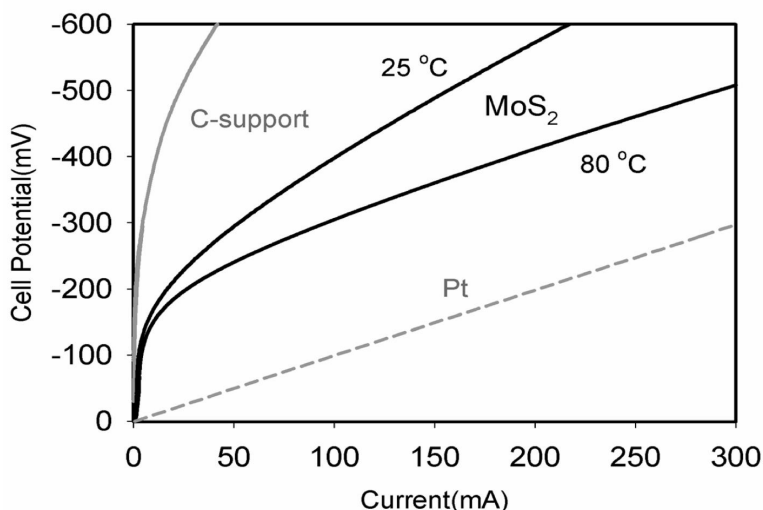

Figure 6.3: Polarization curve of the carbon supported MoS_2, compared with a Polarization curve of the carbon support and Pt. The scanrate was 5 mV/s and 20mL/min. of hydrogen was passed over both electrodes.

The result of the initial test is shown in Figure 6.3. The MoS_2 sample is able to evolve hydrogen at around -0.15 V vs NHE, at a rate which is significantly higher than the carbon support. It is also clear that MoS_2 is not as active

as pure Pt, this was however expected as the value of ΔG_H for platinum is closer to zero than for MoS$_2$. We could, based on these measurements not quantify the specific activity or for the HER on MoS$_2$ in a manner that allowed for direct comparison of the activity with other HER catalysts. We were also not able to show whether the edge of the MoS$_2$ nanoparticles indeed was the active site.

6.1.2 Measuring the area of MoS$_2$

The quantification of the number and type of different sites on a catalyst is one of the most important and difficult tasks when the activity of a certain catalyst is evaluated. MoS$_2$ has as mentioned before been studied for its ability to catalyze the HDS reaction, and only in recent years the role of the different cites on this catalyst has been understood[69].
Given that the amount of research on especially MoS$_2$ is comprehensive it should be a simple task to find a simple and suitable method that would determine the number and types of sites of the MoS$_2$ sample prior to electrochemical characterization. Several studies have been made were the HDS activity was correlated with the adsorption of different simple molecules like CO, NO and H$_2$[70, 71, 72]. We did some preliminary work on hydrogen deuterium exchange, where we tried to desorb preadsorbed deuterium with hydrogen and thus use the amount of desorbed deuterium as a measure of the number of active sites. We had previously used the same technique in the same fuel cell setup to measure CO exchange reactions on Pt and PtRu alloys[27]. The MEA required humidification and thus the electrode was in an aqueous environment. The aqueous environment caused a continuous hydrogen/deuterium exchange between hydrogen from water molecules and the preadsorbed deuterium at a rate that was not zero. Thus preadsorbed deuterium would be exchanged with hydrogen from water and we were not able to use the amount of desorbed deuterium as measure of the number of active sites. We did also try to characterize the carbon supported particles with a transmission electron microscope(TEM) and realized that the contrast of the single layers of S-Mo-S was to low to be easily distinguished from the carbon support. Recent progress in high-angle annular dark-field scanning electron microscopy(HAADF-STEM) has however increased the contrast to a degree where it is possible to image the structure of single layers of MoS$_2$ on carbon[73]. The structure of the carbon supported MoS$_2$ had the same truncated triangular structure as previously found on Au(111) supported MoS$_2$[63]. But even with the ability to characterize the sample used in the fuel cell setup, the complexity of the MEA would make it hard to compare the activity of a series of samples with each other. Even small changes in for instance transport properties or MEA pressing temperature would cause change in activity that might be bigger than the changes introduced to the sample.

6.2 MoS$_2$ on Au(111)

MoS$_2$ on Au(111) has been studied extensively by Besenbacher et al[63, 64, 74, 75, 69] and it has been shown that the particles have the characteristic structure of a truncated hexagon on Au(111), graphite[73] and HOPG[76]. Thus the structure of MoS$_2$ on Au(111) should be similar to that on the high surface area graphite that was recently investigated for the HER[10].
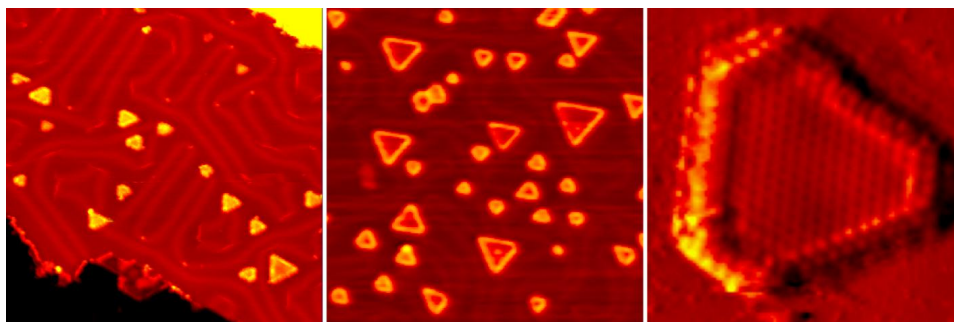

Figure 6.4: STM images of MoS$_2$ on Au(111), left, middle: 470 Å by 470 Å of MoS$_2$ with different coverage and particle size. Right: 60 Å by 60 Å image of a single MoS$_2$ particle showing the truncated triangle with the Mo-edge being the primarily exposed edge.

Electrochemical measurements on well defined surfaces has provided important information about surfaces and surface structures like facets[77], steps[78], stress and strain effects[79]. The combination of STM characterized samples and electrochemical measurements is a strong tool, providing information about the relation between structure and electrochemical behavior[80, 81, 82]. In order to gain further insight into the relation between structure and reactivity of the MoS$_2$ nanoparticles a series of samples of MoS$_2$ on Au(111) was prepared and characterized by the STM, see Figure 6.4. The samples were deliberately synthesized with different coverages and particle sizes such that effects on the activity stemming from coverage and particles sizes could be distinguished. The UHV prepared and characterized samples were after preparation tested in a three electrode cell especially designed to measure on single crystals.
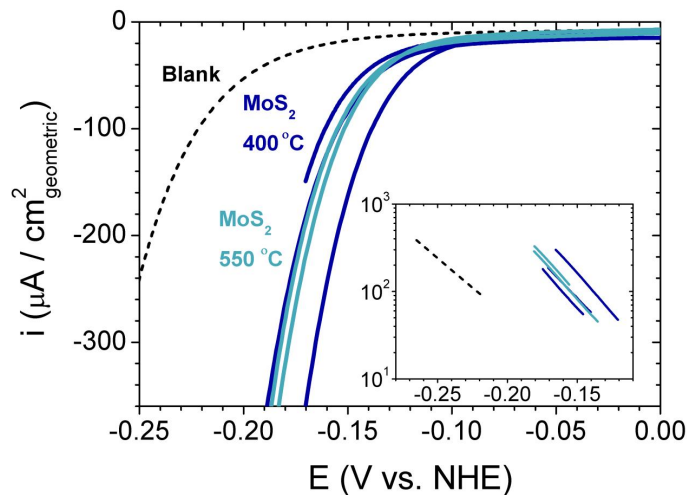
Figure 6.5: Polarization curves and tafel plots of the MoS_2 on Au(111) samples with different particle sizes and coverages, the measurements were done in 1 M H_2SO_4 with scanrate of 5 mV/s

Figure 6.5 shows how the electrochemical measurements are able to distinguish between the HER activity for differently prepared samples. We also find that the Tafel slope consistently is around 57 mV/dec. for the MoS_2 samples. This allows us to compare the exchange currents densities of the different samples with each other.
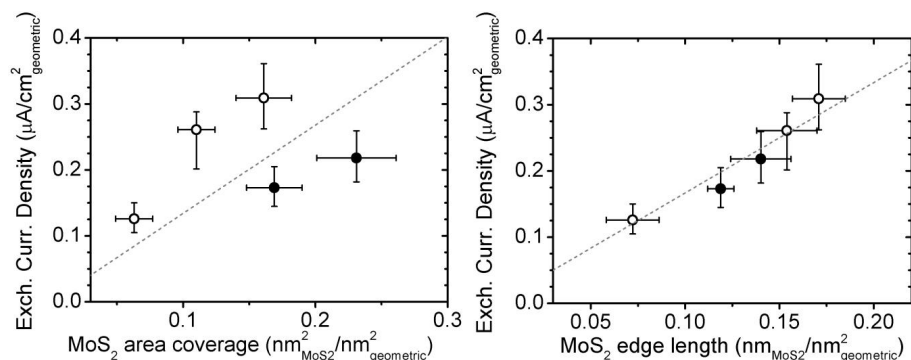
Figure 6.6: Left: the exchange current density as a function of the MoS$_2$ coverage. Right: The exchange current density as function of the edge lenght of the MoS$_2$ particles.

The exchange current densities were then plotted as a function of two different STM recorded sample characteristics, the surface coverage and the edge length of the particles, see Figure 6.6. The exchange current density the exchange current density is only a function of the edge lenght and not the coverage of the nano particulate MoS$_2$. It was thus concluded that the edge of MoS$_2$ as predicted by Hinnemann et al[10] indeed is the active site.
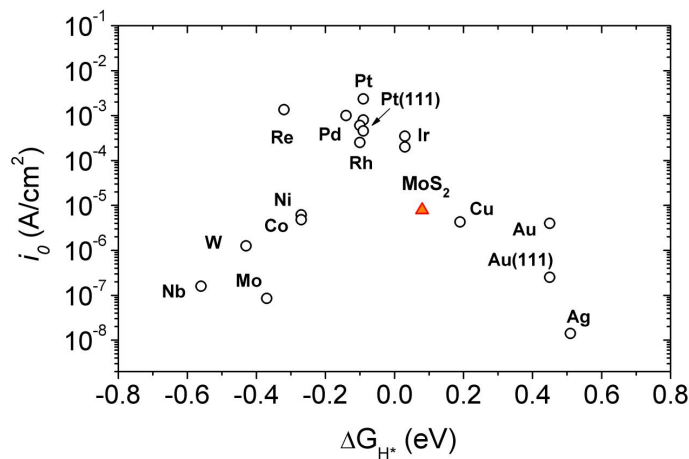
Figure 6.7: The volcano curve with MoS$_2$, the data is compiled from different references[9, 10]

With the knowledge of the active site and the number of active sites it was possible to estimate the exchange current density pr. cm^2 of MoS$_2$ edge.

This allowed for a direct comparison of the HER actvity of MoS_2 with that of other HER catalysts, see Figure 6.7. Note that the activity of MoS_2 is found to be just below that of the Pt family catalysts. For more details see **Paper 3**[83].

6.3 MoS$_2$ on Carbon

In parallel with the study of MoS$_2$ on Au(111), studies on carbon supported MoS$_2$ were also conducted, since the carbon supported MoS$_2$ is more commercially relevant. The carbon supported systems are as mentioned in section 6.1.1 more inhomogeneous and difficult to image. Since knowledge about the concentration of active sites is paramount in the eludication of structure-activity relationship, we aimed to use irreversible oxidation features of MoS$_2$ as the probe for number and types of active sites.

6.3.1 Preparation methods

The first step in such a study is the choice of host materials since a wrong choice could give rise to complications like contamination and transport limitations. Initially the MoS$_2$ was prepared on high surface area carbon powder, by means of wet impregnation of an aqueous solution ammonia-heptamolybdate. The sample was then calcined in air and sulfided at 450 ° C for 4 hours in a flow of 10 % H$_2$S in Hydrogen. The MoS$_2$ on the high surface area carbon was then bonded to an inert electrode with Nafion. Unfortunally severe transport limitations were experienced, when the sample was tested in 0.5 M H$_2$SO$_4$ in the three electrode setup. It was impossible to use our results as the Tafel slope literally were on the order of volts. We then decided to try a more planar support like Au(111), but since the sample would be heated to 450 °C the requirements to the cleanliness of the support material was high. One such clean material is highly orientated pyrolityc graphite which is known to be clean. Unfortunatelly HOPG is very inert and special treatment is required to bond MoS$_2$ to the surface[76, 10] and was thus rejected. We finally found that Toray carbon paper consisting of high temperature treated carbon fibres had the desired cleanliness and at the same time had enough defects to bond MoS$_2$.
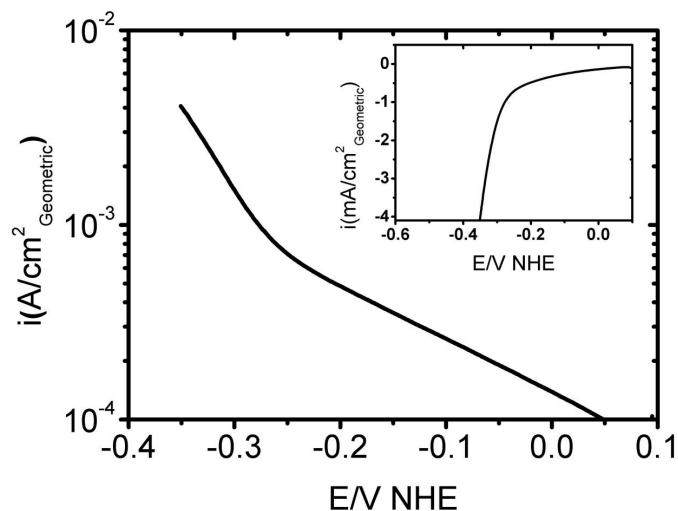
Figure 6.8: Tafel plot (main) and polarization curve (inset) in the cathodic potential range of MoS$_2$ supported on Toray paper. The Tafel slope in the HER region is found to be 120 mV/dec. this is in the expected range for the HER. The scanrate is 5 mV/s and the measurement was conducted in 0.5 M H$_2$SO$_4$.

Figure 6.8 shows a typical polarization curve and Tafel plot of MoS$_2$ supported on Toray paper, firstly it is noticed that hydrogen primeraly is evolved at potentials lower than -0.15 V just as on the other MoS$_2$ systems and we also find that the Tafel slope is around 120 mV/dec.. This value of the Tafel slope is in the expected region for the hydrogen evolution reaction, see section 2.2.2.

6.3.2 Measuring the area by oxidation

Early in our studies, we found that MoS$_2$ was irreveribly oxidyzed at anodic potentials higher than 0.6 vs. NHE, and we did several investigations of whether this feature could be used to determine or estimate the surface area or number of active sites on the carbon supported MoS$_2$ nanoparticles.

Figure 6.9 shows the oxidation of MoS$_2$ and the subsequent decrease in activity. The oxidation peak appears to have two different components a major component at approx. 0.98 V vs. NHE and a minor component at 0.7 V vs. NHE. This indicates that some parts of the MoS$_2$ is oxidized more easy than other parts. As it is known from literature that bulk MoS$_2$ is preferably oxidized at steps/edges[84], we interpret the two peaks as oxidation of the edge(minor) or the basal plane(major) of the MoS$_2$ nanoarticles. A back of the envelope calculation on triangles show that the relation be-
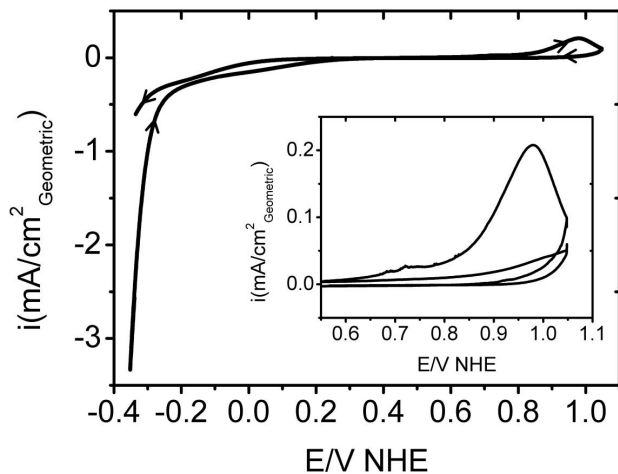
45

Figure 6.9: Cyclic voltammogram of the oxidation and subsequent deactivation of the MoS$_2$ sample in 0.5 M H$_2$SO$_4$. Scanrate 2mV/s. Main: The deactivation of the sample showing one sweep from -0.35 V vs. NHE to 1.05 V vs. NHE and back to -0.35 V vs. NHE. On the 1st anodic sweep an irreversible oxidation peak occurs at 0.6 V vs. NHE and is followed by a subsequent decrease in current at cathodic potentials (-0.35 V vs. NHE), indicating a deactivation of the active sites. Inset: The first and second sweep at anodic potentials showing a significant decrease in the oxidation peak.

tween major(basal plane area) and minor(edge area) peaks seen on Figure 6.9 corresponds to an approximate particle size of 25 nm. This is also in agreement with particle sizes of carbon supported MoS$_2$ reported by Brorson et al[73]. We also checked whether the size of the major oxidation peak was correlated with the amount of Mo used during the preparation of the sample. We found a correlation where approx. 8.9 electrons (r^2 = 0.55) where transferred during oxidation per Mo atom used in the synthesis.

6.3.3 XPS analysis

XPS analysis of the samples where also performed after synthesis and at different stages of electrochemical measurements. This would enable us to speculate further on the reaction mechanism in the oxidation of MoS_2.
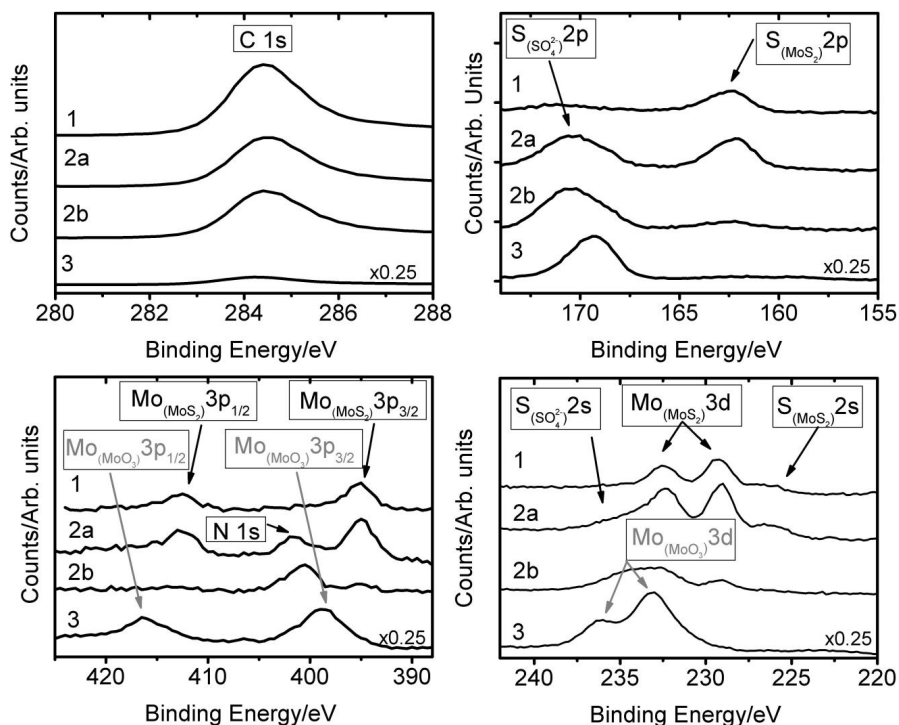

Figure 6.10: XPS spectra of MoS_2 on Toray paper recorded at different stages of its life. 1): As prepared after sulfidation. 2a): After initial activity measurements of the HER(CVs between +0.1 and -0.4 V vs. NHE). 2b): Sample 2a after measurements of the HER and subsequent oxidation/deactivation (CVs between +1.4 and -0.4 V vs. NHE) and removal from the electrolyte at -0.32 V vs. NHE. 3): After measurements of the HER and subsequent oxidation/deactivation (CVs between +1.4 and -0.4 V vs. NHE) and removal from the electrolyte 5 at 0.4 V vs. NHE.

In Figure 6.10 XPS spectra of MoS_2 before(1) and after(2a) HER measurements is not changing significantly apart from the adsorption of sulfate on the surface. The spectra are also comparable with spectra recorded on MoS2 on Au(111)[85]. The spectra does however change after oxidation at anodic potentials of up to 1.4 V vs. NHE, it is clear that the signals from Mo and S in MoS_2 are barely visible after oxidation. The exact product of the oxidation is more difficult to determine as the state of both pure Mo and S is

dependent on the electrochemical conditions[26]. A more detailed discussion of the exact products of the oxidation can be found in **Paper 4**[86], where it was proposed that the reaction mechanism was the following:

$$MoS_2 + 7H_2O \rightarrow MoO_3 + SO_4^{2-} + \frac{1}{2}S_2^{2-} + 14H^+ + 10e^- \qquad (6.1)$$
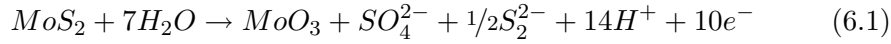
This proposed reaction path allows us to calculate an exchange current density per area MoS_2 of $1.1x10^{-6}$ A/cm^2, comparable with the $7.9x10^{-6}$ A/cm^2 per edge area found on MoS_2 on Au(111). The exchange current density on the carbon supported MoS_2 can be seen as a lower bound as we normalize with area of MoS_2 and not the area of the active sites on the MoS_2. If we assume that the particles as previously mentioned have a particle size of around 25 nm, the edge will be approx. 8% of the area, leading to an exchange current densite pr cm^2 active site that is 12 times higher than the reported exchange current densitty per area of the particle.

6.4 The other metal sulfides

Since MoS_2 is not the only metal sulfide with under-coordinated sulfur atoms that might have promising HER characteristica, we opted to test a whole series of different metal sulfides. The other sulfides were tested for the HER in the fuel cell setup where the initial HER measurements on MoS_2 were performed.
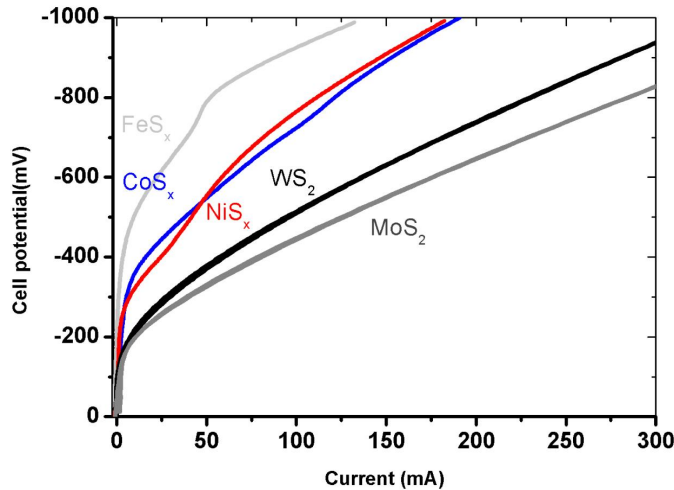

Figure 6.11: Polarisation on curve of the HER of different sulfides measured in the fuel cell setup with a scan rate of 5 mV/s and with a hydrogen flow of 20 mL/min. over both electrodes.

The initial measurements on a choice of metal sulfides are exhibited in Figure 6.11. It can be observed that WS_2 apparently evolves hydrogen almost as efficient as MoS_2 whereas the sulfides based on Fe, Ni and Co apparently are worse HER catalysts. WS_2 is interesting as it has been found to have the same triangular structure as MoS_2 on graphite[87] and has previously been suggested as a catalysts for the HER[88]. A sample synthesized using a similar procedure as used when MoS_2 was synthesized with the main difference being that ammonium metatungstate was used as the precursor.

Figure 6.12: A:Tafel and polarization curve(inset) of WS_2/C, scanrate 5 mV/s both the initial and the final stable scan is shown. B: CV of WS_2/C showing the deactivation of WS_2.

Figure 6.12 shows the electrochemical investigation of the carbon supported WS_2 nanoparticles. The WS_2 nanoparticles exhibit similar electrochemical characteristica to those previously found on MoS_2. The main difference is the Tafel slope that was found to be around to be 135 mV/dec. for this specific sample, but it can not be ruled out that this value will change if the synthesis procedure is further optimized.

6.5 Promotion of MoS$_2$ and WS$_2$

Promotion of MoS$_2$ by Co is known to have a effect on the HDS activity and this system has been studied extensively for decades[89, 90, 62]. Recently this system has also been studied using STM[75, 91] and TEM[73]. It is generally agreed that the promoter atoms are situated on the S-edge of MoS$_2$ [69, 62].
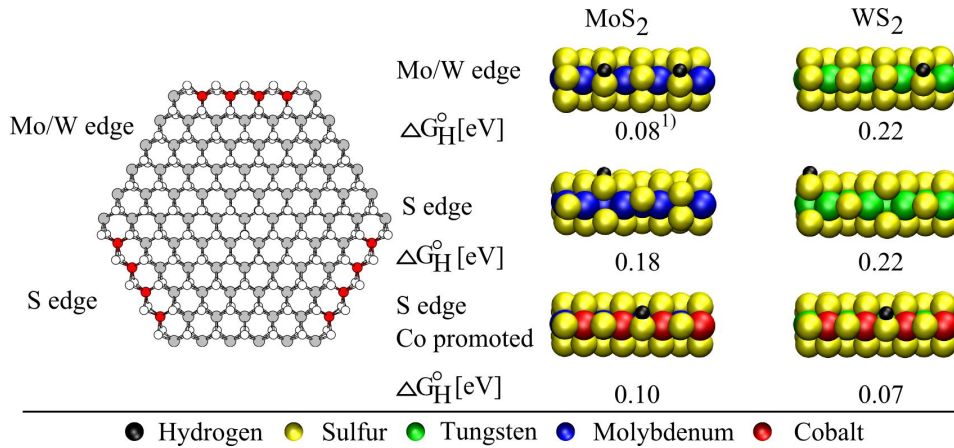
Figure 6.13: Left: Ball model of a Mo/WS2 particle exposing both S edge and Mo/W edge. Right: Differential free energies of hydrogen adsorption on the different edges. 1) from reference[10]

DFT calculations where used to estimate the effect of cobalt promoter atoms on the S-edge of MoS$_2$. The results of this calculation are summarized in Figure 6.13. For the unpromoted system the Mo-edge of MoS$_2$ ($\Delta G_H = 0.08$ eV) should have the highest activity, followed by the S-edge of MoS$_2$($\Delta G_H = 0.18$ eV) and the pure W and S-edge of WS$_2$($\Delta G_H = 0.2$ eV). The addition of Co to the S-edge of both the WS$_2$ and the MoS$_2$ shifts the value of ΔG_H to 0.07 eV and 0.1 eV respectively. Thus we should expect that the addition of Co has a promoting effect.
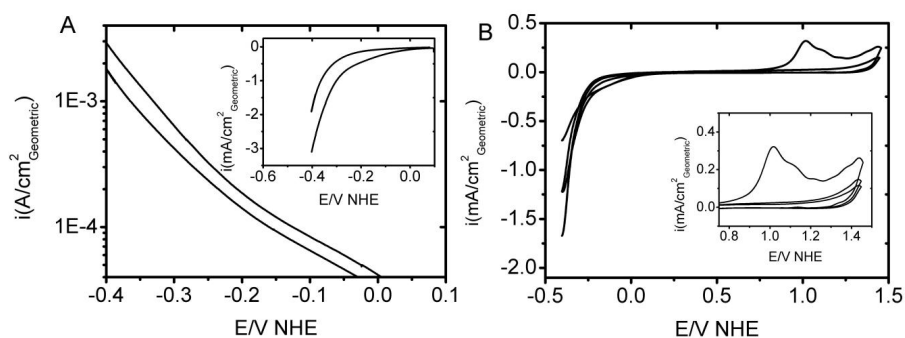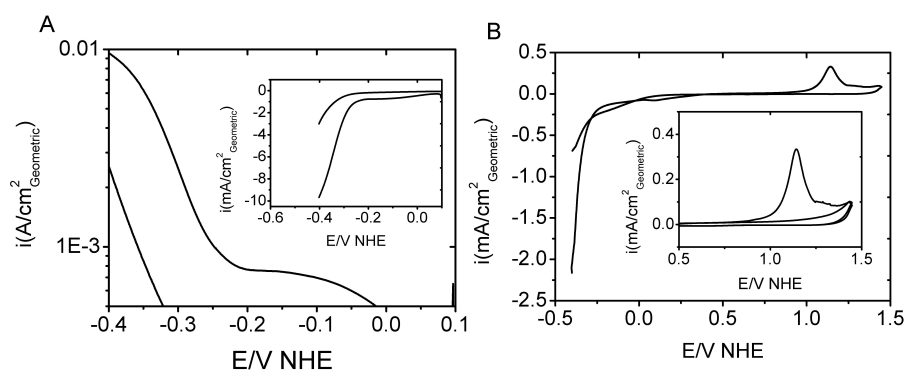
Figure 6.14: A:Tafel and polarization curve(inset) of CoS_x/C, both the initial and the final stable scan is shown. B: CV of CoSx/C showing the oxidation/deactivation of CoS_x.

The first system tested before any promotion experiments were conducted was the test of the HER on sulfided(same conditions as the MoS_2) Co acetate on torray paper, see Figure 6.14. The initial sweep towards chatodic potentials showed a promising HER current but on subsequent sweeps the activity degraded rapidly towards the activity of the Toray paper support. Thus is was concluded that CoS_x on its own was unstable under HER conditions.
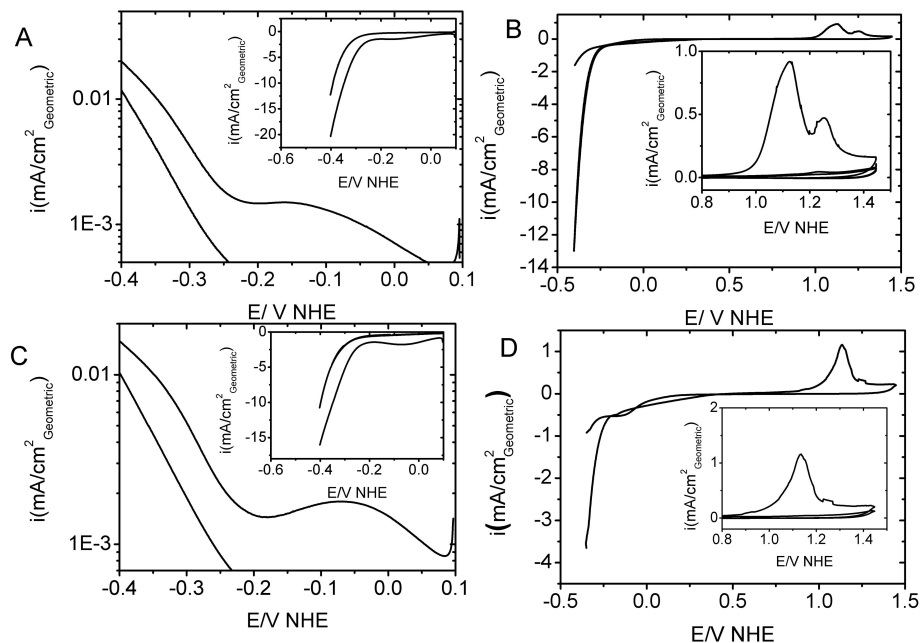
Figure 6.15: A,C:Tafel and polarization curve(inset) of Co-Mo-S(A) and Co-WS(C), the scan rate is 5 mV/S. Both the initial and the final stable scan is shown. B,D: CV of Co-Mo-S(B) and Co-W-S(D) showing the deactivation of Co-Mo-S and Co-W-S.

We tested the Co promoted MoS_2 (Co-Mo-S) and the Co promoted WS_2(Co-W-S) and it was found that the electrochemical behavior towards oxidation and hydrogen evolution was similar to that of the unpromoted catalysts, see Figure 6.15. In order to eludicate on whether there was an effect of the added Co we normalized the current with respect to the area of the respective oxidation peak(measured after HER measurements) of the specific samples.

Figure 6.16: Polarization curves where the currents of the different metal sulfides have been normalized with respect to the charge of the irreversible oxidation peak. A: Polarization curve of the HER on WS_2 and cobalt promoted WS_2(Co-W-S).B: Polarization curve of the HER on MoS_2 and cobalt promoted MoS_2(Co-Mo-S).
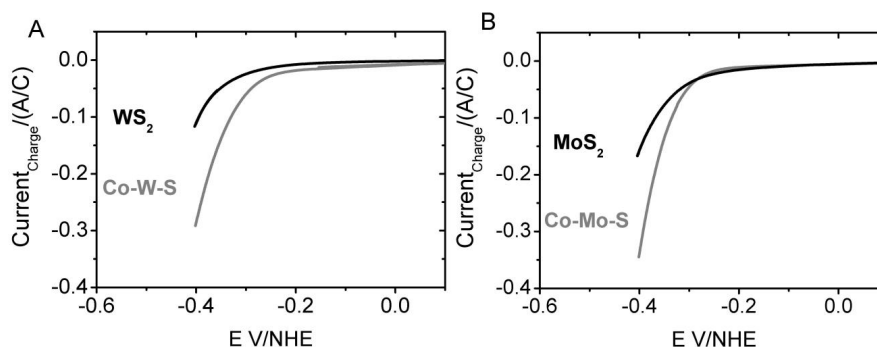
The polarization curves where the current had been normalized with respect to the area of the respective oxidation peaks(Figure 6.16) showed that there was an effect of Co promotion on both the WS_2 and MoS_2. If it is assumed that the particle size of the promoted and unpromoted metal sulfides are equal, we can explain the effect of the promotion in the following manner. The increase of the activity for the Co-Mo-S is due to the S-edge becoming just as active as the Mo-edge, and thus more active sites are created per particle. On the Co-W-S the S-edge is also becoming more active when Co is added and in this case a more active site is created. To sum up our findings it was found by DFT that the activity of the different edges should be WS_2 < MoS_2=Co-Mo-S < Co-W-S whereas the electrochemical measurements on the samples indicate that WS_2 < MoS_2< Co-W-S < Co-Mo-S. More details of the HER on metal sulfides are given in **Paper 4**[86].

6.6 Mo$_3$S$_4$

Mo$_3$S$_4$ is one of the smallest molecules available where under coordinated sulfur sites are present. This system is particularly interesting as it can be considered as a basic building block for metal sulfide systems.
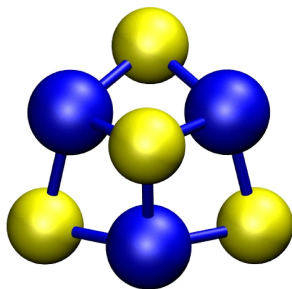
Figure 6.17: The Mo cluster consisting of three molybdenum atoms and four sulfur atoms assembled in an incomplete cubane structure.

The initial studies of the incomplete Mo$_3$S$_4$ cubanes were done in the fuel cell setup were the Mo$_3$S$_4$ clusters where deposited on high surface area carbon pressed into a MEA and tested for the HER.
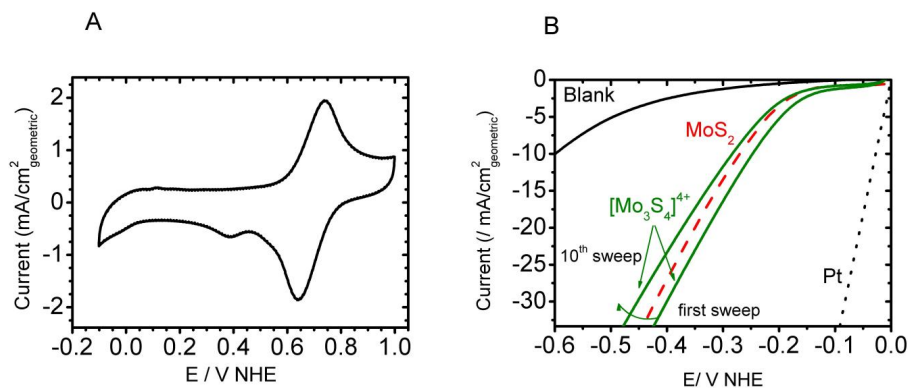
Figure 6.18: Electrochemical characterization of vulcan xc72 supported Mo$_3$S$_4$ in a membrane electrode assembly. The potential is measured with respect to a Pt electrode which serves as both the reference and the counter electrode. A: cyclic voltammogram in the anodic region, showing a reversible oxidation feature at ca. 0.7 V. B: Polarisation curves in the cathodic region where hydrogen is evolved. The activity of Mo$_3$S$_4$ is compared with a blank electrode only containing xc72, a sample with Pt and a sample with MoS$_2$. Hydrogen was passed over both electrodes and the scanrate was 5 mV/s.

The result of the initial measurements show that the Mo$_3$S$_4$ clusters show HER activity that is similar to MoS$_2$, see Figure 6.18. The data also shows

that the HER activity is lowered for each consecutive sweep. At the same time the Mo_3S_4 cluster does not seem to be subject to irreversible oxidation at high anodic potentials. Which is the case for the MoS_2.

Figure 6.19: Electrochemical characterization of the submonolayer of Mo_3S_4 on HOPG. Main: Polarization curve in the anodic region showing hydrogen evolution. The decrease in activity is most likely due to anodic desorption of the clusters. After a sweep to high cathodic potentials (1.2 V vs. NHE), the clusters desorb and the activity is only caused by the activated HOPG. Inset: the corresponding Tafel plot. The scanrate was 5 mV/s.
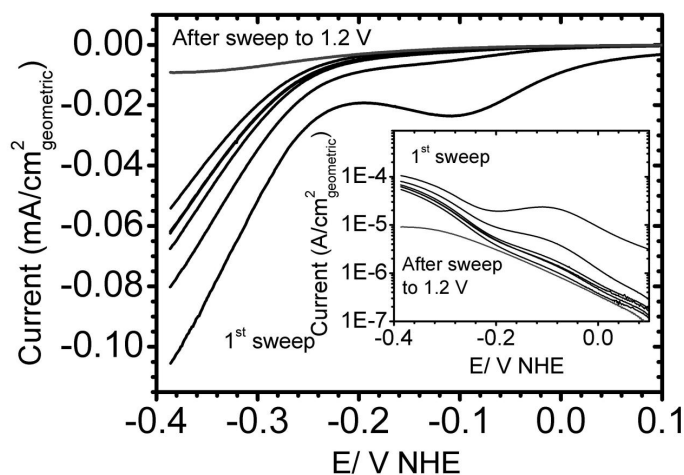
Just as in the study of $Au(111)$ supported MoS_2[92] we did electrochemical measurements on STM imaged samples, this time the support was activated HOPG with a submonolayer of Mo_3S_4. The measurements of the model system, see Figure 6.19, enables us calculate a turn over frequency per molecule, since the STM imaging resolved the number of Mo_3S_4 clusters on the surface of the HOPG. The turnover frequency per Mo_3S_4-molecule was found to be 0.07 s^{-1}. We do not know the exact number of active sites per Mo_3S_4-molecule, but this value is comparable to or even better than the turnover frequency of 0.02 s^{-1} reported for a single site on the edge of MoS_2 nanoparticles[83]. The turnover frequency is, however, smaller than for the turnover frequency per atom of the archetypical HER catalysts[8] (Pt, Pd). XPS studies were also conducted on the supported clusters and it was found that the outmost layer of the Mo_3S_4 had a Mo 3d peak at a higher binding energy than the bulk of the sample. It was also found that the loss of activity was due to slow cathodic desorption of the clusters and not an oxidation of the Mo_3S_4 clusters.

55

6.7   Hydrogen oxidation and metal sulfides

Some of the metal sulfides where also tested for the hydrogen oxidation reaction(HOR). It is well described that platinum effectively catalyzes the HER and the HOR[4] and according to the basic Butler Volmer reaction, see equation 2.1 a good HER catalyst should be a good HOR catalyst, assuming that $\alpha_a = \alpha_c = 0.5$.
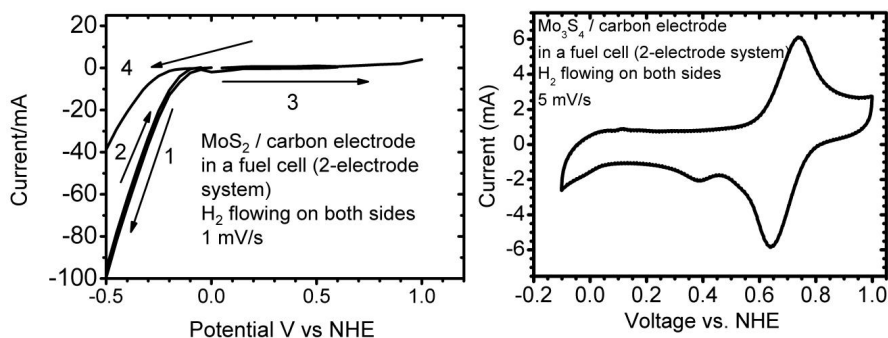
Figure 6.20: Left: The HER and the HOR on the carbon supported MoS_2. Right: CV of carbon supported Mo_3S_4 in the region where HOR is expected to occur.

In Figure 6.20 it is shown that neither MoS_2 nor Mo_3S_4 can oxidize hydrogen at measurable rates. The reason for this difference in the ability to catalyze the HER and the HOR could simply be that the two reactions have different free energy barriers due to different reaction paths. The reaction path for the HER could for instance be a Heyrovski mechanism whereas the HOR could happen via the Tafel mechanism. Similar effects can also be seen on the PtAu core shell system that was able to evolve hydrogen but at the same time not able to oxidize hydrogen, see Figure 5.9. This notion about the difference in reaction paths is also supported by a recent study[93] where the hydrogen deuterium exchange rate was used to calculate a the sticking probability of hydrogen on different metals. The catalyst with low values of ΔG_H apparently did not show the highest hydrogen deuterium exchange rates. Hopefully a more detailed study of the relation between the HER and the HOR could shed more light of these differences.

Chapter 7

Summary and outlook

In this thesis several alternative hydrogen evolution catalysts have been characterized and synthesized, some even to a degree where it was possible to correlate structure and reactivity of the catalysts.

Based on a computational screening for HER catalyst a BiPt surface alloy was identified as a possible HER catalyst. The alloy was synthesized,characterized and found to have a higher HER activity than pure Pt. The surface alloy was also found to be more CO tolerant than pure Pt.

Investigations of a core shell system consisting of a Pt skin on Au was found to exhibit Pt like HER activity after being exposed to high anodic potentials($>$1 V vs. NHE) and Au like HER activity at potentials below 1 V vs. NHE. The difference was ascribed as being a surface segregation effect.

MoS_2 nanoparticles were by DFT modeling found to have active sites similar to the active sites on the hydrogen evolving enzymes hydrogenase and nitrogenase. Carbon supported MoS_2 nanoparticles were synthesized and found to have a decent HER activity. In order to relate the structure of the MoS_2 to the HER activity, a series of electrochemical experiments were conducted on STM imaged MoS_2 supported on Au(111). These experiments corroborated the DFT calculations predicting that the edge of nanoparticulate MoS_2 is the active site for the HER.

Carbon supported MoS_2 was also synthesized and investigated for the HER. A method based on irreversible electrochemical oxidation of the MoS_2 was used to quantify the area of MoS_2, and it was found that the activity was comparable to the activity on MoS_2 supported on Au(111). WS_2 nanoparticles supported on carbon were also synthesized and characterized electrochemically. It was found that the HER activity of WS_2 was in the same region as the MoS_2. Inspired by Co promotion of WS_2 and MoS_2 in HDS catalysis, cobalt promoted carbon supported MoS_2 and WS_2 were synthesized and tested , in both cases Co was found to promote the HER.

Clusters of incomplete Mo_3S_4 cubane structures were also investigated for

their ability to catalyze the HER. Mo_3S_4 was found to catalyze the HER and characterization of samples that were previously imaged by STM allowed the calculation of the turn over frequency per Mo_3S_4 cluster.

Since computational screening methods have been shown as a strong tool to screen for HER catalyst, the next step would be to develop the model further in order to screen materials relevant for oxygen reduction reaction and the hydrogen oxidation reaction. The development of such a method is however not simple as for instance stability of the catalyst is far more crucial for ORR catalyst compared to the HER catalysts.
An other extention of the work in thesis could be to characterize metal sulfides that were imaged by means of high-angle annular dark-field scanning electron microscopy in order to get further information of structure reactivity relations. Finally further work on the Mo_3S_4 clusters could be of interest like the study of the effect of adding another metals to the incomplete cubane structure.

Bibliography

[1] M. S. Dresselhaus and I. L. Thomas. Alternative energy technologies. *Nature*, 414(6861):332–337, NOV 15 2001.

[2] http://platinum.matthey.com.

[3] Wolf Vielstich, Arnold Lamm, and Hubert A. Gasteiger. *Handbook of fuel cells : fundamentals, technology, and applications*. Wiley, Chichester, England ; Hoboken, N.J., 2003.

[4] J. O'M Bockris and Shahed U. M. Khan. *Surface electrochemistry : a molecular level approach*. Plenum, New York, 1993. John O'M. Bockris and Shahed U.M. Khan.; Includes bibliographical references and index.

[5] M. P. Andersson, T. Bligaard, A. Kustov, K. E. Larsen, J. Greeley, T. Johannessen, C. H. Christensen, and J. K. Nørskov. Toward computational screening in heterogeneous catalysis: Pareto-optimal methanation catalysts. *Journal of Catalysis*, 239(2):501–506, APR 25 2006.

[6] J. Sehested, K. E. Larsen, A. L. Kustov, A. M. Frey, T. Johannessen, T. Bligaard, M. P. Andersson, J. K. Nørskov, and C. H. Christensen. Discovery of technical methanation catalysts based on computational screening. *Topics In Catalysis*, 45(1-4):9–13, August 2007.

[7] J. Greeley and M. Mavrikakis. Alloy catalysts designed from first principles. *Nature Materials*, 3(11):810–815, November 2004.

[8] J. K. Nørskov, J. Rossmeisl, A. Logadottir, L. Lindqvist, J. R. Kitchin, T. Bligaard, and H. Jonsson. Origin of the Overpotential for Oxygen Reduction at a Fuel-Cell Cathode. *Journal of Physical Chemistry B - Condensed Phase*, 108(46):17886–17892, 2004.

[9] J. K. Nørskov, T. Bligaard, A. Logadottir, J. R. Kitchin, J. G. Chen, S. Pandelov, and U. Stimming. Trends in the exchange current for hydrogen evolution. *Journal of the Electrochemical Society*, 152(3):J23–J26, 2005.

[10] B. Hinnemann, P. G. Moses, J. Bonde, K. P. Jørgensen, J. H. Nielsen, S. Horch, I. Chorkendorff, and J. K. Nørskov. Biomimetic hydrogen evolution: MoS$_2$ Nanoparticles as Catalyst for Hydrogen Evolution. *Journal of the American Chemical Society*, 127:5308–5309, 2005.

[11] J. Greeley, T. F. Jaramillo, J. Bonde, I. B. Chorkendorff, and J. K. Nørskov. Computational high-throughput screening of electrocatalytic materials for hydrogen evolution. *Nature Materials*, 5(11):909–913, NOV 2006.

[12] J. L. Zhang, M. B. Vukmirovic, Y. Xu, M. Mavrikakis, and R. R. Adzic. Controlling the catalytic activity of platinum-monolayer electrocatalysts for oxygen reduction with different substrates. *Angewandte Chemie-International Edition*, 44(14):2132–2135, 2005.

[13] I. Chorkendorff and J. W. Niemanntsverdriet. *Concepts of Modern Catalysis And Kinetics*. Wiley-VCH, 2003.

[14] T. Erdey-Gruz and M. Volmer. The theory of hydrogen high tension. *Zeitschrift Fur Physikalische Chemie-Abteilung A-Chemische Thermodynamik Kinetik Elektrochemie Eigenschaftslehre*, 150(3/4):203–213, September 1930.

[15] J. Tafel. The polarisation of cathodic hydrogen development. *Zeitschrift Fur Physikalische Chemie–Stochiometrie Und Verwandtschaftslehre*, 50(6):641–712, February 1905.

[16] J. Heyrovsky. A theory of overpotential. *Recueil Des Travaux Chimiques Des Pays-Bas*, 46:582–585, 1927.

[17] N. M. Markovic, B. N. Grgur, and P. N. Ross. Temperature-dependent hydrogen electrochemistry on platinum low-index single-crystal surfaces in acid solutions. *Journal Of Physical Chemistry B*, 101(27):5405–5413, July 1997.

[18] E. Skulason, G. S. Karlberg, J. Rossmeisl, T. Bligaard, J. Greeley, H. Jonsson, and J. K. Nørskov. Density functional theory calculations for the hydrogen evolution reaction in an electrochemical double layer on the Pt(111) electrode. *Physical Chemistry Chemical Physics*, 9(25):3241–3250, 2007.

[19] K. C. Neyerlin, W. B. Gu, J. Jorne, and H. A. Gasteiger. Study of the exchange current density for the hydrogen oxidation and evolution reactions. *Journal Of The Electrochemical Society*, 154(7):B631–B635, 2007.

[20] P. Sabatier. Announcement. Hydrogenation and dehydrogenation for catalysis. *Berichte Der Deutschen Chemischen Gesellschaft*, 44:1984–2001, 1911.

[21] R. Parsons. The Rate of Electrolytic Hydrogen Evolution and the Heat of Adsorption of Hydrogen. *Transactions of the Faraday Society*, 54(7):1053–1063, 1958.

[22] H. Gerischer. Mechanismus der elektrolytischen Wasserstoffabscheidung und Adsorptionsenergie von atomarem Wasserstoff. *B. Soc. Chim. Belg.*, 67:506, 1958.

[23] B. E. Conway and J. O. Bockris. Electrolytic Hydrogen Evolution Kinetics And Its Relation To The Electronic And Adsorptive Properties Of The Metal. *Journal Of Chemical Physics*, 26(3):532–541, 1957.

[24] S. Trasatti. Work Function, Electronegativity, And Electrochemical Behavior Of Metals .3. Electrolytic Hydrogen Evolution In Acid Solutions. *Journal Of Electroanalytical Chemistry*, 39(1):163–&, 1972.

[25] J. Greeley, J. K. Nørskov, L. A. Kibler, A. M. El-Aziz, and D. M. Kolb. Hydrogen evolution over bimetallic systems: Understanding the trends. *Chemphyschem*, 7(5):1032–1035, MAY 12 2006.

[26] M. Pourbaix. *ATLAS OF ELECTROCHEMICAL EQUILIBRIA...* 1966.

[27] J. C. Davies, J. Bonde, A. Logadottir, J. K. Nørskov, and I. Chorkendorff. The ligand effect: CO desorption from Pt/Ru catalysts. *Fuel Cells*, 5(4):429–435, December 2005.

[28] NIST. NIST XPS database, http://srdata.nist.gov/xps/.

[29] J. R. Jennings, editor. *Catalytic Ammonia Synthesis: Fundamentals and Practice.*, volume ISBN 0306436280. Springer-Verlag, 1991.

[30] W. F. Maier, K. Stowe, and S. Sieg. Combinatorial and high-throughput materials science. *Angewandte Chemie-International Edition*, 46(32):6016–6067, 2007.

[31] M. Harute, N. Yamada, T. Kobayashi, and S. Iijima. Gold Catalysts Prepared By Coprecipitation For Low-Temperature Oxidation Of Hydrogen And Of Carbon-Monoxide. *Journal Of Catalysis*, 115(2):301–309, February 1989.

[32] T. V. W. Janssens, A. Carlsson, A. Puig-Molina, and B. S. Clausen. Relation between nanoscale Au particle structure and activity for CO oxidation on supported gold catalysts. *Journal Of Catalysis*, 240(2):108–113, June 2006.

[33] T. V. W. Janssens, B. S. Clausen, B. Hvolbæk, H. Falsig, C. H. Christensen, T. Bligaard, and J. K. Nørskov. Insights into the reactivity of supported Au nanoparticles: combining theory and experiments. *Topics In Catalysis*, 44(1-2):15–26, June 2007.

[34] O. Antoine, Y. Bultel, and R. Durand. Oxygen reduction reaction kinetics and mechanism on platinum nanoparticles inside Nafion (R). *Journal Of Electroanalytical Chemistry*, 499(1):85–94, February 2001.

[35] J. Greeley, J. Rossmeisl, A. Hellman, and J. K. Nørskov. Theoretical trends in particle size effects for the oxygen reduction reaction. *Zeitschrift Fur Physikalische Chemie-International Journal Of Research In Physical Chemistry & Chemical Physics*, 221(9-10):1209–1220, 2007.

[36] P. L. Hansen, J. B. Wagner, S. Helveg, J. R. Rostrup-Nielsen, B. S. Clausen, and H. Topsøe. Atom-resolved imaging of dynamic shape changes in supported copper nanocrystals. *Science*, 295(5562):2053–2055, March 2002.

[37] B. Hammer and J. K. Nørskov. Electronic factors determining the reactivity of metal surfaces. *Surface Science*, 343(3):211–220, December 1995.

[38] M. Mavrikakis, B. Hammer, and J. K. Nørskov. Effect of strain on the reactivity of metal surfaces. *Physical Review Letters*, 81(13):2819–2822, September 1998.

[39] V. Jalan and E. J. Taylor. Importance Of Interatomic Spacing In Catalytic Reduction Of Oxygen In Phosphoric-Acid. *Journal Of The Electrochemical Society*, 130(11):2299–2301, 1983.

[40] V. Stamenkovic, B. S. Mun, K. J. J. Mayrhofer, P. N. Ross, N. M. Markovic, J. Rossmeisl, J. Greeley, and J. K. Nørskov. Changing the activity of electrocatalysts for oxygen reduction by tuning the surface electronic structure. *Angewandte Chemie-International Edition*, 45(18):2897–2901, 2006.

[41] S. Koh, J. Leisch, M. F. Toney, and P. Strasser. Structure-activity-stability relationships of Pt-Co alloy electrocatalysts in gas-diffusion electrode layers. *Journal Of Physical Chemistry C*, 111(9):3744–3752, March 2007.

[42] V. R. Stamenkovic, B. S. Mun, K. J. J. Mayrhofer, P. N. Ross, and N. M. Markovic. Effect of surface composition on electronic structure, stability, and electrocatalytic properties of Pt-transition metal alloys: Pt-skin versus Pt-skeleton surfaces. *Journal Of The American Chemical Society*, 128(27):JA0600476, July 2006.

[43] J. Greeley and J. K. Nørskov. Large-scale, density functional theory-based screening of alloys for hydrogen evolution. *Surface Science*, 601(6):1590–1598, March 2007.

[44] T. J. Schmidt, V. R. Stamenkovic, C. A. Lucas, N. M. Markovic, and P. N. Ross. Surface processes and electrocatalysis on the Pt(hkl)/Bi-solution interface. *Physical Chemistry Chemical Physics*, 3(18):3879–3890, September 2001.

[45] R. Gomez, J. M. Feliu, and A. Aldaz. Effects of irreversibly adsorbed bismuth on hydrogen adsorption and evolution on Pt(111). *Electrochimica Acta*, 42(11):1675–1683, 1997.

[46] M. T. Paffett, C. T. Campbell, and T. N. Taylor. Adsorption And Growth Modes Of Bi On Pt(111). *Journal Of Chemical Physics*, 85(10):6176–6185, November 1986.

[47] F. Abild-Pedersen, J. Greeley, F. Studt, J. Rossmeisl, T. R. Munter, P. G. Moses, E. Skulason, T. Bligaard, and J. K. Nørskov. Scaling Properties of Adsorption Energies for Hydrogen-Containing Molecules on Transition-Metal Surfaces. *Physical Review Letters*, 99(1):016105, 2007.

[48] J. Zhang, K. Sasaki, E. Sutter, and R. R. Adzic. Stabilization of platinum oxygen-reduction electrocatalysts using gold clusters. *Science*, 315(5809):220–222, January 2007.

[49] M. O. Pedersen, S. Helveg, A. Ruban, I. Stensgaard, E. Lægsgaard, J. K. Nørskov, and F. Besenbacher. How a gold substrate can increase the reactivity of a Pt overlayer. *Surface Science*, 426(3):395–409, May 1999.

[50] E. Christoffersen, P. Liu, A. Ruban, H. L. Skriver, and J. Nørskov. Anode Materials for Low-temperature Fuel Cells: A Density Functional. *Journal of Catalysis*, 199, March 2001.

[51] B. L. Abrams, J. Bonde, P. C. K. Vesborg, T.F. Jaramillo, and I. Chorkendorff. Potential Dependent Surface Segregation Effects on Pt/Au. In preparation.

[52] M. W. W. Adams and E. I. Stiefel. Biochemistry - Biological hydrogen production: Not so elementary. *Science*, 282(5395):1842–1843, December 1998.

[53] D. J. Evans and C. J. Pickett. Chemistry and the hydrogenases. *Chemical Society Reviews*, 32(5):268–275, September 2003.

[54] J. B. Howard and D. C. Rees. Structural basis of biological nitrogen fixation. *Chemical Reviews*, 96(7):2965–2982, November 1996.

[55] D. C. Rees and J. B. Howard. The interface between the biological and inorganic worlds: Iron-sulfur metalloclusters. *Science*, 300(5621):929–931, May 2003.

[56] S. C. Lee and R. H. Holm. Speculative synthetic chemistry and the nitrogenase problem. *Proceedings Of The National Academy Of Sciences Of The United States Of America*, 100(7):3595–3600, April 2003.

[57] A. K. Jones, S. E. Lamle, H. R. Pershad, K. A. Vincent, S. P. J. Albracht, and F. A. Armstrong. Enzyme electrokinetics: Electrochemical studies of the anaerobic interconversions between active and inactive states of Allochromatium vinosum [NiFe]-hydrogenase. *Journal Of The American Chemical Society*, 125(28):8505–8514, July 2003.

[58] C. Tard, X. M. Liu, S. K. Ibrahim, M. Bruschi, L. De Gioia, S. C. Davies, X. Yang, L. S. Wang, G. Sawers, and C. J. Pickett. Synthesis of the H-cluster framework of iron-only hydrogenase. *Nature*, 433(7026):610–613, February 2005.

[59] T. B. Rauchfuss. Research on soluble metal sulfides: From polysulfido complexes to functional models for the hydrogenases. *Inorganic Chemistry*, 43(1):14–26, January 2004.

[60] P. E. M. Siegbahn. Proton and electron transfers in [NiFe] hydrogenase. *Advances In Inorganic Chemistry - Including Bioinorganic Studies, Vol 56*, 56:101–125, 2004.

[61] B. Hinnemann and J. K. Nørskov. Chemical activity of the nitrogenase FeMo cofactor with a central nitrogen ligand: Density functional study. *Journal Of The American Chemical Society*, 126(12):3920–3927, March 2004.

[62] H. Topsøe, B. S. Clausen, and F. E. Massoth. *Hydrotreating Catalysis*. Springer-Verlag, Berlin, 1996.

[63] S. Helveg, J. V. Lauritsen, E. Lægsgaard, I. Stensgaard, J. K. Nørskov, B. S. Clausen, H. Topsøe, and F. Besenbacher. Atomic-Scale Structure of Single-Layer MoS_2 Nanoclusters. *Physical Review Letters*, 84(5):951–954, 2000.

[64] M. V. Bollinger, K. W. Jacobsen, and J. K. Nørskov. Atomic and electronic structure of MoS_2 nanoparticles. *Physical Review B*, 67:085410, 2003.

[65] H. Tributsch. Solar Energy-Assisted Electrochemical Splitting of Water. *Zeitschrift Fur Naturforschung Section A-a Journal of Physical Sciences*, 32(9):972–985, 1977.

[66] W. Jaegermann and H. Tributsch. Interfacial Properties Of Semiconducting Transition-Metal Chalcogenides. *Progress In Surface Science*, 29(1-2):1–167, 1988.

[67] A. Nidola and R. Schira. New Sulfide Coatings For Hydrogen Evolution In Koh Electrolysis. *International Journal Of Hydrogen Energy*, 11(7):449–454, 1986.

[68] A. Sobczynski. Molybdenum-Disulfide As A Hydrogen Evolution Catalyst For Water Photodecomposition On Semiconductors. *Journal Of Catalysis*, 131(1):156–166, September 1991.

[69] F. Besenbacher, M. Brorson, B. S. Clausen, S. Helveg, B. Hinnemann, J. Kibsgaard, J. Lauritsen, P. G. Moses, J. K. Nørskov, and H. Topsøe. Recent STM, DFT and HAADF-STEM studies of sulfide-based hydrotreating catalysts: Insight into mechanistic, structural and particle size effects. *Catalysis Today*, 130(1):86–96, January 2008.

[70] N. Y. Topsøe and H. Topsøe. Adsorption Studies On Hydrodesulfurization Catalysts .1. Infrared And Volumetric Study Of No Adsorption On Alumina-Supported Co, Mo, And Co-Mo Catalysts In Their Calcined State. *Journal Of Catalysis*, 75(2):354–374, 1982.

[71] A. Travert, C. Dujardin, F. Maugé, S. Cristol, J. F. Paul, E. Payen, and D. Bougeard. Parallel between infrared characterisation and ab initio calculationsof CO adsorption on sulphided Mo catalysts. *Catalysis Today*, 70:255–269, 2001.

[72] E. J. M. Hensen, G. M. H. J. Lardinois, V. H. J. de Beer, J. A. R. van Veen, and R. A. van Santen. Hydrogen-deuterium equilibration over transition metal sulfide catalysts: On the synergetic effect in CoMo catalysts. *Journal Of Catalysis*, 187(1):95–108, October 1999.

[73] M. Brorson, A. Carlsson, and H. Topsøe. The morphology of MoS_2, WS_2, Co-Mo-S, Ni-Mo-S and Ni-W-S nanoclusters in hydrodesulfurization catalysts revealed. *Catalysis Today*, 123(1-4):31–36, MAY 30 2007.

[74] J. V. Lauritsen, J. Kibsgaard, S. Helveg, H. Topsøe, B. S. Clausen, E. Lægsgaard, and F. Besenbacher. Size-dependent structure of MoS2 nanocrystals. *Nature Nanotechnology*, 2(1):53–58, JAN 2007.

[75] J. V. Lauritsen, J. Kibsgaard, G. H. Olesen, P. G. Moses, B. Hinnemann, S. Helveg, J. K. Nørskov, B. S. Clausen, H. Topsøe, E. Lægsgaard, and F. Besenbacher. Location and coordination of promoter atoms in Co- and Ni-promoted MoS_2-based hydrotreating catalysts. *Journal of Catalysis*, 249(2):220–233, 2007.

[76] J. Kibsgaard, J. V. Lauritsen, E. Lægsgaard, B. S. Clausen, H. Topsøe, and F. Besenbacher. Cluster-support interactions and morphology of MoS_2 nanoclusters in a graphite-supported hydrotreating model catalyst. *Journal of the American Chemical Society*, 128(42):13950–13958, OCT 25 2006.

[77] R. R. Adzic, A. V. Tripkovic, and W. E. Ogrady. Structural Effects In Electrocatalysis. *Nature*, 296(5853):137–138, 1982.

[78] R. R. Adzic, A. V. Tripkovic, and V. B. Vesovic. Structural Effects In Electrocatalysis - Oxidation Of Formic-Acid And Hydrogen Adsorption On Platinum Single-Crystal Stepped Surfaces. *Journal Of Electroanalytical Chemistry*, 204(1-2):329–341, June 1986.

[79] L. A. Kibler, A. M. El-Aziz, R. Hoyer, and D. M. Kolb. Tuning reaction rates by lateral strain in a palladium monolayer. *Angewandte Chemie-International Edition*, 44(14):2080–2084, 2005.

[80] E. Herrero, J. M. Feliu, and A. Wieckowski. Scanning tunneling microscopy images of ruthenium submonolayers spontaneously deposited on a Pt(111) electrode. *Langmuir*, 15(15):4944–4948, July 1999.

[81] F. Hernandez and H. Baltruschat. Electrochemical characterization of gold stepped surfaces modified with Pd. *Langmuir*, 22(10):4877–4884, May 2006.

[82] J. Meier, K. A. Friedrich, and U. Stimming. Novel method for the investigation of single nanoparticle reactivity. *Faraday discussions*, 121:365–372, 2002.

[83] T. F. Jaramillo, K. P. Jørgensen, J. Bonde, J. H. Nielsen, S. Horch, and I. Chorkendorff. Identification of active edge sites for electrochemical H_2 evolution from MoS_2 nanocatalysts. *Science*, 317(5834):100–102, JUL 6 2007.

[84] W. Kautek and H. Gerischer. Anisotropic photocorrosion of n-type MoS_2 $MoSe_2$, and WSe_2 single crystal surfaces: the role 0f cleavage steps, line and screw dislocations. *Surface Science*, 119(1):46–60, 7/1 1982.

[85] J. H. Nielsen, K. P. Jørgensen, J. Bonde, K. Nielsen, L. Bech, Y. Tison, S. Horch, T. F. Jaramillo, and I. Chorkendorff. XPS and STM on MoS_2 on Au(111). In preparation, 2008.

[86] J. Bonde, P. G. Moses, T. F. Jaramillo, J. K. Nørskov, and I. Chorkendorff. Hydrogen Evolution on Nano-particulate Transition Metal Sulfides. *accepted Faraday discussions*, 2008.

[87] A. Carlsson, M. Brorson, and H. Topsøe. Morphology of WS_2 nanoclusters in WS_2/C hydrodesulfurization catalysts revealed by high-angle annular dark-field scanning transmission electron microscopy (HAADF-STEM) imaging. *Journal of Catalysis*, 227(2):530–536, OCT 25 2004.

[88] A. Sobczynski, A. Yildiz, A. J. Bard, A. Campion, M. A. Fox, T. Mallouk, S. E. Webber, and J. M. White. Tungsten Disulfide - a Novel Hydrogen Evolution Catalyst for Water Decomposition. *Journal of Physical Chemistry*, 92(8):2311–2315, APR 21 1988.

[89] B. S. Clausen, S. Mørup, H. Topsøe, and R. Candia. Mössbauer studies of the activated state of Co-Mo Hydrodesulfurization Catalysts. *Journal De Physique*, 37(12):6–249–6–252, 1976.

[90] I. Alstrup, I. Chorkendorff, R. Candia, B. S. Clausen, and H. Topsøe. A Combined X-Ray Photoelectron and Mössbauer Emmission Spectroscopy Study of the State of Cobalt in Sulfided,Supported,and Unsupported Co-Mo Catalysts. *Journal of Catalysis*, 77:397–409, 1982.

[91] J. V. Lauritsen, S. Helveg, E. Lægsgaard, and I. Steensgaard. Atomic-Scale Structure of Co-Mo-S Nanoclusters in Hydrotreating. *Journal of Catalysis*, 197, 2001.

[92] T. F. Jaramillo, J. Bonde, J. Zhang, B. L. Ooi, K. Andersson, J. Ulstrup, and I. Chorkendorff. Hydrogen evolution on supported $[Mo_3S_4]^{4+}$ cubane type electrocatalysts. Submitted, Journal of Physical Chemistry C, 2008.

[93] M. Johansson, O. Lytken, and I. Chorkendorff. The sticking probability for H-2 on some transition metals at a hydrogen pressure of 1 bar. *Journal Of Chemical Physics*, 128(3):034706, January 2008.

Included Publications

Paper 1:

"Biomimetic Hydrogen Evolution"
B. Hinneman, P. G. Moses, <u>J. Bonde</u>, K. P. Jørgensen, S. Horch, J. H.
Nielsen , I. Chorkendorff and J.K. Nørskov,
Journal of the American Chemical Society , **127**, 5308 (2005)

Included Publications

Biomimetic Hydrogen Evolution: MoS₂ Nanoparticles as Catalyst for Hydrogen Evolution

Berit Hinnemann, Poul Georg Moses, Jacob Bonde, Kristina P. Jørgensen, Jane H. Nielsen,
Sebastian Horch, Ib Chorkendorff, and Jens K. Nørskov*

*Center for Atomic-scale Materials Physics, Department of Physics, NanoDTU, Technical University of Denmark,
DK-2800 Lyngby, Denmark*

Received January 24, 2005; E-mail: norskov@fysik.dtu.dk

The electrochemical hydrogen evolution process whereby protons and electrons are combined into molecular hydrogen is catalyzed most effectively by the Pt group metals.[1] The interest in hydrogen evolution catalysts is currently increasing, as molecular hydrogen, H_2, is being considered as an energy carrier.[2] Unlike the hydrocarbon fuels used today, hydrogen produces only water during oxidation, for instance in a fuel cell. For hydrogen to be a real alternative to hydrocarbons, it must be produced in a sustainable fashion. One possibility is to use sunlight directly or indirectly (through wind power, for instance) to split water.[2] This requires an efficient catalyst for hydrogen evolution, preferably based on materials that are cheap and abundant. It is therefore important to find alternatives to the Pt group metals.

Hydrogenases and nitrogenases are also effective catalysts for the hydrogen evolution process[3,4] even though the catalytically active site of these enzymes contains the much less noble metals Fe, Ni, and Mo. Recently it has become possible to anchor hydrogenase to an electrode surface,[5] and considerable progress has been made in the synthesis of compounds in solution resembling the hydrogenase active site and showing activity for hydrogen evolution.[6]

In the present communication, we use density functional calculations to guide us to a new inorganic analogue of the other hydrogen-producing enzyme, nitrogenase. We analyze the difference between the metallic and the biological catalysts and show that in terms of being able to stabilize intermediates involving atomic hydrogen they have very similar properties. This allows us to identify a parameter determining whether a certain compound will be suitable as a catalyst in electrochemical hydrogen evolution, and it provides an efficient way to search for new systems.

Most water-splitting processes rely on electrochemical hydrogen evolution $2H^+ + 2e^- \rightarrow H_2$ in the final step. The hydrogen evolution reaction must in the first step involve bonding of hydrogen to the catalyst $H^+ + e^- + * \rightarrow H^*$, where * denotes a site on the surface able to bind to hydrogen. The second step is the release of molecular hydrogen through one of the two processes:[1] $2H^* \rightarrow H_2 + 2*$ or $H^+ + e^- + H^* \rightarrow H_2 + *$.

Using density functional theory (DFT) calculations, we can elucidate the thermochemistry (which is independent on the precise mechanism of the second step) of the reaction; see Figure 1.[7] By calculating the free energy of atomic hydrogen bonding to the catalyst, one can compare different metal surfaces as catalysts. For a chemical process to proceed at or around room temperature, no reaction step can be associated with large changes in the free energy. This immediately excludes the metals that form strong bonds to atomic hydrogen (Ni and Mo in Figure 1) as good catalysts because the hydrogen release step will be slow. Metals that do not bind to atomic hydrogen (Au in Figure 1) are also excluded because here the proton/electron-transfer step will be thermodynamically uphill
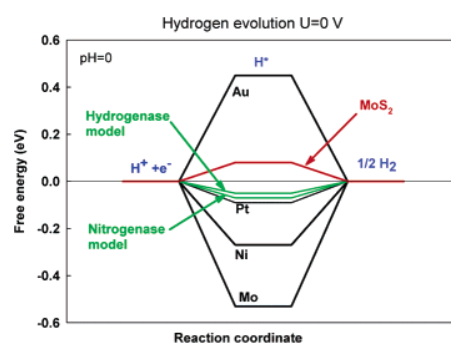

Figure 1. Calculated free energy diagram for hydrogen evolution at a potential $U = 0$ relative to the standard hydrogen electrode at pH = 0. The free energy of $H^+ + e^-$ is by definition the same as that of $^1/_2 H_2$ at standard conditions. The free energy of H atoms bound to different catalysts is then found by calculating the free energy with respect to molecular hydrogen including zero-point energies and entropy terms. The comparison of different elemental metals is taken from ref 7. The results for hydrogenase are from ref 11. The included result for MoS₂ is the free energy required to increase the hydrogen coverage from 25 to 50%; see Figure 2.
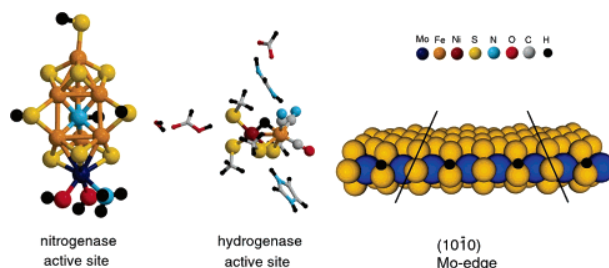

Figure 2. (Left) Nitrogenase FeMo cofactor (FeMoco) with three hydrogen atoms bound at the equatorial μ_2S sulfur atoms. (Middle) Hydrogenase active site with one hydrogen atom bound. The structure is taken from ref 11. (Right) MoS₂ slab with sulfur monomers present at the Mo edge. The coverage is 50%, i.e., hydrogen is bound at every second sulfur atom. The lines mark the dimension of the unit cell in the x-direction.

and therefore slow. There could be extra energy barriers associated with the proton-transfer steps or H_2 recombination, but independent of this it is a necessary, but not sufficient, criterion for a material to be a good catalyst that the free energy of adsorbed H is close to that of the reactant or product (i.e., $\Delta G_H^\circ \cong 0$). This principle can explain available experimental observations regarding metals as catalysts and electrode materials for hydrogen evolution.[7]

It is interesting to apply the same analysis to the active sites in nitrogenases and hydrogenases. For nitrogenase we have considered the model of the active site, the FeMo cofactor (FeMoco) shown in Figure 2.[8] We find that hydrogen atoms can only bind exothermically to the three equatorial sulfur ligands (μ_2S ligands) on the FeMoco. When the free energy of hydrogen atoms bound to the equatorial sulfur of the FeMoco is included in Figure 1, it
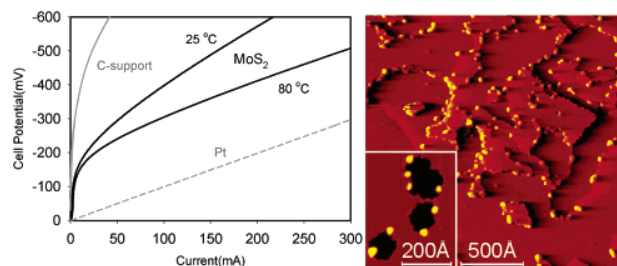
Figure 3. (Left) Polarization curve for hydrogen evolution on Pt, daihope C-support, and MoS_2 cathodes. The polarization curves for Pt and C support are made at 25 °C. The potentials are measured with respect to a carbon-supported Pt anode in a proton exchange membrane electrode assembly. (Right) STM images of MoS_2 nanoparticles on modified graphite.

results in a binding energy close to that of Pt. The FeMoco thus complies with the $\Delta G_H^\circ \cong 0$ requirement.[9] A number of researchers have performed computational studies of hydrogenase,[10,11] and the results obtained by Siegbahn[11] allow us to calculate the atomic hydrogen adsorption free energy for a [NiFe]-hydrogenase system. The Siegbahn model for the hydrogenase active site is shown in Figure 2. When the free energy is included in Figure 1, one can see that hydrogenase also fulfils the $\Delta G_H^\circ \cong 0$ requirement and fulfils it best for all considered systems.[9]

We therefore conclude that ΔG_H° is a good descriptor of materials that can catalyze hydrogen evolution and applies to a broad range of systems, both metals and enzymes. This means that we can use the same calculations to search for other systems, which could be candidates as catalysts for hydrogen evolution. One compound we have found computationally to obey the criterion is MoS_2; see Figure 1. Comparing the nitrogenase active site and the MoS_2 edge structure, we see that they bear a close resemblance, as shown in Figure 2. In both structures, the sulfur atom, which binds the hydrogen, is 2-fold coordinated to metal atoms, either to molybdenum or to iron. Only the edges of MoS_2 are interesting in this context, as the basal plane of MoS_2 is catalytically inactive.[12] The first H that bonds to the edge is strongly bound, but at an H coverage above 0.25, the differential free energy of adsorption is 0.1 eV. According to the calculations, additional H atoms should then be able to adsorb with a low barrier or, equivalently, a low overpotential of the order 0.1 V. A good material would be nanometer-large MoS_2 crystallites supported on, for example, graphite, which is conducting but otherwise inert. Such materials are used as catalysts for hydrotreating (hydrogenation of sulfur compounds in crude oil[13]), and methods for their preparation can be found in the literature.[14] It is indeed possible to prepare nanosized MoS_2 clusters on a graphite support, as can be seen in the scanning tunnel microscope (STM) image shown in Figure 3. The MoS_2 nanoparticles are approximately 4 nm in diameter and 1 nm in apparent height, and nucleate along the graphitic steps.

We have tested experimentally whether MoS_2 nanoparticles supported on carbon can be used as catalyst for electrochemical hydrogen evolution. This was done by preparing a membrane electrode assembly (MEA), based on a Nafion proton exchange membrane, with a standard platinum electrode on one side and a MoS_2/graphite electrode on the other side. By having the same hydrogen pressure on both sides, we could make the electrochemical measurements using a Parstat 2273 potentiostat resulting in the $I-V$ curve shown in Figure 3. The experimental approach has been used successfully in other studies.[15] The conditions of the experiment correspond to pH = 0 as in the calculations. As shown in Figure 3, MoS_2/graphite is a quite reasonable material for hydrogen evolution with an overpotential in the range 0.1−0.2 V.

We note that MoS_2 has been found to be a promoter for the hydrogen evolution activity of NiS_x electrodes,[16] which can be understood from our findings. Furthermore, MoS_2 has been tested for photocatalytic hydrogen evolution and shows activity but with significantly lower currents.[17]

Our findings suggest that we can begin searching for new catalytic materials using quantum chemical methods. The MoS_2 nanoparticles supported on graphite may be an example of a new class of electrode materials.

Supporting Information Available: Details of the DFT calculations, experimental setup, and obtained data. This material is available free of charge via the Internet at http://pubs.acs.org.

References

(1) (a) Trasatti, R. S. *J. Electroanal. Chem.* **1972**, *39*, 163. (b) Bockris, J. O'M.; Reddy, A. K. N.; Gamboa-Aldeco, M. *Modern Electrochemistry 2A* 2nd ed.; Kluwer Academic/Plenum Publishers: New York, 1998.
(2) Dresselhaus, M. S.; Thomas, I. L. *Nature* **2001**, *414*, 332.
(3) (a) Evans, D. J.; Pickett C. J. *Chem. Soc. Rev.* **2003**, *32*, 268. (b) Vollbeda, A.; Fontecilla-Camps, J. C. *J. Chem. Soc., Dalton Trans.* **2003**, *21*, 4030.
(4) (a) Rees, D. C.; Howard, J. B. *Science* **2003***, 300*, 929. (b) Lee, S. C.; Holm, R. H. *Proc. Natl. Acad. Sci. U.S.A.* **2003**, *100*, 3595.
(5) Lamle, S. E.; Vincent, K. A.; Halliwell, L. M.; Albracht, S. P. J.; Armstrong, F. A. *J. Chem. Soc., Dalton Trans.* **2003**, *21*, 4152.
(6) (a) Rauchfuss, T. B. *Inorg. Chem.* **2004**, *43*, 14. (b) Meija-Rodriguez, Chong, D.; Reibenspies, J. H.; Soriaga, M. P.; Darensbourg, M. Y. *J. Am. Chem. Soc.* **2004**, *126*, 12004. (c) Razavet, M.; Davies, S. C.; Hughes, D. L.; Barclay, J. E.; Evans, D. J.; Fairhurst, S. A.; Liu, X.; Pickett, C. *J. Chem. Soc., Dalton Trans.* **2003**, *4*, 586.
(7) Nørskov, J. K.; Bligaard, T.; Logadóttir, Á.; Kitchin, J. R.; Chen, J. G.; Pandelov, S.; Stimming, U. *J. Electrochem. Soc.* **2005**, *152*. J23.
(8) Hinnemann, B.; Nørskov, J. K. *J. Am. Chem. Soc.* **2004**, *126*, 3920.
(9) The difference in pH and chemical potential for electron transfer is of the same order and cancel each other; see Supporting Information.
(10) (a) Cao, Z.; Hall, M. B. *J. Am. Chem. Soc.* **2001**, *123*, 3734. (b) Liu, Z.-P.; Hu, P. *J. Chem. Phys.* **2002**, *117*, 8177. (c) Bruschi, M.; Fantucci, P.; De Goia, L. *Inorg. Chem.* **2004**, *43*, 3733.
(11) Siegbahn, P. E. M. *Adv. Inorg. Chem.* **2004**, *56*, 101.
(12) Raybaud, P.; Hafner, J.; Kresse, G.; Kasztelan, S.; Toulhoat, H. *J. Catal.* **2000**, *189*, 129.
(13) Topsøe, H.; Clausen, B. S.; Massoth, F. E. *Hydrotreating Catalysis−Science and Technology*, Springer-Verlag: Berlin, 1996.
(14) Chorkendorff, I.; Niemantsverdriet, J. W. *Concepts of Modern Catalysis and Kinetics*; Wiley-VCH: New York, 2003.
(15) Davies, J. C.; Nielsen, R. M.; Thomsen, L. B.; Chorkendorff, I.; Logadóttir, Á.; Łodziana, Z.; Nørskov, J. K.; Li, W. X.; Hammer, B.; Longwitz, S. R.; Schnadt, J.; Vestergaard, E. K.; Vang, R. T.; Besenbacher, F. *Fuel Cells* **2004**, *4*, 309.
(16) Nidola, A.; Schira, R. *Int. J. Hydrogen Energy* **1986**, *11*, 449.
(17) Sobczynski, A. *J. Catal.* **1991**, *131*, 156.

JA0504690

Paper 2:

"Computational high-throughput screening of electrocatalytic materials for
hydrogen evolution"
J. Greeley, T. F. Jaramillo, <u>J. Bonde</u>, I. Chorkendorff and J. K. Nørskov,
Nature Materials, **5**, 909 (2006)

Included Publications

Computational high-throughput screening of electrocatalytic materials for hydrogen evolution

JEFF GREELEY[1], THOMAS F. JARAMILLO[2], JACOB BONDE[2], IB CHORKENDORFF[2] AND JENS K. NØRSKOV[1]*

[1] Center for Atomic-scale Materials Design, NanoDTU, Department of Physics, Technical Univ. of Denmark, DK-2800 Kongens Lyngby, Denmark
[2] Center for Individual Nanoparticle Functionality, NanoDTU, Department of Physics, Technical Univ. of Denmark, DK-2800 Kongens Lyngby, Denmark
*e-mail: norskov@fysik.dtu.dk

The pace of materials discovery for heterogeneous catalysts and electrocatalysts could, in principle, be accelerated by the development of efficient computational screening methods. This would require an integrated approach, where the catalytic activity and stability of new materials are evaluated and where predictions are benchmarked by careful synthesis and experimental tests. In this contribution, we present a density functional theory-based, high-throughput screening scheme that successfully uses these strategies to identify a new electrocatalyst for the hydrogen evolution reaction (HER). The activity of over 700 binary surface alloys is evaluated theoretically; the stability of each alloy in electrochemical environments is also estimated. BiPt is found to have a predicted activity comparable to, or even better than, pure Pt, the archetypical HER catalyst. This alloy is synthesized and tested experimentally and shows improved HER performance compared with pure Pt, in agreement with the computational screening results.

The *in silico* design of functional materials on the basis of electronic-structure calculations is a longstanding goal of theoretical materials science. Such an effort would require the establishment of a direct link between the macroscopic functionality and the atomic-scale properties of the material, in addition to the development of efficient and accurate methods for solving the electronic-structure problem. The first examples of the use of computational methods to screen for new materials have recently been published[1–10]. Such calculations are computationally demanding, and these studies have generally either used simplified electronic-structure schemes or have considered relatively few material combinations. In the present article, we show that it is possible to carry out moderately large-scale combinatorial screening for alloy catalyst materials using density functional theory (DFT) calculations. We introduce a screening procedure that efficiently combines catalytic activity criteria, detailed stability assessments and a database of DFT calculations on more than 700 binary transition-metal surface alloys. We apply the procedure to the evaluation of alloy catalysts for a fundamental electrochemical process, the hydrogen evolution reaction (HER). One of the most promising candidate materials resulting from the search is a surface alloy of bismuth and platinum. We develop a method to synthesize a BiPt surface alloy and show experimentally that its activity is superior to that of Pt, the archetypical HER catalyst.

The HER, which involves proton reduction and concomitant hydrogen evolution, is important for a variety of electrochemical processes, and technological interest in the HER is spread over applications as diverse as hydrogen fuel cells, electrodeposition and corrosion of metals in acids and storage of energy via H_2 production[11–13]. We choose the HER to illustrate our approach primarily because a simple atomic-scale descriptor for the catalytic activity has previously been established. It has long been known that when the catalytic activity of a material for the HER is plotted as a function of the hydrogen–metal bond strength, a volcano-shaped form is found[14–18]. This behaviour is related to the Sabatier
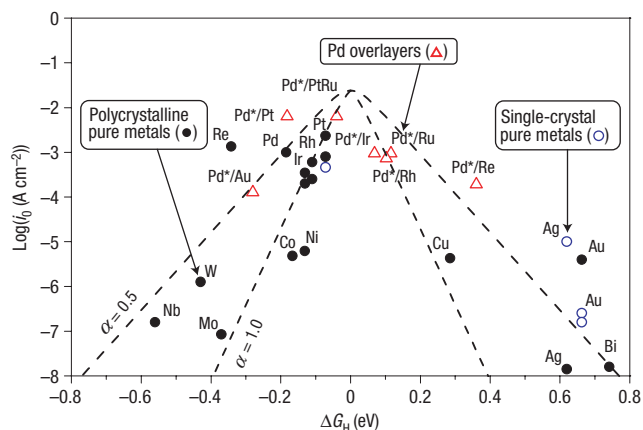
Figure 1 **Volcano plot for the HER for various pure metals and metal overlayers.** ΔG_H values are calculated at 1 bar of H_2 (298 K) and at a surface hydrogen coverage of either 1/4 or 1/3 ML. Experimental data are compiled in refs 17,20,21. Where available, computational data are taken from the present work; other computational results are taken from the references above. The experimental data have been collected from over 40 years of publications, representing different experimental conditions and surface structures. No corrections for changes in the calculated ΔG_H values with coverage are included, in contrast to the calculated values for Pd overlayers (denoted by Pd*/substrate) presented in ref. 21. The two curved lines correspond to the activity predictions of simple mean-field, microkinetic models, assuming transfer coefficients (α) of 0.5 and 1.0, respectively.

Figure 2 **Schematic diagrams of surface alloys at the solute coverages for which calculations are carried out.** The solute atoms are shown in white, and the host (substrate) atoms are indicated in dark green. All solute atoms are embedded in the surface layer of the corresponding host metal. **a**, A pure metal. **b**, A surface alloy with solute coverage = 1/3 ML. **c**, A surface alloy with solute coverage = 2/3 ML. **d**, One ML of solute atoms, forming an overlayer.

principle, a general explanatory paradigm in heterogeneous catalysis and electrocatalysis that states that optimal catalytic activity can be achieved on a catalytic surface with intermediate binding energies (or free energies of adsorption) for reactive intermediates[19]. If the intermediates bind too weakly, it is difficult for the surface to activate them, but if they bind too strongly, they will occupy all available surface sites and poison the reaction; intermediate binding energies permit a compromise between these extremes. In the particular case of hydrogen evolution, it turns out that these general principles can be quantified by analysing the free energy of hydrogen adsorption ΔG_H; this quantity is a reasonable descriptor of hydrogen evolution activity for a wide variety of metals and alloys[15,20,21]. As first suggested by Parsons[15], the optimum value should be around $\Delta G_H = 0$. In Fig. 1, we have plotted experimentally measured HER exchange current densities[17,20,21] against ΔG_H values calculated using DFT (see below). Although there is some scatter in the data (the experimental values are from several different authors), the figure seems to suggest that an optimum in the measured HER exchange current densities is found for DFT-derived ΔG_H values very close to (if not identically equal to) zero. We have therefore adopted the approach of using calculated values of $|\Delta G_H|$ to search for new HER catalysts, and we will assume in the following that the closer $|\Delta G_H|$ is to zero, the better the catalyst.

Using periodic $((\sqrt{3} \times \sqrt{3})R30°$ unit cell), self-consistent, DFT calculations (see the Methods section), we evaluate the value of ΔG_H on the 736 distinct binary transition-metal surface alloys that can be formed from the 16 metals Fe, Co, Ni, Cu, As, Ru, Rh, Pd, Ag, Cd, Sb, Re, Ir, Pt, Au and Bi (these elements are simply chosen to give a very broad pool of metallic and semimetallic elements, most of which are thermodynamically resistant to bulk oxide formation in water at 298 K and $U = 0$ V versus the standard hydrogen electrode; SHE). Such alloys, which are composed of a pure metal substrate with a solute element alloyed into the
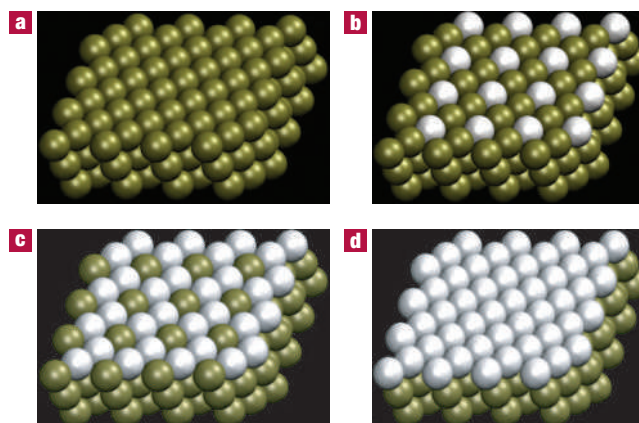
surface layer (Fig. 2), can exhibit surface properties that are vastly different from the properties of the bulk alloy. In Fig. 3, we show schematically the calculated free energies of hydrogen adsorption on a subset of these surface alloys—those with a 1/3 monolayer (ML) of solute in the surface layer (also see Fig. 2b). The figure clearly demonstrates that a number of binary surface alloys have high predicted activity for the HER.

Our purely computational screening procedure thus identifies a number of interesting candidates for HER catalysts. However, the analysis has so far neglected any consideration of whether or not the indicated alloys will be stable in real electrochemical environments. To estimate the stability of the surface alloys for the HER, we carry out four simple tests for each alloy (see the Supplementary Information). First, we estimate the free-energy change associated with surface segregation events; such events can cause surface solute atoms to segregate into the bulk. Second, we determine the free-energy change associated with intrasurface transformations such as island formation and surface de-alloying. Third, we evaluate the free energy of oxygen adsorption, beginning with splitting of liquid water; facile oxygen adsorption can lead to surface poisoning and/or oxide formation. Finally, we estimate the likelihood that the surface alloys of interest will corrode in acidic environments (pH = 0). For this test, we simply take the free energies of dissolution as reported in the electrochemical series[13].

In Fig. 4, we plot the most pessimistic of the free-energy transformation values determined for each alloy against the absolute magnitude of ΔG_H. The stability considerations immediately eliminate a large number of alloys from consideration; although many alloys have high predicted HER activity, only a small fraction are predicted to be both active and stable in acidic HER environments (Fig. 4), including, among others, surface alloys of BiPt, PtRu, AsPt, SbPt, BiRh, RhRe, PtRe, AsRu, IrRu, RhRu, IrRe and PtRh (note that the last seven of these have solute coverages different from 1/3 ML and therefore are not found in Fig. 3). Thus, these results demonstrate that stability considerations are essential for finding realistic candidate catalysts for hydrogen evolution. Furthermore, the results suggest that more detailed computational analyses and, ultimately, experimental testing of the promising alloys are in order.
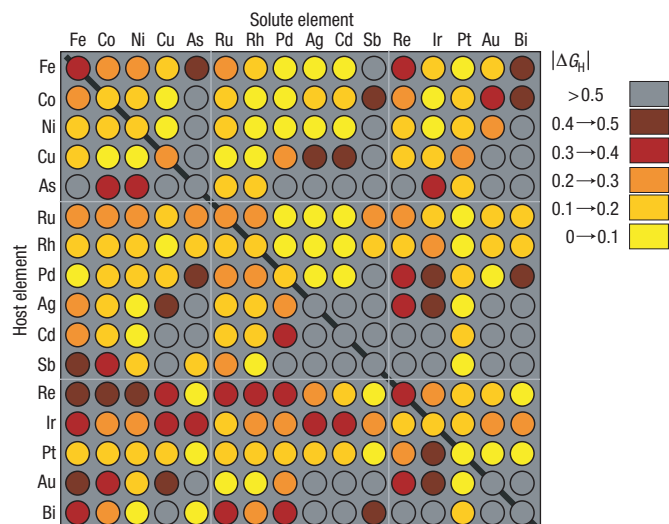
Figure 3 Computational high-throughput screening for $|\Delta G_H|$ on 256 pure metals and surface alloys. The rows indicate the identity of the pure metal substrates, and the columns indicate the identity of the solute embedded in the surface layer of the substrate. Thus, a point at the intersection of the 'Rh' row with the 'Pd' column, for example, would correspond to a surface alloy with Pd embedded in the (111) surface layer of a pure Rh host. The solute coverage is $1/3$ ML in all cases, and the adsorbed hydrogen coverage is also $1/3$ ML. The diagonal of the plot corresponds to the hydrogen-adsorption free-energy on the pure metals.
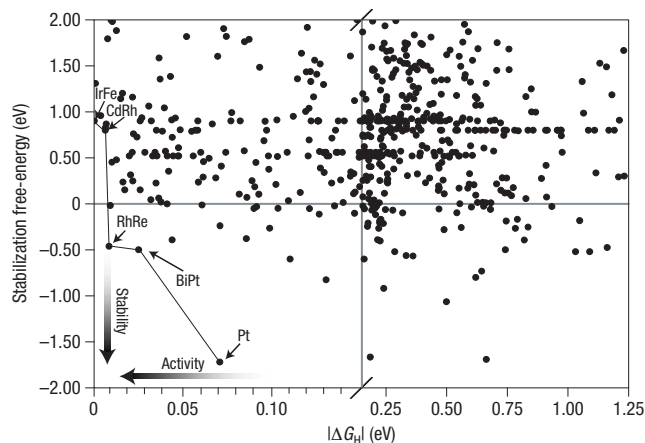

Figure 4 Pareto-optimal plot of stability and activity of surface alloys for the HER. The stabilization free-energy can be thought of as a free energy of formation for the surface alloys; the stability of the alloys with respect to various reconstructive/deactivating processes (including surface segregation, island formation, water splitting/oxygen adsorption and metal dissolution) is evaluated for each alloy, and the most pessimistic such energy (that is, the energy that would give the maximum probability that the alloy would destabilize) is plotted. The Pareto-optimal line indicates the best possible compromise between activity and stability, but given the simplicity of our model, other alloys could certainly be worth considering for use as HER catalysts; the alloys in the lower left quadrant, in particular, are promising. For the labelled points, a single element indicates a pure metal. For the bimetallic alloys, the solute is listed first; the solute coverages are $1/3$ ML (BiPt), 1 ML (RhRe), $1/3$ ML (CdRh) and $2/3$ ML (IrFe).

For the present study, we have selected BiPt for further analysis. This surface alloy is particularly interesting for the HER because of the stark contrast between its two constituent elements; pure Pt exhibits high catalytic activity, whereas pure Bi is not active at all (see Fig. 1). A surface alloy formed from these two elements, however, yields a material predicted by the calculations to have an activity comparable to, or even better than, pure Pt. We note, in passing, that this 'counterintuitive' surface alloy might not have been investigated without the aid of a combinatorial screening approach to guide the search for new catalysts.

To study this material in more detail, we first carried out further calculations on more detailed structural models to assess the effect of Bi coverage on our results. These calculations were done at a Bi coverage of $1/4$ ML (2×2 unit cells—see the Methods section); we note that Bi coverages equal to or greater than $1/2$ ML caused very large distortions of the alloy surface and, thus, were not considered in detail. The coverage of adsorbed hydrogen was also $1/4$ ML in these analyses. Although the preferred site preference for H on the BiPt surface alloy was different for the 2×2 versus $(\sqrt{3} \times \sqrt{3})R30°$ unit cells (face-centred cubic and near-top sites, respectively), the trends in ΔG_H values for the BiPt versus Pt slabs (-0.03 versus -0.07 eV on the $(\sqrt{3} \times \sqrt{3})R30°$ slab and 0.00 versus -0.04 eV on the 2×2 slab, respectively) were unchanged. For this more detailed analysis, we also carried out additional stability tests. We estimated the potential versus SHE at which hydroxyl will adsorb on the surface after water splitting; a value of ~ 0.4 V was obtained by following the procedure described previously[22]. Thus, although hydroxyl (which preferentially adsorbs on a Bi top site) adsorbs at a potential several tenths of a volt lower than atomic oxygen, even this more reactive species will not be present under typical HER conditions. We also evaluated the adatom formation energy for a BiPt surface alloy in the presence of $1/4$ ML of adsorbed hydrogen. Adatom formation was found to be endothermic (~ 0.07 eV) in the

presence of adsorbed hydrogen, suggesting that under typical HER conditions, the stable form is that of the surface alloy, and there will only be a relatively small concentration of Bi adatoms present at equilibrium. These results, when combined with the activity and stability calculations described above, paint a picture of BiPt surface alloys as structurally stable systems that exhibit moderately improved hydrogen evolution kinetics compared with pure Pt. It is important to emphasize, however, that the HER model used is quite simple and that the calculated difference in ΔG_H for BiPt and Pt (~ 0.04 eV) is small, given the typical accuracy associated with DFT calculations. Thus, it is only possible to conclude from the computational results that BiPt surface alloys might be interesting for the HER. To validate the results of our computational screening, careful experimental tests are clearly necessary.

Mixed Pt and Bi catalysts have been studied experimentally for decades. The two most commonly reported forms are: (1) a Pt surface modified by irreversibly adsorbed Bi (Pt–Bi_{ir}) and (2) bulk intermetallic PtBi or $PtBi_2$. Interest in bulk intermetallics has recently increased; they are typically investigated for electro-oxidation reactions (see, for example, ref. 23). Literature on the Pt–Bi_{ir} system—the most commonly studied form of mixed Pt and Bi—extends back to the 1970s; many studies focus on the oxidation of H_2, CO and formic acid, in addition to the reduction of O_2 (refs 24–33). Perhaps the most pertinent Pt–Bi_{ir} work is that of Gómez *et al.* who investigated the impact of Bi_{ir} on hydrogen evolution for Pt(100) and Pt(111). They showed that Bi_{ir} severely poisons both Pt surfaces for HER, as evidenced by a significant decrease in current as a function of Bi_{ir} coverage[26,27]. This result seems, at first glance, to contradict our theoretical prediction that mixed Pt and Bi alloys show improved activity for the HER. However, it should be recalled that our calculated BiPt
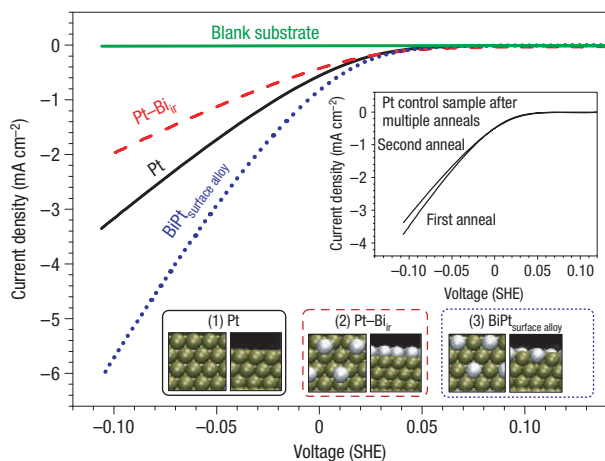
Figure 5 Hydrogen evolution after each stage of BiPt surface alloy synthesis on a fluorine-doped tin-oxide substrate. (1) Pt film after deposition and anneal (2) immediately after Bi UPD (3) after second anneal to form the BiPt surface alloy. The inset represents a control sample—Pt film without Bi—after first and second anneals. Current densities are normalized to the surface area of the initial, pure Pt sample, determined by H UPD.

surface structure is a surface alloy and not Bi_{ir} on Pt. By carefully controlling our electrochemical synthesis procedure (see discussion below), we create a surface alloy, and we show that this specific structure does, in fact, show improved activity for the HER. We note that, to our knowledge, no previous electrochemical studies on the Pt–Bi_{ir} system have attempted to form a surface alloy from the Bi_{ir} submonolayer.

To create the BiPt surface alloy, we used a three-step approach: (1) electrodeposition of an initial Pt film onto an inert support, (2) spontaneous deposition of a submonolayer of Bi_{ir} by Bi underpotential deposition (UPD) and (3) annealing of the Pt–Bi_{ir} precursor to form a BiPt surface alloy. For a given sample, we measured hydrogen evolution after each step of the synthesis. Following the work of Gómez *et al.*, we used the cathodic current density at 0.0 V versus SHE ($i_{0.0\,V}$) as the primary figure of merit for comparison—approximately the exchange current density[26,27,34]. Current–voltage measurements of a representative sample are plotted in Fig. 5. After heating the initial polycrystalline Pt film in a furnace (see the Methods section), the sample demonstrated a current density of $i_{0.0\,V} = 5.6(10)^{-4}\,A\,cm_{Pt}^{-2}$ ($-\log i_{0.0\,V} = 3.25$), consistent with previous literature values for Pt and indicating that the starting material was prepared adequately with negligible contamination[20]. We then adsorbed a submonolayer of Bi_{ir} onto the Pt film by the same Bi UPD method used in previous reports (10 min, 1 mM $Bi_2O_3/0.5\,M\,H_2SO_4$), resulting in an estimated Bi_{ir} coverage of ~10% by X-ray photoelectron spectroscopy (data not shown). Immediately after Bi UPD, the measured activity of the Pt–Bi_{ir} sample was considerably less than that of the initial Pt film— as expected, the Bi_{ir} blocked Pt sites and poisoned the surface for hydrogen evolution[24]. To complete the synthesis of a BiPt surface alloy, we annealed the Pt–Bi_{ir} precursor to 500 °C in a tube furnace.

Heating the Pt–Bi_{ir} system is the crucial step, as it provides the temperature necessary for Bi to overcome the kinetic barriers associated with alloying into the surface layer of Pt. Evidence of this process was reported by Paffett, Campbell and Taylor who conducted extensive studies of Bi dosed onto a Pt(111) crystal under ultrahigh vacuum conditions[35,36]. They used low-energy electron diffraction and Auger electron spectroscopy to

track morphological changes in a Bi adlayer as a function of coverage and temperature. One of the features they observed was that of a multilayered surface alloy—nominal composition $Pt_{1.00}Bi_{0.95}$—that formed at moderate temperatures (~370 °C) after starting with a multilayer Bi film. These surface-science experiments clearly indicate that Bi can and will form a surface alloy with Pt at elevated temperatures. The synthesis procedure that we have developed shows that surface alloys can also be produced from electrochemically adsorbed species; this is a simple, low-cost and general method that can be applied to numerous electrochemical systems.

Having completed the annealing procedure, we again measured the hydrogen evolution rate. Figure 5 shows significantly improved current–voltage characteristics; quantitatively speaking, $i_{0.0\,V}$ is double that of the Pt–Bi_{ir} precursor and, more importantly, ~50% greater than $i_{0.0\,V}$ of the initial Pt film. The improved performance of this film cannot be attributed to a simple change in morphology or to increased surface area because cyclic voltammetry in the H UPD region after each stage of synthesis indicates, if anything, a decrease in Pt surface area (see the Supplementary Information). To verify that the final anneal did not influence the Pt itself, we conducted several control experiments on similarly prepared pure Pt samples through multiple heat treatments. These data are shown as an inset in Fig. 5 and demonstrate a negligible effect.

The three-step procedure used to synthesize the annealed sample is highly reproducible, and the results provide strong evidence that the final, annealed sample is indeed a BiPt surface alloy, consistent with the ultrahigh vacuum studies of Paffett *et al.*[35,36]. It is worth noting that Bi itself is a notoriously poor electrocatalyst for the HER[17]; so it is difficult to imagine a morphology involving Bi—other than a surface alloy—that could possibly improve the electrocatalytic activity of Pt for hydrogen evolution. Hence, we have shown that a combination of *in silico* screening and careful experimental synthesis of promising candidates can lead to improved electrocatalysts, even when the identified metal combinations involve an element that is known to be inert for the HER, or when the metal combinations have previously been studied in different structural forms and have been found to be inactive.

We have thus confirmed experimentally the prediction that the HER activity of BiPt surface alloys should be comparable to that of pure Pt, or perhaps slightly better. This result suggests that our computational screening procedure is a promising technique for use in catalyst searches. The screening procedure can be viewed as a general, systematic, DFT-based method of incorporating both activity and stability criteria into the search for new metal alloy catalysts. As the accuracy and quality of kinetic models and DFT calculations improve, such *in silico* combinatorial screening procedures should become broadly useful for catalytic materials discovery.

METHODS

The computational analysis is carried out using DACAPO[37], a total energy calculation code. For the high-throughput computational screening, a three-layer slab, periodically repeated in a super-cell geometry with five equivalent layers of vacuum between any two successive metal slabs, is used to determine hydrogen binding energies. Close-packed surfaces are considered in all cases. A $(\sqrt{3} \times \sqrt{3})R30°$ unit cell, corresponding to a hydrogen coverage of 1/3 ML, is used. With this unit cell, and using the 16 elements described in the text, it is possible to create 736 symmetrically distinct pure metal and binary surface alloy slabs—16 pure metals, 240 surface alloys with a pure overlayer of solute metal, 240 with only two solute atoms in the surface layer and an extra 240 with one solute atom in the surface layer. For all slabs, the metal atoms are kept fixed in their bulk-truncated positions, and the hydrogen atoms are

allowed to relax until the total force is less than $0.5\,\text{eV}\,\text{Å}^{-1}$. The total energy is then further refined by using the residual forces and estimated harmonic vibrational frequencies for hydrogen ($\sim 1,050\,\text{cm}^{-1}$ for three-fold sites and $\sim 2,020\,\text{cm}^{-1}$ for top sites) to extrapolate to the bottom of a parabola in energy space. $0.24\,\text{eV}$ is added to the calculated binding energies (with respect to gaseous H_2) to give adsorption free energies[20]. The oxygen binding energies (used for the oxygen adsorption stability criterion) are computed in the same way, except that a slightly higher force cutoff ($0.6\,\text{eV}\,\text{Å}^{-1}$) is used and appropriate vibrational frequencies ($\sim 500\,\text{cm}^{-1}$ for three-fold sites and $\sim 775\,\text{cm}^{-1}$ for top sites) are used for the energy extrapolations.

For all DFT calculations, adsorption is allowed on only one of the two exposed surfaces of the metal slabs, and the electrostatic potential is adjusted accordingly[38]. Ionic cores are described by ultrasoft pseudopotentials[39], and the Kohn–Sham one-electron valence states are expanded in a basis of plane waves with kinetic energy below $340\,\text{eV}$; a density cutoff of $500\,\text{eV}$ is used. The surface Brillouin zone is sampled with an $18(\sqrt{3}\times\sqrt{3})$ Chadi–Cohen **k** point grid. In all cases, convergence of the total energy with respect to the cutoff energies and the **k** point set is confirmed. The exchange–correlation energy and potential are described by the generalized gradient approximation[37] (GGA-RPBE98). The self-consistent RPBE98 density is determined by iterative diagonalization of the Kohn–Sham hamiltonian, Fermi population of the Kohn–Sham states ($k_\text{B}T=0.1\,\text{eV}$) and Pulay mixing of the resulting electronic density[40]. All total energies have been extrapolated to $k_\text{B}T=0\,\text{eV}$. Zero-point energy effects are assumed to be approximately constant for all metals and alloys considered[20]. Spin-polarization effects are included in the reported results for alloys in which naturally magnetized metals (Ni, Co, Fe) are present. Graphical inserts are produced using visual molecular dynamics[41].

For the more detailed calculations on the BiPt surface alloy, a 2×2 surface unit cell is used, corresponding to a hydrogen coverage of $1/4$ ML. A four-layer slab is used for these calculations, and the top two layers of the slab are allowed to relax. The maximum force permitted for any vector component is $0.05\,\text{eV}\,\text{Å}^{-1}$. The **k** point grid, in this case, involves $18(1\times 1)$ Chadi–Cohen points.

Pt was electrodeposited from a $1\,\text{mM}\,H_2PtCl_6$ (99.995%, Aldrich) solution onto an inert substrate—fluorine-doped tin-oxide coated onto glass (Hartford Glass). A square wave pulsed deposition was used, referenced to a Ag quasi-reference electrode (AgQRE). The three-step deposition sequence consisted of a $0.5\,\text{s}$ pulse at $-0.9\,\text{V}$ versus AgQRE, followed by a $0.5\,\text{s}$ pulse at $-0.2\,\text{V}$ versus AgQRE, followed by a $1\,\text{s}$ rest interval. The sequence was repeated 120 times, totalling 4 min. The AgQRE was produced by oxidizing a pre-cleaned Ag wire in $1.0\,\text{M}$ HCl at $+1.0\,\text{V}$ versus the saturated calomel electrode for 60 s. Cyclic voltammograms of the deposited and annealed Pt films showed no evidence of contamination, corroborated by X-ray photoelectron spectroscopy measurements. Hydrogen evolution experiments were conducted in N_2-purged H_2SO_4 (pH 0.40). The cyclic voltammogram sweep rate was $5\,\text{mV}\,\text{s}^{-1}$ versus the saturated calomel electrode. A bridge was used during recording of the cyclic voltammograms to prevent Cl^- contamination. All heat treatments were conducted in a tube furnace at $500\,^\circ\text{C}$ in air for 12 h. Samples were transferred in ambient air and protected in plastic containers.

References

1. Greeley, J. & Mavrikakis, M. Alloy catalysts designed from first principles. *Nature Mater.* **3,** 810–815 (2004).
2. Muller, R. P., Philipp, D. M. & Goddard, W. A. Quantum mechanical-rapid prototyping applied to methane activation. *Top. Catalys.* **23,** 81–98 (2003).
3. Andersson, M. P. *et al.* Towards computational screening in heterogeneous catalysis: Pareto-optimal methanation catalysts. *J. Catalys.* **239,** 501–506 (2006).
4. Greeley, J., Nørskov, J. K. & Mavrikakis, M. Electronic structure and catalysis on metal surfaces. *Annu. Rev. Phys. Chem.* **53,** 319–348 (2002).
5. Toulhoat, H. & Raybaud, P. Kinetic interpretation of catalytic activity patterns based on theoretical chemical descriptors. *J. Catalys.* **216,** 63–72 (2003).
6. Linic, S., Jankowiak, J. & Barteau, M. A. Selectivity driven design of bimetallic ethylene epoxidation catalysts from first principles. *J. Catalys.* **224,** 489–493 (2004).
7. Ceder, G. *et al.* Identification of cathode materials for lithium batteries guided by first-principles calculations. *Nature* **392,** 694–696 (1998).
8. Besenbacher, F. *et al.* Design of a surface alloy catalyst for steam reforming. *Science* **279,** 1913–1915 (1998).
9. Franceschetti, A. & Zunger, A. The inverse hand-structure problem of finding an atomic configuration with given electronic properties. *Nature* **402,** 60–63 (1999).
10. Vitos, L., Korzhavyi, P. A. & Johansson, B. Stainless steel optimization from quantum mechanical calculations. *Nature Mater.* **2,** 25–28 (2003).
11. Jacobson, M. Z., Colella, W. G. & Golden, D. M. Cleaning the air and improving health with hydrogen fuel-cell vehicles. *Science* **308,** 1901–1905 (2005).
12. Hamann, C. H., Hamnett, A. & Vielstich, W. *Electrochemistry* (Wiley-VCH, Weinheim, 1998).
13. Lide, D. R. (ed.) *CRC Handbook of Chemistry and Physics* (CRC Press, New York, 1996).
14. Conway, B. E. & Bockris, J. O. M. Electrolytic hydrogen evolution kinetics and its relation to the electronic and adsorptive properties of the metal. *J. Chem. Phys.* **26,** 532–541 (1957).
15. Parsons, R. The rate of electrolytic hydrogen evolution and the heat of adsorption of hydrogen. *Trans. Faraday Soc.* **54,** 1053–1063 (1958).
16. Gerischer, H. Mechanism of electrolytic discharge of hydrogen and adsorption energy of atomic hydrogen. *Bull. Soc. Chim. Belg.* **67,** 506 (1958).
17. Trasatti, S. Work function, electronegativity, and electrochemical behaviour of metals. III. Electrolytic hydrogen evolution in acid solutions. *Electroanal. Chem. Interfacial Electrochem.* **39,** 163–184 (1972).
18. Krishtalik, L. I. On the influence of hydrogenation of the cathode metal upon the overvoltage of hydrogen. *Electrokhimiya* **2,** 616 (1966).
19. Sabatier, P. Hydrogénations et deshydrogénations par catalyse. *Ber. Deutschen Chem. Gesellschaft* **44,** 1984 (1911).
20. Nørskov, J. K. *et al.* Trends in the exchange current for hydrogen evolution. *J. Electrochem. Soc.* **152,** J23–J26 (2005).
21. Greeley, J., Kibler, L., El-Aziz, A. M., Kolb, D. M. & Nørskov, J. K. Hydrogen evolution over bimetallic systems: Understanding the trends. *ChemPhysChem* **7,** 1032–1035 (2006).
22. Nørskov, J. K. *et al.* Origin of the overpotential for oxygen reduction at a fuel-cell cathode. *J. Phys. Chem. B* **108,** 17886–17892 (2004).
23. Casado-Rivera, E. *et al.* Electrocatalytic activity of ordered intermetallic phases for fuel cell applications. *J. Am. Chem. Soc.* **126,** 4043–4049 (2004).
24. Markovic, N. M. & Ross, P. N. Surface science studies of model fuel cell electrocatalysts. *Surf. Sci. Rep.* **45,** 121–229 (2002).
25. Schmidt, T. J., Stamenkovic, V. R., Lucas, C. A., Markovic, N. M. & Ross, P. N. Surface processes and electrocatalysts on the Pt(hkl)/Bi-solution interface. *Phys. Chem. Chem. Phys.* **3,** 3879–3890 (2001).
26. Gómez, R., Fernández-Vega, A., Feliu, J. M. & Aldaz, A. Hydrogen evolution on Pt single-crystal surfaces—effects of irreversibly adsorbed bismuth and antimony on hydrogen adsorption and evolution on Pt(100). *J. Phys. Chem.* **97,** 4769–4776 (1993).
27. Gómez, R., Feliu, J. M. & Aldaz, A. Effects of irreversibly adsorbed bismuth on hydrogen adsorption and evolution on Pt(111). *Electrochim. Acta* **42,** 1675–1683 (1997).
28. Bowles, B. J. Formation and desorption of monolayers of bismuth on a platinum electrode. *Electrochim. Acta* **15,** 737 (1970).
29. Clavilier, J., Feliu, J. M. & Aldaz, A. An irreversible structure sensitive adsorption step in bismuth underpotential deposition at platinum-electrodes. *J. Electroanal. Chem.* **243,** 419–433 (1988).
30. Hayden, B. E., Murray, A. J., Parsons, R. & Pegg, D. J. UHV and electrochemical transfer studies on Pt(110)-(1x2): The influence of bismuth on hydrogen and oxygen adsorption, and the electro-oxidation of carbon monoxide. *J. Electroanal. Chem.* **409,** 51–63 (1996).
31. Evans, R. W. & Attard, G. A. The redox behavior of compressed bismuth overlayers irreversibly adsorbed on Pt(111). *J. Electroanal. Chem.* **345,** 337–350 (1993).
32. Hamm, U. W., Kramer, D., Zhai, R. S. & Kolb, D. M. On the valence state of bismuth adsorbed on a Pt(111) electrode: an electrochemistry, LEED, and XPS study. *Electrochim. Acta* **43,** 2969–2978 (1998).
33. Kizhakevariam, N. & Stuve, E. M. Coadsorption of bismuth with electrocatalytic molecules—a study of formic-acid oxidation on Pt(100). *J. Vac. Sci. Technol. A* **8,** 2557–2562 (1990).
34. Vetter, K. J. *Electrochemical Kinetics: Theoretical and Experimental Aspects* (Academic, New York, 1967).
35. Paffett, M. T., Campbell, C. T. & Taylor, T. N. The influence of adsorbed Bi on the chemisorption properties of Pt(111)—H_2, CO, and O_2. *J. Vac. Sci. Technol. A* **3,** 812–816 (1985).
36. Paffett, M. T., Campbell, C. T. & Taylor, T. N. Adsorption and growth modes of Bi on Pt(111). *J. Chem. Phys.* **85,** 6176–6185 (1986).
37. Hammer, B., Hansen, L. B. & Nørskov, J. K. Improved adsorption energetics within density-functional theory using revised Perdew-Burke-Ernzerhof functionals. *Phys. Rev. B* **59,** 7413–7421 (1999).
38. Bengtsson, L. Dipole correction for surface supercell calculations. *Phys. Rev. B* **59,** 12301–12304 (1999).
39. Vanderbilt, D. Soft self-consistent pseudopotentials in a generalized eigenvalue formalism. *Phys. Rev. B* **41,** 7892–7895 (1990).
40. Kresse, G. & Furthmuller, J. Efficiency of ab-initio total energy calculations for metals and semiconductors using a plane-wave basis set. *Comput. Mater. Sci.* **6,** 15–50 (1996).
41. Humphrey, W., Dalke, A. & Schulten, K. VMD—visual molecular dynamics. *J. Mol. Graph.* **14,** 33–38 (1996).

Competing financial interests

The authors declare that they have no competing financial interests.

Included Publications

Paper 3:

“Identification of Active Edge Sites for Electrochemical H_2 Evolution from MoS$_2$ Nanocatalysts”
T. F. Jaramillo, K. P. Jørgensen, <u>J. Bonde</u>, J. H. Nielsen, S. Horch and I. Chorkendorff,
Science, **316**, 100 (2007)

Included Publications

Identification of Active Edge Sites for Electrochemical H$_2$ Evolution from MoS$_2$ Nanocatalysts

Thomas F. Jaramillo,[1] Kristina P. Jørgensen,[1] Jacob Bonde,[1] Jane H. Nielsen,[1] Sebastian Horch,[2] Ib Chorkendorff[1]*

The identification of the active sites in heterogeneous catalysis requires a combination of surface sensitive methods and reactivity studies. We determined the active site for hydrogen evolution, a reaction catalyzed by precious metals, on nanoparticulate molybdenum disulfide (MoS$_2$) by atomically resolving the surface of this catalyst before measuring electrochemical activity in solution. By preparing MoS$_2$ nanoparticles of different sizes, we systematically varied the distribution of surface sites on MoS$_2$ nanoparticles on Au(111), which we quantified with scanning tunneling microscopy. Electrocatalytic activity measurements for hydrogen evolution correlate linearly with the number of edge sites on the MoS$_2$ catalyst.

Progress in the field of heterogeneous catalysis is often hampered by the difficulty of identifying the active site on a catalyst surface (*1*, *2*). In homogeneous catalysis, the active center is generally more clearly defined and quantified, with spectroscopic and mechanistic studies providing direct insight into reactive intermediates. Solid-state catalysts, however, commonly exhibit a variety of different surface sites that are difficult to identify and quantify; the scenario is further complicated when multiple sites work together in turning over a reaction. Identifying the most active site(s) is critical to designing and developing improved catalytic materials. Many useful in situ and ex situ experimental techniques, as well as computational methods, have been developed (*3–5*) to address this problem, but identifying the active site remains a challenging task.

In this study we used such methods to determine the active site of nanoparticulate MoS$_2$ for the hydrogen evolution reaction (HER), $2H^+ + 2e^- \rightarrow H_2$ (*6*, *7*), which is fundamentally important for a variety of electrochemical processes, fuel cells (as the reverse reaction), and solar H$_2$ production (water splitting), particularly where there is a need to replace precious metal catalysts such as Pt (*7*, *8*). In its bulk form, MoS$_2$ is a poor HER catalyst (*9*). Nanoparticulate MoS$_2$, however, is a more promising system; density functional theory (DFT) calculations indicate that the edges of MoS$_2$ nanoparticles are active for hydrogen evolution (*8*), but no previous experiments have shown this conclusively.

Nanoparticulate MoS$_2$ has been studied previously in an attempt to link activity to specific surface sites, in that MoS$_2$ is used industrially as a hydrodesulfurization (HDS) catalyst (*10*, *11*). Detailed insight has been gained from studies on simplified model systems in ultra-high vacuum (UHV) and by using computational methods (*12–15*), as well as from combining reactivity measurements and ex situ characterization of industrial catalyst samples (*10*, *11*, *16*). Structural studies on the MoS$_2$ catalyst have shown that it is composed almost entirely of flat polygons of S-Mo-S trilayers (*10*); depending on the synthesis conditions, these trilayers may stack in a graphite-like manner or remain as single trilayers. For single trilayers, two general kinds of surface sites exist—terrace sites, which are those on the basal plane, and edge sites, which lie at the edge of the nanoparticles. DFT studies suggest that the active site for HDS is on the edge of the MoS$_2$ nanoparticles. This result is supported by adsorption studies of thiophene using scanning tunneling microscopy (STM) (*17*). Despite numerous studies on this material, there is a call for studies that uniquely link the well-defined structures of the model sys-

tem to catalytic activity under standard reaction conditions (*18*).

To provide an experimental elucidation of the active site for the HER, we prepared MoS$_2$ samples in UHV of deliberately chosen nanoparticulate morphologies such that the fractions of the terrace and edge sites were systematically varied, then characterized by STM. All of the MoS$_2$ samples in this study were synthesized on a clean Au(111) substrate by physical vapor deposition of Mo in a background of H$_2$S (*19*), followed by annealing, according to the approach in (*13*). Three samples were annealed at 400°C, two were annealed at 550°C, and a "blank" sample was synthesized without the deposition of Mo and annealed to 400°C. The Au(111) substrate serves to disperse the MoS$_2$ nanoparticles by its herringbone reconstruction and is not particularly active for the HER (*20*). To maintain discretely separated single trilayer particles, we purposely synthesized the samples with low area coverages of MoS$_2$, less than one-fourth ML (i.e., 0.25 nm$^2_{MoS2}$/nm$^2_{geometric}$).

Immediately after deposition, each sample was vacuum transferred to a second UHV chamber for STM imaging (Fig. 1). The crystallized, single-layered MoS$_2$ nanoparticles can be described as flat polygons with a conducting edge state, seen as bright lines along the particle perimeter. Comparison of representative images of samples annealed at 400°C (Fig. 1A) and 550°C (Fig. 1B) shows how particle size increased after sintering at the higher temperature. The particles annealed to 400°C are consistent with similarly prepared MoS$_2$ nanoparticles on Au(111) (*13*). Besenbacher *et al.* have shown that the dominant edge structure of MoS$_2$ nanoparticles is that of a sulfided Mo edge and that this edge is particularly favored by larger-sized particles (*12*, *18*). We also observe the predominance of the sulfided Mo-edge in our samples, regardless of annealing temperature. Thus, controlled sintering allows us to change the ratio of basal plane sites to edge sites without changing the nature of the edge. This sulfided (1 0 –1 0)
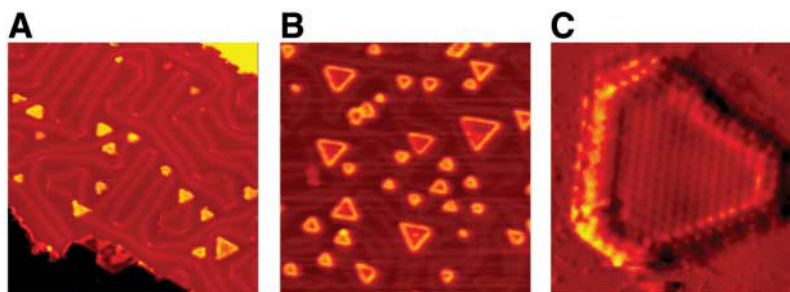

Fig. 1. A series of STM images of MoS$_2$ nanoparticles on Au(111). The particles exhibit the typical polygon morphology with conducting edge states and are dispersed on the Au surface irrespective of coverage and annealing temperature (400°C or 550°C). (**A**) Low coverage (0.06 nm$^2_{MoS2}$/nm$^2_{geom.}$), annealed to 400°C (470 Å by 470 Å, 1.2 nA, 4 mV). (**B**) High coverage (0.23 nm$^2_{MoS2}$/nm$^2_{geom.}$), annealed to 550°C (470 Å by 470 Å, 1.2 nA, 1.9 V). (**C**) Atomically resolved MoS$_2$ particle, from a sample annealed to 550°C, showing the predominance of the sulfided Mo-edge (*19*, *20*) (60 Å by 60 Å, 1.0 nA, 300 mV).

[1]Center for Individual Nanoparticle Functionality, Department of Physics, Nano-DTU, Technical University of Denmark, DK-2800 Lyngby, Denmark. [2]Center for Atomic-scale Materials Design, Department of Physics, Nano-DTU, Technical University of Denmark, DK-2800 Lyngby, Denmark.

*To whom correspondence should be addressed. E-mail: ibchork@fysik.dtu.dk

Mo-edge is the same structure predicted by DFT calculations to be the active site for H_2 evolution (8).

After imaging, we transfer the samples from UHV into an electrochemical cell to measure HER activity (21). Polarization curves ($i - E$) within a cathodic potential window, and corresponding Tafel plots (log $i - E$), are shown in Fig. 2. Current densities are normalized to the geometric area of the exposed face of all samples.

The most inherent measure of activity for the HER is the exchange current density, i_0 (6, 7, 22, 23), which is determined by fitting $i - E$ data to the Tafel equation (6), yielding Tafel slopes of 55 to 60 mV/decade and exchange current densities in the range of 1.3×10^{-7} to 3.1×10^{-7} A/cm$^2_{geometric}$ for all MoS$_2$ samples (table S1). In Fig. 3, we plot the exchange current density for each sample versus two sample parameters, the MoS$_2$ area coverage (Fig. 3A), and the MoS$_2$ edge state length (Fig. 3B). The data points fall on a straight line only when plotted versus edge length. Although the points show some scatter around this trend, they are described by a best-fit linear relation with a slope of 1.67×10^{-20} A/nm$_{MoS2-edge}$.

Because the rate of reaction is directly proportional to the number of edge sites for all samples, regardless of particle size, we conclude that the edge site is indeed the active site (24). Bearing this in mind, we note in Fig. 3A that the exchange current densities of the samples sintered at 550°C are significantly lower than those prepared at 400°C, per MoS$_2$ coverage, exactly as one would expect considering that the sintered samples have less edge length per area of MoS$_2$.

We also compared nanoscale MoS$_2$ to other materials that catalyze the HER on a per active site basis (1). For this direct site-to-site comparison, we used the 1.5×10^{15} sites/cm^2 for the Pt(111) face as the basis for comparison as Pt is the archetypal HER catalyst (25). An exchange current density of 4.5×10^{-4} A/cm^2 for this face (26) yields a turnover frequency (TOF) of 0.9 s^{-1} (table S2). In general, TOFs of transition metals range over 10 orders of magnitude (Hg, for instance, has a TOF as low as ~10^{-9} s^{-1}) (22). Given the slope in Fig. 3B, we have calculated the TOF of the MoS$_2$ edge to be 0.02 s^{-1}, indeed in the high range of TOFs for metals.

For further insight into the catalytic nature of the MoS$_2$ edge, we have added our data for nanoparticulate MoS$_2$ to a recent version of the volcano-type relations observed for HER catalysts (Fig. 4), in this case for the Gibbs free energy for atomic hydrogen adsorption (ΔG_H) (22, 23). These volcano relations ultimately reflect the Sabatier principle, which accounts for optimal surfaces as ones that exhibit moderate binding energies of reaction intermediates, hydrogen adsorption in the case of the HER. In Fig. 4, the exchange current density is shown as a function of the DFT-calculated free energy of adsorption of hydrogen, which was recently determined to be +0.08 eV for the MoS$_2$ edge (8). To add MoS$_2$ to this figure, we converted the TOF of nanoparticulate MoS$_2$ to its exchange current density per 1.5×10^{15} sites/cm^2, which yields 7.9×10^{-6} A/cm^2 (table S2). This value surpasses those of the common metals and lies just below those of the precious Pt-group metals. When plotting this experimentally determined activity of the edge site versus its DFT-calculated ΔG_H (8), we see that it follows the volcano trend (23). This agreement validates the predictive capability of this DFT model as well as its applicability beyond metal catalysts.

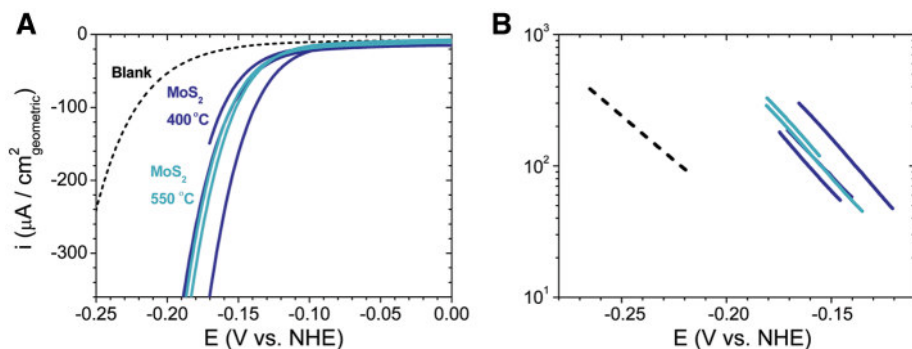After identifying the active site and comparing it with typical metal catalysts, we may

Fig. 2. Polarization curves and Tafel plots in a cathodic potential window for the five different MoS$_2$ samples as well as a blank sample. Samples annealed to 400°C are dark blue, samples annealed to 550°C light blue. (**A**) Polarization curve showing H$_2$ evolution on all samples. (**B**) Tafel plot (log current versus potential). All of the MoS$_2$ samples have Tafel slopes of 55 to 60 mV per decade irrespective of annealing temperature and coverage. Sweep rate: 5 mV/s.
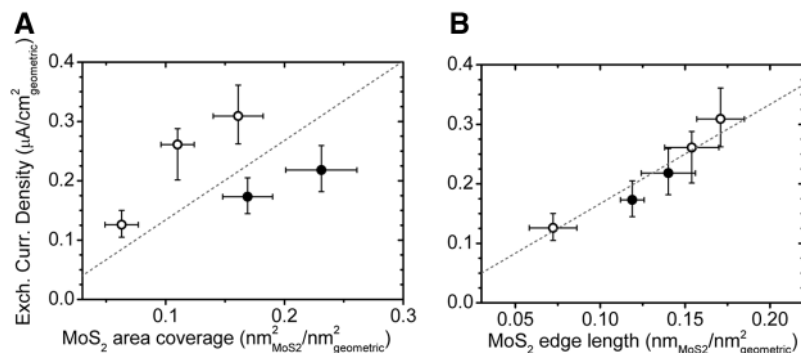

Fig. 3. Exchange current density versus (**A**) MoS$_2$ area coverage and (**B**) MoS$_2$ edge length. In both figures, open circles are samples annealed to 400°C, filled circles are samples annealed to 550°C. The exchange current density does not correlate with the area coverage of MoS$_2$, whereas it shows a linear dependence on the MoS$_2$ edge length. Exchange current densities are extracted from the Tafel plot in Fig. 2. The edge length was measured on all imaged particles and normalized by the imaged area.

Fig. 4. Volcano plot of the exchange current density as a function of the DFT-calculated Gibbs free energy of adsorbed atomic hydrogen for nanoparticulate MoS$_2$ and the pure metals (23). As seen, MoS$_2$ follows the same trend as the pure metals. The MoS$_2$ exchange current density is normalized to the atomic site density of Pt for comparison. Samples are polycrystalline unless otherwise noted.
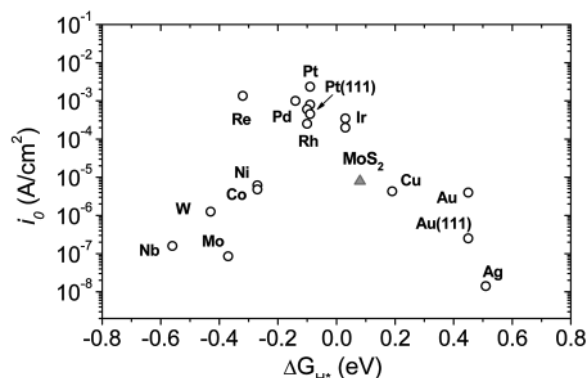
consider how to improve its activity. The DFT-calculated ΔG_H of the MoS_2 edge site is slightly positive at +0.08 eV, with calculations suggesting an H coverage of only one-quarter on the edge under operating conditions (8). Thus, only 1 in 4 edge atoms evolves molecular H_2 at a given time, unlike Pt(111) which operates at a H-coverage of ~1 ML (7, 26, 27). If all MoS_2 edge sites could be made to adsorb H, activity could be increased by a factor of 4. This might be accomplished by appropriately tuning the electronic structure of the edge to increase the bond strength of the ad-sorbed H (23). Such a modification could simul-taneously improve the inherent turnover of each edge site, further improving the overall activity of the material toward that of Pt-group metals.

References and Notes

1. G. A. Somorjai, *Introduction to Surface Chemistry and Catalysis* (Wiley, New York, 1994).
2. T. Zambelli, J. Wintterlin, J. Trost, G. Ertl, *Science* **273**, 1688 (1996).
3. C. T. Campbell, *Science* **294**, 1471 (2001).
4. N. I. Jaeger, *Science* **293**, 1601 (2001).
5. S. Dahl *et al.*, *Phys. Rev. Lett.* **83**, 1814 (1999).
6. J. O. M. Bockris, S. U. M. Khan, *Surface Electrochemistry: A Molecular Level Approach.* (Plenum, New York, 1993).
7. B. E. Conway, B. V. Tilak, *Electrochim. Acta* **47**, 3571 (2002).
8. B. Hinnemann *et al.*, *J. Am. Chem. Soc.* **127**, 5308 (2005).
9. W. Jaegermann, H. Tributsch, *Prog. Surf. Sci.* **29**, 1 (1988).
10. H. Topsøe, B. S. Clausen, F. E. Massoth, in *Catalysis Science and Technology*, J. R. Anderson, M. Boudart, Eds. (Springer-Verlag, New York, 1996), vol. 11.
11. R. R. Chianelli *et al.*, *Catal. Rev.* **48**, 1 (2006).
12. M. V. Bollinger *et al.*, *Phys. Rev. Lett.* **87**, 19 (2001).
13. S. Helveg *et al.*, *Phys. Rev. Lett.* **84**, 951 (2000).
14. J. Kibsgaard *et al.*, *J. Am. Chem. Soc.* **128**, 13950 (2006).
15. M. V. Bollinger, K. W. Jacobsen, J. K. Nørskov, *Phys. Rev. B* **67**, 085410 (2003).
16. R. Prins, V. H. J. de Beer, G. A. Somorjai, *Catal. Rev. Sci. Eng* **31**, 1 (1989).
17. J. V. Lauritsen *et al.*, *J. Catal.* **224**, 94 (2004).
18. J. V. Lauritsen *et al.*, *Nat. Nanotech.* **2**, 53 (2007).
19. Materials and methods are available as supporting material on *Science* Online.
20. J. Perez, E. R. Gonzalez, H. M. Villullas, *J. Phys. Chem. B* **102**, 10931 (1998).
21. The cell, specifically designed for studies on UHV-transferred samples, is sealed upon the imaged (111) face of the sample with a viton o-ring, exposing ~0.10 cm^2 to the H_2SO_4 electrolyte (pH 0.24, 23°C), and cyclic voltammograms are recorded. This procedure ensures a one-to-one correlation between the imaged MoS_2 nanoparticles and the measured activity for hydrogen evolution.
22. S. Trasatti, *J. Electroanal. Chem.* **39**, 163 (1972).
23. J. K. Nørskov *et al.*, *J. Electrochem. Soc.* **152**, J23 (2005).
24. We note that Au atoms along the particle edge also scale with the edge length; however, previous experimental and computational studies have shown negligible interaction between the MoS_2 and the support (14, 15), leading us to conclude that such sites would be as inactive as those of the blank samples, prepared without MoS_2 deposition.
25. In our comparison with Pt(111), we assumed that the observed HER on this surface is dominated by terrace atoms, not defects. This is the consensus in the literature (7).
26. N. M. Markovic, B. N. Grgur, P. N. Ross, *J. Phys. Chem. B* **101**, 5405 (1997).
27. E. Skúlason *et al.*, *Phys. Chem. Chem. Phys.* **9**, 3241 (2007).; 10.1039/B700099E
28. This project was supported by the Danish Strategic Research Council. T.F.J. acknowledges an H. C. Ørsted Postdoctoral Fellowship from the Technical University of Denmark. The Center for Individual Nanoparticle Functionality is supported by the Danish National Research Foundation. The Center for Atomic-scale Materials Design is supported by the Lundbeck Foundation.

Understanding Reactivity at Very Low Temperatures: The Reactions of Oxygen Atoms with Alkenes

Hassan Sabbah,[1] Ludovic Biennier,[1] Ian R. Sims,[1]* Yuri Georgievskii,[2] Stephen J. Klippenstein,[3]* Ian W. M. Smith[4]*

A remarkable number of reactions between neutral free radicals and neutral molecules have been shown to remain rapid down to temperatures as low as 20 kelvin. The rate coefficients generally increase as the temperature is lowered. We examined the reasons for this temperature dependence through a combined experimental and theoretical study of the reactions of $O(^3P)$ atoms with a range of alkenes. The factors that control the rate coefficients were shown to be rather subtle, but excellent agreement was obtained between the experimental results and microcanonical transition state theory calculations based on ab initio representations of the potential energy surfaces describing the interaction between the reactants.

A pplication of the CRESU technique (1) has shown that a surprising number of bimolecular reactions between neutral gas-phase species are rapid at very low temperatures. To date, rate coefficients for some 45 neutral-neutral reactions have been measured (2, 3), in some cases at temperatures as low as 13 K (4). All have rate coefficients at 298 K [*k*(298 K)] that are equal to or exceed ~10^{-11} cm^3 molecule^{-1} s^{-1}. Moreover, the general trend with temperature is for the rate coefficients to increase as the temperature is lowered.

These observations have led to a reevaluation of the chemistry that occurs in the cold cores (10 to 20 K) of dense, dark interstellar clouds (ISCs), where the majority of interstellar molecules have been identified. Although sequences of ion-molecule reactions initiated by the cosmic ray–induced ionization of H_2 clearly play a central role in this chemistry, neutral-neutral reactions are now expected to be more important than previously thought (5). Unfortunately, the kinetic database required for detailed astrochemical modeling (6) is still far from complete. There are many reactions that may occur in ISCs, such as those between pairs of unstable species, for which low-temperature kinetic data neither exist nor are likely to be obtained in the foreseeable future. Theoretical or semi-empirical methods of estimating these rate coefficients are therefore desirable.

Several complementary theoretical treatments (7–9) have been advanced to explain the observed negative temperature dependences of rate coefficients for radical-radical reactions, principally on the basis of the notion of adiabatic capture of the reactants via long-range attractive forces. Although they differ in their details, these treatments all predict large rate coefficients at very low temperatures for radical-radical reactions, where there is generally no barrier on the minimum energy reaction path. In the case of radical-molecule reactions, a key issue is whether a potential energy barrier exists along the mini-mum energy path from reactants to products: either a real barrier (i.e., a maximum above the energy of the separated reactants) or a "submerged" barrier corresponding to a maximum along the minimum energy path between the shallow min-imum associated with a prereaction complex and the products (see below). Further theoret-ical work, particularly by Georgievskii and Klippenstein (10, 11), has shown that a sub-merged barrier can serve as a second inner tran-sition state (or bottleneck), because the internal states at this smaller interreactant separation are more widely spaced than at the outer, capture transition state. In these circumstances, the rate of reaction falls below that predicted by capture theories, and a version of microcanonical transi-

[1]Institut de Physique de Rennes, Laboratoire PALMS, UMR 6627 du CNRS–Université de Rennes 1, Equipe Astrochimie Expérimentale, Bat. 11c, Campus de Beaulieu, 35042 Rennes Cedex, France. [2]Combustion Research Facility, Sandia National Laboratories, Livermore, CA 94551, USA. [3]Chemistry Division, Argonne National Laboratory, Argonne, IL 60439, USA. [4]University Chemical Laboratory, Lensfield Road, Cambridge CB2 1EW, UK.

*To whom correspondence should be addressed. E-mail: ian.sims@univ-rennes1.fr (I.R.S.); sjk@anl.gov (S.J.K.); i.w.m. smith@bham.ac.uk (I.W.M.S.)

Included Publications

Paper 4:

Hydrogen Evolution on Nano-particulate Transition Metal Sulfides

**Jacob Bonde[a], Poul G. Moses[b] , Thomas F. Jaramillo[c],
Jens K. Nørskov[b], Ib Chorkendorff [*a]**

The Hydrogen Evolution Reaction (HER) on carbon supported MoS_2 nanoparticles is investigated and compared to findings with previously published work on Au(111) supported MoS_2. An investigation into MoS_2 oxidation is presented and used to quantify the surface concentration of
10 MoS_2. Other metal sulfides with morphologies similar to MoS_2 such as WS_2, cobalt-promoted WS_2, and cobalt-promoted MoS_2 were also investigated in the search for improved HER activity. Experimental findings are compared to Density Functional Theory (DFT) calculated values for the hydrogen binding energies (ΔG_H) on each system.

Introduction

15

Research efforts to develop electrocatalysts for energy conversion reactions have increased substantially in recent years. Platinum, the ubiquitous electrocatalyst used in PEM fuel cells, is both expensive and scarce, prompting widespread
20 efforts to discover cost-effective materials to replace Pt. In this work we focus on non-noble metal sulfide catalysts for the Hydrogen Evolution Reaction (HER) under acidic conditions, a reaction catalyzed most effectively by Pt-based materials[1] .

25

Previously, MoS_2 has been studied as a catalyst in hydrodesulfurisation[2] and in the photo-oxidation of organics[3,4]. In electrocatalysis, it has recently been shown that the edge structure of nanoparticulate MoS_2 is active for the
30 HER, mimicking the active sites/co-factor of the hydrogen evolving enzymes nitrogenase and hydrogenase[5,6]. This work aims to extend the investigation on carbon-supported nanoparticulate MoS_2 for the HER. Unlike the case of Au(111) supported MoS_2 studied by STM in previous work[6],
35 the catalysts probed herein are more commercially relevant, which also implies that they are less homogeneous and more difficult to image on the atomic scale. As knowledge of the concentration of active sites on a catalyst surface is paramount to elucidating structure-composition-activity relationships, the
40 first aim of this work is to utilize electrochemical oxidation to probe MoS_2 surface area, distinguishing between basal plane and edge sites. In developing this methodology to quantify active sites on a macroscopic scale, we then direct our attention to related catalyst systems, namely WS_2, cobalt-
45 promoted WS_2, and cobalt-promoted MoS_2. We end by comparing experimentally determined activity data to predictions made by Density Functional Theory (DFT) models of these systems in order to gain insight into trends in catalyst activity.

50

It has been found that ΔG_H, the hydrogen binding energy to a given surface, is a good descriptor for identifying
55 electrocatalyst materials with high exchange current densities[1,7,8]. A recent study[5]using DFT showed that the active sites on nitrogenase and hydrogenase bind hydrogen weakly, similar to Pt. It was also found that the overpotential of carbon supported MoS_2 is comparable to the DFT calculated
60 hydrogen binding energy on the edge of the nanoparticles. In another study MoS_2 nanoparticles on Au(111) were synthesized under UHV conditions, characterized by STM and examined for HER activity[6].This study showed direct evidence that the active site of the MoS_2 nanoparticles is
65 indeed the edge. The exchange current density was also found to be in agreement with the volcano relation between the HER exchange current density and the DFT calculated values for ΔG_H proposed by Nørskov et al[7]. By having identified the active site of MoS_2 particles, the next step is to modify that
70 edge such that its ΔG_H approaches even closer to zero where the HER volcano curve has its maximum, and this is a major aim of the work presented herein.

Bulk MoS_2 consists of stacked S-Mo-S layers, and MoS_2
75 nanoparticles can be synthesized as single layer hexagonal structures exposing two different kinds of edges, the so-called Mo-edge and the S-edge[9]. It has been shown that the structure of nanoparticulate MoS_2 is a single layered truncated triangle primarily exposing the Mo-edge when supported on Au(111)[6,
80 9], Highly Ordered Pyrolytic Graphite (HOPG)[10] or graphitic carbon[11]. Brorson et al[11,12]also found truncated triangles by means of HAADF-STEM (High-Angle Annular Dark-Field-Scanning Transmission Electron Microscopy) in their investigation of MoS_2, WS_2 and cobalt-promoted MoS_2.

85

Estimating the number of active sites on a nanoparticulate catalyst is not trivial. One approach is to measure activity on well defined model systems characterized by STM, for example UHV-deposited nanoparticles[6,13]or physi- or
90 chemisorbed molecular clusters[14]. Another option is to use a well established method to measure electrochemically active surface area such as that used with Pt based on the adsorption-desorption behavior of underpotentially deposited hydrogen,

H_{upd}[15]. We note, however, that this method still relies upon the assumption that the sites active for H_{upd} are the same as those active for the HER. As we are studying metal sulfides where no such method exists, the irreversible oxidation of metal sulfides will be investigated as a measure of their surface area and edge sites.

In the following we will show our investigation of MoS_2, WS_2 and cobalt promoted WS_2 (Co-W-S) and MoS_2 (Co-Mo-S), prepared similarly to the ones imaged by Brorson et al[11] and supported on Toray carbon paper. The electrochemical measurements will be discussed in relation to DFT calculations of ΔG_H for each of the metal sulfates investigated in order to identify structure-composition-activity relationships for these systems.

Results and discussion:

Synthesis and electrochemical characterization of MoS_2.

MoS_2 particles on Toray carbon paper were prepared by dropping 25 µL of an aqueous ammonia heptamolybdate (1mM Mo) solution onto 1 cm^2 of Toray paper. The sample was dried in air at 140 C followed by sulfidation in 10% H_2S in H_2 at 450 C for 4 hours, and subsequently cooled in that same gas stream. This preparation method would typically give the highest current on a per gram basis; higher loadings usually led to lower currents.
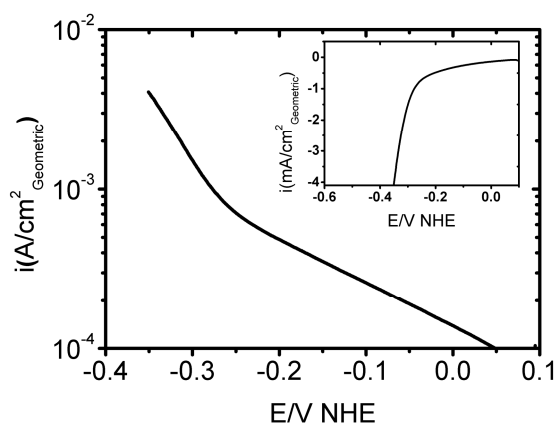
Fig. 1 Tafel plot (main) and polarization curve (inset) in the cathodic potential range of MoS_2 supported on Toray paper. The scan rate is 5 mV/s and the Tafel slope in the HER region is found to be 120 mV/dec.

HER activity was measured (See experimental details) and the results are plotted as Tafel (log i - E) and polarization curves (i-E) in Figure 1. The Tafel plot exhibits a slope of 120 mV/dec and an exchange current density of 4.6 10^{-6}

$A/cm^2_{geometric}$. Samples prepared by different methods have often yielded different Tafel slopes, ranging between 110 mV/dec. and several hundred mV/dec. We attribute this to transport limitations through the fibrous, porous network characteristic of Toray carbon paper. Although sample/substrate preparation could potentially be optimized further, the consistent results achieved using the preparation method described above allows for accurate cross-comparisons among different catalyst materials. It should be noted that hydrogen evolution is taking off at around -0.2 V vs. NHE just as we have previously seen on MoS_2[5,6].

The current measured from approx. +0.1 V vs. NHE to -0.15 V is most likely not due to the HER but rather oxygen reduction at the interface between the electrolyte and the electrode. Finally it should be noted that sweeps between -0.35 and +0.1 V vs. NHE showed negligible change over time, apart from the effects of bubble formation on the electrode.
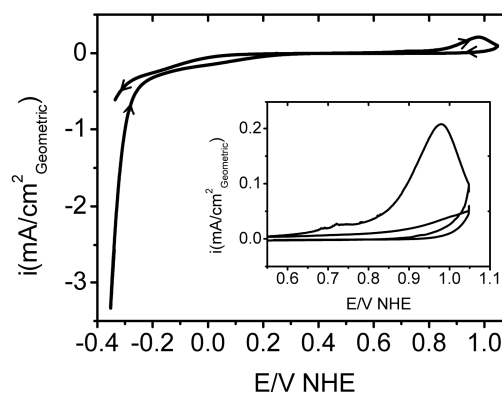

Fig. 2 Cyclic voltammogram of the oxidation and subsequent deactivation of the MoS_2 sample. Scanrate 2mV/s. Main: The deactivation of the sample showing one sweep from -0.35 V vs. NHE to 1.05 V vs NHE and back to -0.35 V vs. NHE. On the 1st anodic sweep an irreversible oxidation peak occurs at 0.6 V vs. NHE and is followed by a subsequent decrease in current at cathodic potentials (-0.35 V vs. NHE), indicating a deactivation of the active sites. Inset: The first and second sweep at anodic potentials showing a significant decrease in the oxidation peak.

Figure 2 shows a cyclic voltammogram of MoS_2/C where the potential is cycled between -0.3 and +1.05 V vs. NHE. At approx. +0.6 V vs. NHE an irreversible oxidation begins to occur with a maximum at +0.98 V vs. NHE. On the subsequent cathodic sweep a significant drop in HER activity is noticed. On the ensuing anodic sweep seen in the inset of Figure 2, the oxidation peak is no longer present. Thus, the loss of HER activity is attributed to irreversible MoS_2 oxidization. In subsequent studies, fresh samples were subjected to CVs in which an initially narrow potential window was widened gradually to more positive (anodic) potentials. It was found that the HER activity of MoS_2/C remained stable with every sweep as long as the anodic potential was limited to ≤ +0.6 V vs. NHE.

MoS₂ electro-oxidation

To our knowledge, the electrochemical oxidation of nanoparticulate MoS_2 is not covered in the literature, which instead focuses on the corrosion of bulk MoS_2. Kautek[16] found that the bulk system preferentially oxidized at the $(10\bar{1}1)$ face and that it did not corrode at the (0001) basal plane. On the nanoparticles this would correspond to corrosion of the particle edges. Closer examination of the insert of Figure 2 reveals two distinct oxidation peaks. The major peak has its maximum at approx. +0.98 V vs. NHE whereas the minor peak has its maximum at approx. +0.7 V vs. NHE. As the edges of MoS_2 nanoparticles are expected to be more readily oxidized than the basal plane[16], we interpret the two distinct oxidation peaks to correspond to the edges (minor peak, +0.7 V vs. NHE) and the basal planes (major peak, +0.98 V vs. NHE) of the particles. While only one cycle to +1.05 V vs. NHE will completely deactivate the sample for the HER, it takes several cycles to +0.7 V vs. NHE to achieve the same effect. This implies that not all edge sites are oxidized with a single sweep to +0.7 V vs. NHE. Had the sample been deactivated for the HER after a single sweep to +0.7 V vs. NHE, we could definitely have used this peak as a measure of the concentration of edge sites. But as this is not the case we will use the major peak at +0.98 V vs. NHE to determine the

total surface area of MoS_2/C. We have however attempted to use the weak feature at +0.7 V vs. NHE to get an estimate of our particle size. At low sweep rates (2 mV/s) the feature is typically not dominated by the major feature at +0.98 V vs. NHE. The area of the edge feature is approx. 8 % of the major peak. If the particles are triangular this corresponds to an edge length of around 25 nm, consistent with the particle sizes observed by Brorson et al[11].

XPS was also employed in this investigation to study the MoS_2/C at three stages of its life: freshly prepared, after HER in H_2SO_4 and after oxidation in H_2SO_4 at high anodic potentials (see experimental details). To obtain a reasonable signal to noise ratio for the XPS studies the Toray paper was dip coated in a 0.14 M Mo solution instead of dropping a known amount of solution on the surface, resulting in a higher loading of Mo than previously described (a factor of 5-10 according to the charge of the oxidation peak). The survey spectra of the different samples showed no contaminants on the freshly prepared samples. On the samples that had been submerged in H_2SO_4 peaks corresponding to sulfate were seen and a peak corresponding to N *1s* was also seen. The N *1s* peak is most likely caused by trace amounts of NH_3 present in air absorbed by H_2SO_4 as $(NH_4)_2SO_4$ with a N *1s* binding energy of 401.3 eV[17].
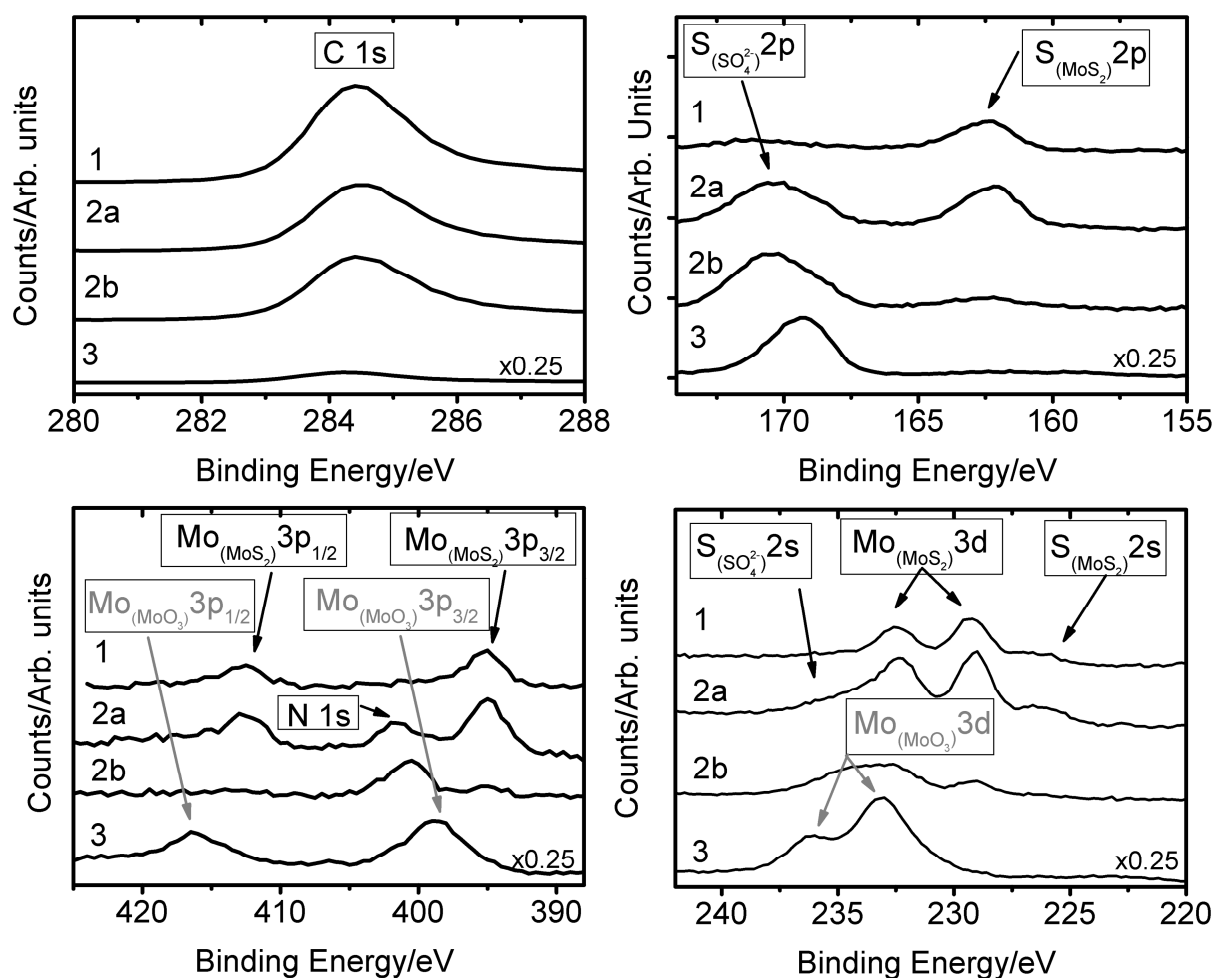
Fig. 3 XPS spectra of MoS$_2$ on Toray paper recorded at different stages of its life. 1): As prepared after sulfidation. 2a): After initial activity measurements of the HER(CVs between +0.1 and -0.4 V vs. NHE). 2b): Sample 2a after measurements of the HER and subsequent oxidation/deactivation (CVs between +1.4 and -0.4 V vs. NHE) and removal from the electrolyte at -0.32 V vs. NHE). 3): After measurements of the HER and subsequent oxidation/deactivation (CVs between +1.4 and -0.4 V vs. NHE) and removal from the electrolyte at 0.4 V vs. NHE.

The XPS data, see Figure 3. reveals that the freshly prepared sample (no. 1) of MoS$_2$ is similar to previously reported spectra[18-20]. The XPS data from a similarly prepared sample that was tested for the HER (sample no. 2a) by sweeping the potential between +0.1 V and -0.45 V vs. NHE, showed an increase in the SO$_4^{2-}$ peak which is to be expected as the sample had been submerged in H$_2$SO$_4$. Apart from the increase in the SO$_4^{2-}$ peak no significant changes were found compared to the freshly prepared sample, indicating that MoS$_2$/C does not change significantly during the HER. After XPS analysis of sample no. 2a was examined for the HER again, then cycled between -0.4 V vs. NHE and +1.4. V vs. NHE and removed from the solution at -0.32 V vs. NHE (sample no. 2b in the XPS spectra). A significant decrease of the Mo *3d*, Mo *3p*, S *2s* and S *2p* peaks was observed and there was no XPS signal corresponding to MoO$_3$. Thus, although the amount of surface Mo decreased significantly it still maintained its Mo^{4+} character(as in MoS$_2$). There are

several possible explanations for the lack of Mo on the surface: (1) The MoS$_2$ desorbs from the surface at high anodic potentials, (2) The oxidation product of MoS$_2$, MoO$_3$, dissolves[21], (3) That MoO$_3$ is reduced to Mo^{3+} at -0.32 V vs. NHE and subsequently dissolves[21]. To answer this question, sample no. 3 was subjected to the same oxidation treatment as sample no. 2b but in this case the sample was pulled out of solution at a higher potential (+0.4 V vs. NHE) where MoO$_3$ is thermodynamically stable according to the Pourbaix diagrams[21]. XPS reveals a shift of the Mo *3d* and Mo *3p* towards higher binding energies just as expected for MoO$_3$. Thus it is unlikely that MoS$_2$ dissolves at anodic potentials.

We note that the Mo peaks of the MoO$_3$ were significantly greater than the Mo peaks observed on the other samples and at the same time the C *1s* peak was significantly smaller. The increase in intensity could be due to a higher loading on this specific sample but we only found a factor of 2 larger oxidation peak on sample 3 than on sample 2a/b. This leads us

to believe that there could be surface enrichment of Mo species on the outermost exposed surface the Toray paper after repeated dissolution-redeposition cycles during each potential sweep.
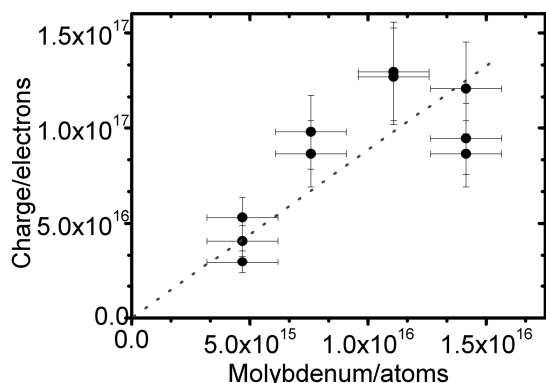
5

Fig. 4 The charge of the irreversible oxidation peak as a function of the amount of Mo used during the synthesis of MoS₂.

10 Having established that the MoS_2 is in fact being oxidized at high anodic potentials we will now elaborate on possible reaction mechanisms. The reaction mechanism will enable us to use the irreversible oxidation peaks to determine the amount of MoS_2 present on the surface. A plot of the 15 correlation between the amount of Mo used during synthesis and the charge of the irreversible oxidation peak is shown on figure 4. In a corrosion study by Jaegermann[18], bulk MoS_2 was electrochemically oxidized in KNO_3 and examined by XPS. A shift toward higher binding energies was observed for the S 20 *2p* and Mo *3d* peaks and a broadening was observed in the S *2p* line. This was interpreted as MoS_2 degradation to SO_4^{2-}, S_2^{2-} and MoO_3. We can with this knowledge consider how many electrons we expect to use to oxidize one Mo atom. If we consider one extreme where the carbon supported MoS_2 is 25 decomposed into MoO_3 and SO_4^{2-} the following reactions would take place, where 18 electrons are transferred per Mo atom

$$MoS_2 + 11\ H_2O \rightarrow MoO_3 + 2\ SO_4^{2-} + 22\ H^+ + 18e^- \qquad (1)$$
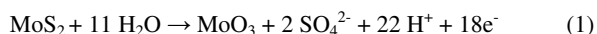
30

The other extreme would be that MoS_2 is decomposed into MoO_3 and S_2^{2-} where 4 electrons are needed

$$MoS_2 + 3\ H_2O \rightarrow MoO_3 + S_2^{2-} + 6\ H^+ + 4e^- \qquad (2)$$
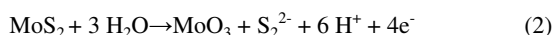
35 According to figure 4 the correlation between the oxidation peak and the deposited amount of Mo yields 8.9 (r^2 =0.55) electrons per Mo atom used in the deposition. This number is in between the two extremes mentioned above. Revisiting the XPS data we can not see whether we have produced excess 40 SO_4^{2-} due to the background of H_2SO_4. We are however also

not seeing any significant amounts S_2^{2-} after cyclic voltammetry. While the samples have been subject to a high anodic (1.4 vs. NHE) potential where S_2^{2-} can be oxidized to SO_4^{2-} the subsequent high cathodic (-0.4 vs. NHE) potential 45 can reduce the S_2^{2-} to H_2S[21]. We can not conclusively determine the exact nature of the oxidation reaction. But our measurements indicate that the sulfur in the MoS_2 is only partially oxidized during anodic sweeps, resulting in the following proposed reaction mechanism:

50

$$MoS_2 + 7\ H_2O \rightarrow MoO_3 + SO_4^{2-} + \tfrac{1}{2}\ S_2^{2-} + 14\ H^+ + 10\ e^- \qquad (3)$$
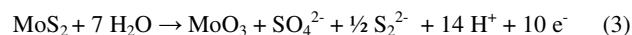
HER activity of MoS₂/C

55 In order to determine the activity of the MoS_2/C system per active site, we start with the irreversible oxidation to estimate the total surface area of MoS_2 on the Toray paper. The irreversible oxidation peak of the sample shown in Figure 1 and Figure 2 has a charge of 0.014 C. If we assume that 10 60 electrons are involved in the oxidation of MoS_2, as presented in the previous section, the surface area will be 4.2 cm² of single layered MoS_2 giving an exchange current density(i_0) of $1.1*10^{-6}$ A/cm² (and a Tafel slope of 120mV/dec). We have previously shown that the active sites of Au(111) supported 65 MoS_2 nanoparticles are situated on the edge[6](i_0 =$7.9*10^{-6}$ A/cm²).

The exchange current density on a per active site basis will clearly be higher than the exchange current densities reported 70 above since few of the MoS_2 sites are on the edge. Thus the values above constitute a lower bound for activity. If we incorporate the fact that the MoS_2 nanoparticles are triangular with an edge length of 25 nm approx. 8 % of the atoms will be situated at the edge of the particle. This would lead to a 12- 75 fold increase in exchange current density per active site.

Electrochemical characterization of WS₂

WS_2 exhibits a layered structure similar to MoS_2[11,12], forming 80 the same triangular shape as MoS_2 when prepared under similar conditions. WS_2 supported on SiO_2 has previously been proposed as a catalyst for the hydrogen evolution reaction[22].
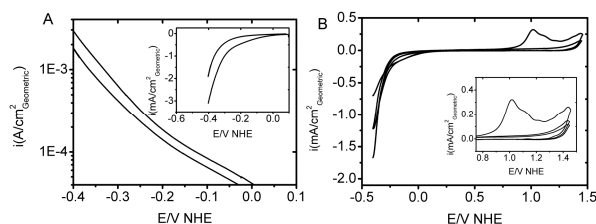
85

5 The WS$_2$ was studied on Toray paper and the preparation method was similar to that of the MoS$_2$ samples (See experimental details). In Figure 5 the results of the electrochemical measurements are shown. Figure 5 A) shows a Tafel plot (log i - E) and a polarization curve (i - E) in the

10 region where we have previously observed hydrogen evolution on MoS$_2$ samples. On the polarization curve (inset of Figure 5 A)) the cathodic current increases at potentials more negative than -0.2 V vs. NHE ascribed to HER activity. The Tafel slope on this sample is found to be 135mV/dec.

15 indicating that the current could be transport limited. Figure 5 b) shows the deactivation of the sample at positive potentials. As with the MoS$_2$/C sample, an oxidation feature is observed with a peak at approx. 1 V vs. NHE, and on consecutive sweeps the peak disappears concurrent with a drop in the HER

20 current. This is the same behavior as we have seen on the MoS$_2$/C sample except that the WS$_2$ sample required two sweeps towards highly anodic potentials before the HER current was affected. This behavior was also observed with high loadings of MoS$_2$/C samples that surely had formed

25 multilayer's. In this case, the outer layer could be passivated by a sulfur/oxide layer, thus requiring several oxidation/reduction steps to completely dissolve the metal sulfide. Apart from the potential formation of multilayer's the oxidation of the WS$_2$ is similar to that of MoS$_2$/C and it is

30 assumed that the oxidation process is similar to that of MoS$_2$/C.

Cobalt promoted MoS$_2$ and WS$_2$

35 Cobalt is often used to promote WS$_2$ and MoS$_2$ in catalyzing the hydrodesulfurization reaction. Both the structural and the catalytic effect of adding cobalt has been extensively studied[2]. It is widely accepted that the cobalt is located at the edge of MoS$_2$, more specifically the so called S-edge(-1010). Cobalt

40 promotion of MoS$_2$ has also been shown to change the morphology significantly[11]. Cobalt promoted MoS$_2$ is usually found as truncated triangles exposing the S-edge$\left(\bar{1}010\right)$ predominantly, unlike the unpromoted MoS$_2$, in which the triangles are less truncated and primarily expose their Mo-

45 edge(10-10)[23]. In the following we will show data for sulfided Co and Co promoted WS$_2$ and MoS$_2$.

Electrochemical characterization of cobalt sulfide CoS$_x$)

50 The first step in testing the promotion by cobalt is the test of sulfided cobalt itself. We have used Co(acetate) as the Co precursor as described in[11]. The precursor was sulfided under the same conditions as the MoS$_2$ and the WS$_2$ samples (see experimental details). The Co is expected to be in the form of

55 Co$_8$S$_9$ immediately after sulfidation, but as this form is not stable in air[24] our Co sulfide is most likely partially sulfided
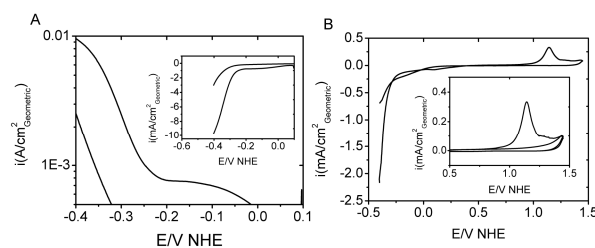
(CoS$_x$).

60 **Fig. 6** A:Tafel and polarization curve(inset) of CoS$_x$/C, both the initial and the final stable scan is shown. B: CV of CoS$_x$/C showing the oxidation/deactivation of CoS$_x$

Figure 6 A) shows the initial and the stable Tafel (log i - E)

65 and polarization curves (i - E) within a narrow potential window (maximum +0.1 V vs. NHE). Initially the activity is high, but unlike MoS$_2$ and WS$_2$, subsequent sweeps within this potential window show a significant decrease in activity. The decrease is most likely due to the CoS$_x$ instability in

70 sulfuric acid, introducing ambiguity into the interpretation of the current at cathodic potentials as the HER competes with cathodic desorption or dissolution of CoS$_x$. In Figure 6 B) a wide sweep is exhibited. The CoS$_x$ exhibits similar oxidation features as we have seen on the MoS$_2$ and WS$_2$, but in this

75 case the oxidation peak is shifted towards a higher potential(1.14 V vs. NHE). After oxidation the HER activity drops just as with MoS$_2$ and WS$_2$, again indicating oxidation of the material.

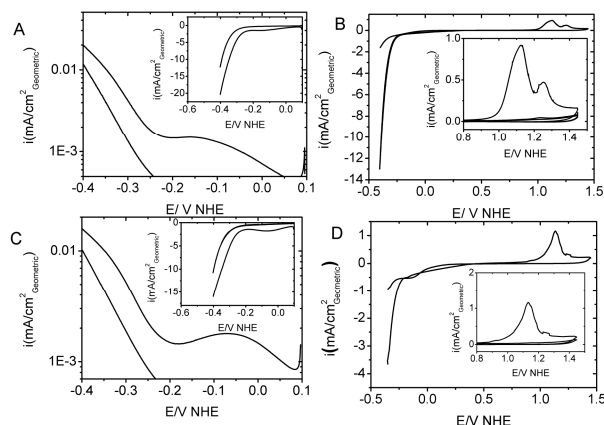80 ## Cobalt promoted MoS$_2$(Co-Mo-S) and WS$_2$(Co-W-S)

Fig. 7 A,C:Tafel and polarization curve(inset) of Co-Mo-S(A) and Co-WS(C), the scan rate is 5 mV/S both the initial and the final stable scan is shown. B,D: CV of Co-Mo-S(B) and Co-W-S(D) showing the

85 deactivation of Co-Mo-S and Co-W-S.

The Co promoted WS$_2$ and MoS$_2$ was prepared by co impregnation of the Mo/W and the Co precursor (see experimental details). Figure 7 A) and C) shows the Tafel (log i - E) and the polarization (inset) curve (i - E) within a

90 narrow potential window (maximum +0.1 V vs. NHE). The

HER current diminishes just as on the pure CoS_x sample: it is initially high and after subsequent sweeps the current decreases noticeably, but unlike the case of pure CoS_x, remains stable at a fairly high level. This indicates that some of the Co promoter is in the state of CoS_x, but as the current stabilizes at a higher level than pure CoS_x, MoS_2 or WS_2 the remaining Co must have a promotion effect. The Tafel slopes are also in the expected region (Co-W-S 132 mV/dec., Co-Mo-S 101 mV/dec.). In Figure 7 B) and D) the CVs within a wide potential window are shown and just as on the other metal sulfides we observe an irreversible oxidation peak followed by a significant decrease in HER activity. The peak maximum, however, seems to be shifted to a more anodic potential (approx. 1.1 V vs. NHE) than those corresponding to the unpromoted MoS_2 and WS_2.

DFT calculations on WS_2, MoS_2, Co-Mo-S and Co-W-S
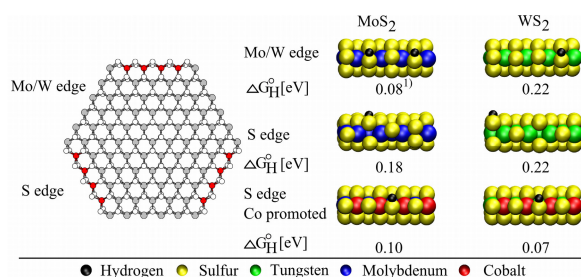
Fig. 8 Left: Ball model of a Mo/WS_2 particle exposing both S edge and Mo/W edge. Right: Differential free energies of hydrogen adsorption. 1) from reference[5].

We have calculated ΔG_H at the S edge $(\bar{1}010)$ and the Mo/W edge $(10\bar{1}0)$ of WS_2 and MoS_2 and on the Co promoted S edge $(\bar{1}010)$ edge of WS_2 and MoS_2 over a wide range of S coverage and H coverage. The choice of the relevant edge configurations have been based on the chemical potential of hydrogen and sulfur at the experimental sulfiding conditions using a thermodynamic model similar to the one presented in[25] . The structure and the differential free energies of H adsorption for these structures can be seen in Figure 8. The results indicate that non promoted WS_2 and MoS_2 nanoparticles should be reasonably good hydrogen evolution catalysts since both edges on both systems have free energies of adsorption close to zero. Hydrogen evolution on MoS_2 is expected to take place predominantly at the Mo edge ($\Delta G_H = 0.08$ eV) rather than the S edge ($\Delta G_H = 0.18$ eV), while for WS_2 both edges are equally good ($\Delta G_H = 0.22$ eV). Given these values for ΔG_H, non-promoted MoS_2 is predicted to be a better hydrogen evolution catalyst than WS_2.

The incorporation of cobalt into the edge structures of both WS_2 and MoS_2 is expected to have a promotion effect. The cobalt only incorporates itself into the S edge of both cases, so ΔG_H values at the Mo/W edge remain unaffected. At the S edge, however, ΔG_H is reduced to 0.10 eV and 0.07 eV for MoS_2 and WS_2, respectively (down from 0.18 eV and 0.22 eV). We note that the free energy of hydrogen adsorption at

the cobalt-promoted S edge of MoS_2 is very similar to the free energy of hydrogen adsorption on the Mo edge of MoS_2. Therefore, for MoS_2 the effect of promotion is the increase in the number of sites with high activity. On WS_2 the effect of cobalt promotion is the creation of new sites with higher activity than that prior to promotion.

In comparing all catalyst systems, DFT calculations suggest that cobalt-promoted MoS_2 (Co-Mo-S) should be a better catalyst than Co promoted WS_2 (Co-W-S) because it would have active sites on both edges and therefore a higher total number of active sites.

Linking catalyst structure and composition to HER activity

Calculated DFT values are best compared to experimental data where the activity has been normalized with respect to the number of active sites on the catalyst, in this case the number and type of edge sites on the different metal sulfides. We accomplish this normalization by using the irreversible oxidation features of each sulfide.
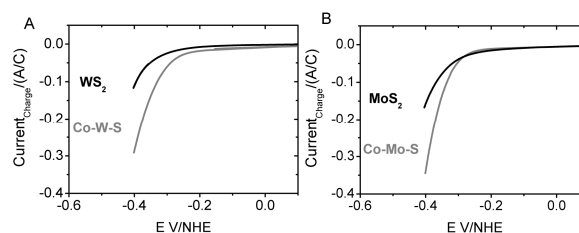

Fig. 9 Polarization curves where the currents of the different metal sulfides have been normalized with respect to the charge of the irreversible oxidation peak. A: Polarization curve of the HER on WS_2 and cobalt promoted WS_2(Co-W-S).B: Polarization curve of the HER on MoS_2 and cobalt promoted MoS_2(Co-Mo-S).

Figure 9 exhibits normalized polarization curves (E- i) pertaining to each of the different samples. There is an apparent promotion effect of Co on both the MoS_2 and the WS_2 samples. The promotion effect on the WS_2 sample can be explained by the DFT calculations predicting that the Co promotion should decrease the free energy of hydrogen adsorption from 0.22 eV to 0.07 eV on the S-edge and thus effectively increase the activity of the active site. MoS_2 is a slightly different case. It has previously been found that MoS_2's Mo-edge, which has a ΔG_H of 0.08 eV, is the major edge exposed, and that this edge does not adsorb cobalt[23, 26, 27]. However, the inhomogenous nature of these nanoparticulate catalysts suggests that both the Mo-edge and the S-edge will be present in significant fractions. Thus, the cobalt on MoS_2's S-edge promotes the HER as its free energy of hydrogen adsorption is decreased from 0.18 eV to 0.10 eV. In other words, the number of active sites is increased since the normally less active S-edges becomes more active in the

presence of cobalt.

Experimental/Calculation details

Toray carbon paper was used as support material because it is inert, of high purity, has high conductivity and because it has adsorption sites/defects that will anchor the metal sulfide particles. The Toray paper was cut into strips that were 1 cm wide and 5 cm long. The Toray paper was loaded with catalyst by wetness impregnation with an aqueous solution of $(NH_4)_6Mo_7O_{24}.4H_2O$ in the case of MoS_2 and an aqueous solution of $H_{24}N_6O_{39}W_{12}.xH_2O$ in the case of WS_2. In the case of the sulfided Co, $C_4H_4CoO_4.4H_2O$ in an aqueous solution was used. The promoted WS_2 and MoS_2 were made by co-impregnation of Co and Mo/W. The impregnation of the pure sulfides was done by dropping a 25 μL aliquot (0.3-1 mM for Mo, 0.8 mM for W, 4mM for Co). The co-impregnation of the promoted sulfides was done by adding a 25 μL aliquot of Mo(0.7mM) or W(0.8 mM) solution followed by a 25 μL aliquot of Co(4mM) solution. A different sample preparation was used for the MoS_2 sample for XPS analysis where a the Toray paper was dip coated in the Mo solution(0.14 M) to obtain a more uniform impregnation.

The samples were dried at 140 ˚C and afterwards sulfided in a tube furnace under 10% H_2S in H_2 at 450 ˚C for 4 hours. The samples were cooled down in the same gas stream.

The electrochemical measurements where performed in N_2 purged 0.5 M H_2SO_4 (pH 0.4). To avoid contamination from the SCE reference electrode a salt bridge was used. A Pt mesh was used as the counter electrode.

The XPS data was recorded using a Perkin-Elmer surface analysis system (Physical Electronics Industries Inc., USA) with a chamber base pressure of 10^{-10} Torr.

Al-Kα radiation (1486.6 eV) was used for excitation. The XPS scans on Figure 4 were measured with a pass energy of 100 eV, a step size of 1 eV, and 250 ms/step.

DFT calculations

An infinite stripe model, which has previously been proven successful to investigate MoS_2 based systems [5, 28-30] ,is used to investigate the edges of MoS_2. The infinite stripe exposes both the $(10\bar{1}0)$ Mo edge and the $(\bar{1}010)$ S edge. The supercell has 4 Mo atoms in the x-direction and 4 Mo atoms in the y-direction, in order to allow for important reconstructions with a period of 2 in the x direction and to allow decoupling of the Mo edge and the S edge in the y-direction. The stripes are separated by 14.8Å in the z-direction and 9Å in the y-direction.

The plane wave density functional theory code *DACAPO* [31, 32] is used to perform the DFT calculations. The Brillouin zone is sampled using a Monkhorst-Pack k-point set[33] containing 4 k-points in the x-direction and 1 k-point in the y- and z-direction. The calculated equilibrium lattice constant is 3.235Å and 3.214Å for MoS_2 and WS_2 respectively. A plane-wave cutoff of 30 Rydberg and a density wave cutoff of 45 Rydberg are employed using the double-grid technique[34]. Ultrasoft pseudopotentials are used except for sulfur, where a soft pseudopotential is employed[35, 36]. A Fermi temperature of $k_BT=0.1eV$ is used for all calculations and energies are extrapolated to zero electronic temperature. The exchange correlation functional RPBE is used. The convergence criterion for the atomic relaxation is that the norm of the total force should be smaller than 0.15eV/Å, which corresponds approximately to a max force on one atom below 0.05eV/Å . Figures of atomic structures have been made using VMD[37]. The differential free energies are calculated as described in [5] where 0.29eV is added to the pure DFT energy of adsorption in order to take zero point energy and entropy into account.

Conclusions

We have studied the hydrogen evolution on Co promoted and unpromoted nanoparticulate MoS_2 and WS_2 structures. Cyclic voltammetry revealed that they are irreversibly oxidized at high anodic potentials. We have used the irreversible oxidation features to determine the surface area of MoS_2 and proposed a possible oxidation mechanism of MoS_2. XPS analysis showed no change in the oxidation state of MoS_2 after HER measurements, but after oxidation at potentials above 0.6 V vs. NHE MoS_2 was oxidized. We found that the activity of the carbon supported MoS_2 is comparable to that of our previously published results on Au(111) supported MoS_2. WS_2 has a similar structure and was also investigated in this study. It was found to irreversibly oxidize at high anodic potentials, just like MoS_2 and was found to be almost as active. Tests of Cobalt promoted MoS_2 and WS_2 samples were also performed and Co is indeed promoting the HER in both cases. The findings are corroborated by DFT calculations showing that the activity of the different samples should be $WS_2<MoS_2=Co-Mo-S<Co-W-S$.

Notes and references

[a] *Center for Individual Nanoparticle Functionality (CINF),*
Department of Physics, Technical University of Denmark,
DK-2800 Lyngby, Denmark
[b] *Center for Atomic-scale Materials Design (CAMd),*
Department of Physics, Technical University of Denmark,
DK-2800 Lyngby, Denmark

c *Department of Chemical Engineering, Stanford University, 381 North-South Mall, Stauffer III, Stanford, CA 94305-5025, USA*
corresponding author: ibchork@fysik.dtu.dk

5 1 J. Greeley, T. F. Jaramillo, J. Bonde, I. B. Chorkendorff and J. K. Nørskov, *Nature Materials,* 2006, **5**, 909-913.

2 H. Topsøe, B. S. Clausen and F. E. Massoth, *Hydrotreating Catalysis*, Springer-Verlag, Berlin, 1996.

3 H. Tributsch, *Zeitschrift Fur Naturforschung Section A-a Journal of*
10 *Physical Sciences,* 1977, **32**, 972-985.

4 J. P. Wilcoxon, *J Phys Chem B,* 2000, **104**, 7334-7343.

5 B. Hinnemann, P. G. Moses, J. Bonde, K. P. Jorgensen, J. H. Nielsen, S. Horch, I. Chorkendorff and J. K. Nørskov, *J Am Chem Soc,* 2005, **127**, 5308-5309.

15 6 T. F. Jaramillo, K. P. Jørgensen, J. Bonde, J. H. Nielsen, S. Horch and I. Chorkendorff, *Science : International Edition - AAAS,* 2007, **316**, 100-101.

7 J. K. Nørskov, T. Bligaard, A. Logadottir, J. R. Kitchin, J. G. Chen, S. Pandelov and U. Stimming, *J. Electrochem. Soc.,* 2005, **152**, J23.

20 8 J. Greeley, J. K. Nørskov, L. A. Kibler, A. M. El-Aziz and D. M. Kolb, *Chemphyschem,* 2006, **7**, 1032-1035.

9 S. Helveg, J. V. Lauritsen, E. Lægsgaard, I. Stensgaard, J. K. Nørskov, B. S. Clausen, H. Topsøe and F. Besenbacher, *Phys. Rev. Lett.,* 2000, **84**, 951-954.

25 10 J. Kibsgaard, J. V. Lauritsen, E. Laegsgaard, B. S. Clausen, H. Topsoe and F. Besenbacher, *J. Am. Chem. Soc.,* 2006, **128**, 13950-13958.

11 M. Brorson, A. Carlsson and H. Topsøe, *Catalysis Today,* 2007, **123**, 31-36.

12 A. Carlsson, M. Brorson and H. Topsøe, *J. Catal.,* 2004, **227**, 530-536.

30 13 J. Meier, K. A. Friedrich and U. Stimming, *Faraday Discuss.,* 2002, **121**, 365-372.

14 T. F. Jaramillo, J. Zhang, B. L. Ooi, J. Bonde, K. Andersson, J. Ulstrup, J. K. Nørskov and I. Chorkendorff, In preparation 2008,.

15 N. M. Markovic and P. N. Ross, *Surface Science Reports,* 2002, **45**,
35 121-229.

16 W. Kautek and H. Gerischer, *Surface Science,* 1982, **119**, 46-60.

17 C.D. Wagner, A. V. Naumkin, A. Kraut-Vass, J. W. Allison, C. J. Powerll and J. R. Rumble Jr., *NIST X-Ray Photoelectron Spectroscopy Database, Standard Reference Database 20, Version 3.4 (2008)*
40 *http://srdata.nist.gov/xps.*

18 W. Jaegermann and D. Schmeisser, *Surface Science,* 1986, **165**, 143-160.

19 T. Weber, J. C. Muijsers, H. J. M. C. van Wolput, C. P. J. Verhagen and J. W. Niemantsverdriet, *J. Phys. Chem.,* 1996, **100**, 14144-14150.

45 20 J. H. Nielsen, K. P. Jørgensen, J. Bonde, K. Nielsen, L. Bech, Y. Tison, S. Horch, T. F. Jaramillo and I. Chorkendorff, In preparation 2008,.

21 M. Pourbaix, *ATLAS OF ELECTROCHEMICAL EQUILIBRIA...*, 1966.

50 22 A. Sobczynski, A. Yildiz, A. J. Bard, A. Campion, M. A. Fox, T. Mallouk, S. E. Webber and J. M. White, *J. Phys. Chem.,* 1988, **92**, 2311-2315.

23 J. V. Lauritsen, J. Kibsgaard, G. H. Olesen, P. G. Moses, B. Hinnemann, S. Helveg, J. K. Nørskov, B. S. Clausen, H. Topsøe, E.
55 Lægsgaard and F. Besenbacher, *Journal of Catalysis,* 2007, **249**, 220-233.

24 I. Alstrup, I. Chorkendorff, R. Candia, B. S. Clausen and H. Topsøe, *Journal of Catalysis,* 1982, **77**, 397-409.

25 M. V. Bollinger, K. W. Jacobsen and J. K. Nørskov, *Phys Rev B,* 2003, **67**, 085410.

60 26 P. Raybaud, J. Hafner, G. Kresse, S. Kasztelan and H. Toulhoat, *J Catal,* 2000, **190**, 128-143.

27 H. Schweiger, P. Raybaud and H. Toulhoat, *Journal of Catalysis,* 2002, **212**, 33-38.

28 B. Hinnemann, J. K. Nørskov and H. Topsøe, *J Phys Chem B,* 2005,
65 **109**, 2245-2253.

29 J. V. Lauritsen, M. Nyberg, R. T. Vang, M. V. Bollinger, B. S. Clausen, H. Topsøe, K. W. Jacobsen, E. Lægsgaard, J. K. Nørskov and F. Besenbacher, *Nanotechnology,* 2003, **14**, 385-389.

30 L. S. Byskov, J. K. Nørskov, B. S. Clausen and H. Topsøe, *J Catal,*
70 1999, **187**, 109-122.

31 S. R. Bahn and K. W. Jacobsen, *Comput Sci Eng,* 2002, **4**, 56-66.

32 B. Hammer, L. B. Hansen and J. K. Nørskov, *Physical Review B,* 1999, **59**, 7413-7421.

33 H. J. Monkhorst and J. D. Pack, *Phys Rev B,* 1976, **13**, 5188-5192.

75 34 K. Laasonen, A. Pasquarello, R. Car, C. Lee and D. Vanderblit, *Phys Rev B,* 1993, **47**, 10142-10153.

35 N. Troullier and J. L. Martins, *Phys Rev B,* 1991, **43**, 1993-2006.

36 D. Vanderbilt, *Phys. Rev. B,* 1990, **41**, 7892-7895.

37 W. Humphrey, A. Dalke and K. Schulten, *J. Mol. Graph.,* 1996, **14**, 33

80

Included Publications

Paper 5:

"Hydrogen Evolution on supported incomplete cubane-type $[Mo_3S_4]^{4+}$ electrocatalyst"
T. F. Jaramillo, <u>J. Bonde</u>, J. Zang, B. L. Ooi, J. Ulstrup and I. Chorkendorff,
Submitted Journal of Physical Chemistry C, (2008)

Included Publications

Hydrogen Evolution on supported incomplete cubane-type [Mo3S4]4+ electrocatalysts

Hydrogen Evolution on supported incomplete cubane-type $[Mo_3S_4]^{4+}$ electrocatalysts

Thomas F. Jaramillo[1], Jacob Bonde[2],Jingdong Zhang[3], Bee-Lean Ooi[3] , Klas Andersson[2],

Jens Ulstrup[3], Ib Chorkendorff [2]*.

1 *Department of Chemical Engineering, Stanford University, 381 North-South Mall, Stauffer III,*

Stanford, CA 94305-5025, USA

2 Center for Individual Nanoparticle Functionality (CINF), Department of Physics

3 Department of Chemistry

Technical University of Denmark

DK-2800 Lyngby, Denmark

* Corresponding author:

Email: ibchork@fysik.dtu.dk

Phone: (45) 4525 3170

Fax: (45) 4593 2399

RECEIVED DATE

Abstract:

Electrocatalytic properties of biomimetic supported incomplete cubane-type $[Mo_3S_4]^{4+}$ clusters are investigated. The activity towards the hydrogen evolution reaction (HER) is evaluated on both a high surface area gas diffusion electrode in a membrane electrode assembly and on highly orientated pyrolytic graphite (HOPG) supports. Submonolayers of the clusters were imaged by means of scanning tunnelling microscopy(STM) prior to electrochemical characterization. This enabled the quantification of the activity on a per cluster basis for the HER and the comparison of the activity with other HER catalysts. We find that the HER activity of the $[Mo_3S_4]^{4+}$ is comparable with that of the edge sites of MoS_2. On the basis of these studies, supported $[Mo_3S_4]^{4+}$-molecules were investigated by X-ray Photoelectron Spectroscopy(XPS) and the observed deterioration in electrocatalytic activity with time was assigned to slow $[Mo_3S_4]^{4+}$ cathodic desorption from the catalyst support.

Keywords: Hydrogen evolution, Electrocatalysis, $[Mo_3S_4]^{4+}$, XPS, STM, Biomimetics.

1. Introduction.

Interfacial electrocatalytic charge transfer processes are at the heart of future energy conversion. Decades of research into conventional metals and alloys has paved the way for the development of the electrocatalytic materials used in today's commercial devices including fuel cells and electrolyzers[1]. A number of challenges, however, remain in developing active, stable, and low-cost catalysts. Sulfur-rich transition metal clusters have attracted much attention due to their inherently interesting chemistry and by their structural and functional relevance to redox metalloproteins and metalloenzymes[2-11]. The latter observations offer particular perspectives for the potential use of such clusters in heterogeneous catalysis and interfacial electrocatalysis.

Monolayers of a variety of redox metalloenzymes in protein film voltammetry can be brought to retain electrocatalytic electron transfer and redox enzyme function in the immobilized state on, usually modified, electrode surfaces. These enzymes include iron-sulfur cluster-based enzymes as well as Mo-

enzymes in processes such as fumarate reduction and succinate oxidation, nitrate reduction, DMSO reduction and particularly, hydrogen evolution and proton reduction[12-14]. Although of great importance, redox metalloenzyme function is, however, unlikely to carry over as large-scale industrial electrocatalysts. This is due to their high cost and fragile nature in non-native surroundings outside their natural biological environments. Even though the individual enzyme molecule may be catalytically highly active, the large size of the molecules also means that the number of enzyme molecular sites on the surface in a full monolayer is much smaller than the number of active sites on metallic catalytic surfaces.

Biomimetic electrocatalysts based on chemically synthesized low-cost, earth-abundant metal-containing groups that resemble the active core groups in redox metalloenzymes may, on the other hand be able to retain electrocatalytic activity at a small size. The heme group as the core group in a broad variety of heme proteins is an example of such a robust and catalytically specific molecular electrocatalyst[15-19] Synthetic iron-sulfur cubane-like structures resembling the core metal centres in iron-sulfur proteins and metalloenzymes have also been studied extensively by Holm and associates[2-5]. These are, however, fragile and difficult to handle, and they have not been addressed with a view on interfacial electrocatalysis.

Polynuclear sulfide-containing Mo-complexes offer instead a class of robust and relatively easier-to-handle homologues to the iron-sulfur cubane-type clusters The trimeric, incomplete cubane-type cluster aqua ion, $[Mo_3S_4(H_2O)_9]^{4+}$ ($[Mo_3S_4]^{4+}$), in particular has been extensively investigated[5], see Figure 1. $[Mo_3S_4]^{4+}$ is extremely stable, but electrochemically reactive, and when coordinated to ligands such as iminodiacetate, evidence for three different oxidation states has been obtained[6]. This suggests that its electrocatalytic activity may be promising. $[Mo_3S_4]^{4+}$ reacts readily with a range of metals or metal ions to form heterometallic complete cubane-type clusters, $[Mo_3MS_4]^{n+}$ (M = Pd, Pt, Ru, Ni, Fe, etc.), thus offering possibilities for tuning of the redox potential and other catalytically important properties. Several of these heterometallic cubane-type $[Mo_3MS_4]^{n+}$ clusters appeared to be catalytically active, for example, in hydrazine N-N cleavage reactions[7], lactonization of alkynoic acids[8], hydrodesulfurization[9],

and other organic chemical reactions[10]. The recently reported spontaneous adsorption of $[Mo_3S_4]^{4+}$ on Au(111) surfaces resulting in $[Mo_3S_4]^{4+}$-monolayer formation[11] is also noteworthy. It is the first example of monolayer formation *in situ* by a polynuclear metal-sulfide cluster directly anchored onto the gold surface and structurally mapped to single-molecule resolution by scanning tunnelling microscopy directly in aqueous electrolyte solution (*in situ* STM). Coupled with the different accessible redox-states for polynuclear metal-sulfide clusters, this has sparked off the idea of exploiting the $[Mo_3S_4]^{4+}$ for functionalization of other materials.

We report here comprehensive data for supported incomplete cubane-type $[Mo_3S_4]^{4+}$ as an intriguing new class of materials that holds promise for efficient electrocatalysis of one of the altogether most important electrochemical processes, the electrochemical hydrogen evolution reaction (HER). Flexibility in cluster synthesis, composition, and structure may allow for new electrode materials to be tailored based on these relatively low-cost, earth abundant elements. We provide voltammetric current-overpotential relations on carbon-supported (high surface area carbon and highly oriented pyrolytic graphite, HOPG) multi- and monolayers of the $[Mo_3S_4]^{4+}$ molecules. STM of the cluster molecules on activated HOPG that "resemble" the high surface area carbon, resolved to the level of the single molecule, enables further direct comparison between the macroscopic electrochemical exchange currents and the density of molecules on the surface. Catalytic activity per molecule can be estimated in this way. Comprehensive electronic characterization of different states of the $[Mo_3S_4]^{4+}$ molecules using X-ray Photo-electron Spectroscopy (XPS) has finally been achieved.

Models of catalysis that allow us to understand catalytic reactions at a molecular level have emerged in recent years[20, 21]. By carefully examining the active site of working systems, we can identify the material (or site) properties that principally control electrocatalytic activity and then search for other, less expensive, systems that emulate these properties. As noted, the HER is an important interfacial electrochemical process that could have a crucial role in a future hydrogen economy[22]. In 1958, Parsons[23] first proposed the descriptor for facile hydrogen evolution, i.e. thermo-neutral H-adsorption from electrochemical reduction of the solute proton . Optimal catalytic surfaces are those which exhibit

a Gibbs free energy of electrochemical H-adsorption (ΔG_H) close to zero, a notion which has recently

gained much more attention. Recent DFT calculations have shown that there is indeed a correlation

between calculated values of ΔG_H and experimentally measured exchange current densities on a wide

range of materials[24-27].

In approaching catalytic materials discovery, we have previously aimed to emulate enzymatic catalysis

using solid-state materials[27, 28]. The edge sites of nanoparticulate MoS_2 mimics, in many ways the

metallic active sites in the nitrogenase and hydrogenase enzymes, both of which evolve hydrogen from

protons in a facile manner without the use of precious metals[27, 28]. Structurally speaking, the primary

commonality between the enzymatic active center and the MoS_2 edge is under-coordinated sulfur, which

in both cases was shown to be the active site for the HER [27] as determined by DFT calculations[28]. The

$[Mo_3S_4]^{4+}$ studied herein also exhibits this structural commonality, inspiring further study of

electrocatalytic reactions, and the HER in particular.

The incomplete cubane-type $[Mo_3S_4]^{4+}$ was first synthesized nearly two decades ago[6], but studies of

electrocatalytic activity have not been reported before. In this report we present data for the electro-

catalytic activity of $[Mo_3S_4]^{4+}$ on a high surface area carbon support (Vulcan xc72) followed by a more

detailed study of the adsorption and electro-catalytic activity of individually separated $[Mo_3S_4]^{4+}$

molecules supported onto HOPG surfaces. By combining electrochemistry with surface science

techniques, we have investigated and assessed this new class of bio-mimetic, solid-state electrocatalysts.

2. Experimental Methods

2.1. Synthesis of $[Mo_3S_4]^{4+}$.

$[Mo_3S_4]^{4+}$ was synthesized by reduction of either ammonium tetrathiomolybdate or the $Mo(V)_2$ aqua

ion, $[Mo_2O_2S_2(H_2O)_6]^{2+}$, with sodium borohydride, as reported in the literature[29, 30]. Solutions of

$[Mo_3S_4]^{4+}$ in H_2SO_4 were obtained by repeated cation-exchange chromatography (Dowex 50W-X2, 400

mesh) and checked by UV-Vis spectroscopy (Hewlett Packard 8453).

2.2. $[Mo_3S_4]^{4+}$-electrode preparation

Phosphate buffer (PB) solutions were prepared from Suprapur® chemicals, di-potassium hydrogen phosphate (K_2HPO_4, 99.99%) and potassium dihydrogen phosphate (KH_2PO_4, 99.995%). The $[Mo_3S_4]^{4+}$/HOPG samples were prepared in two different ways. One is to directly cast a drop (50 µl) of $[Mo_3S_4]^{4+}$ solution (1.8 mM $[Mo_3S_4]^{4+}$ in 0.4 M H_2SO_4) onto a freshly cleaved HOPG surface. Physical adsorption is the main interaction between the adsorbate and HOPG surface in this procedure. The drop was allowed to dry in a desiccator and the sample was used as such after a single rinse with a drop of water. This simple method works efficiently with hydrophobic molecules for which hydrophobic interactions are the driving force in stable adlayer formation. However, a stable adlayer for hydrophilic molecules cannot easily be maintained in this way. The HOPG surface must first be activated into a hydrophilic form compatible with a hydrophilic adsorbate such as $[Mo_3S_4]^{4+}$. In the second method, the HOPG was thus activated prior to drop-casting. The activation of HOPG was carried out in pH 7.0 PB solution by the electrochemical method in reference [31]. Immediately after activation and rinsing, a freshly prepared 50 µL aliquot of 1.8 mM $[Mo_3S_4]^{4+}$ in 0.4 M H_2SO_4 (aq.) was drop-casted onto the activated HOPG surface and soaked for 2 hours. Excess solution was washed away by thorough rinsing with Millipore water (18.2 MΩ·cm).

2.3 Electrochemical measurements in a three-electrode cell

Cyclic voltammograms of the HER in de-aerated 0.5 M H_2SO_4 (pH 0.40) were conducted. An O-ring seal was used to expose only the STM-imaged part of the sample to the electrolyte. The cyclic voltammogram sweep rate was 5 mV/s. A SCE and a Pt mesh were used as reference and counter electrode, respectively.

2.4. Electrochemical measurements in a membrane electrode assembly (MEA)

2.4.1. MEA preparation

1 mL $[Mo_3S_4]^{4+}$ solution (40mM $[Mo_3S_4]^{4+}$ in 4M H_2SO_4) was wet-impregnated on 160 mg of Carbot xc72 carbon black and dried. An ink was then prepared with 44 mg of the carbon supported $[Mo_3S_4]^{4+}$, 0.1 mL wt % Nafion® solution (5 % wt. in a mixture of lower aliphatic alcohols and water) and 0.2 mL methanol (99.99 %). The ink was sonicated for 40 min, drop-cast on a 3.14 cm^2 graphite paper disk (Toray) and dried to create a gas diffusion electrode (GDE) with $[Mo_3S_4]^{4+}$.

The GDE with $[Mo_3S_4]^{4+}$ was HOT pressed (130 ˚C and 32 bar for 5 min.) together with a 117 Nafion® membrane and a commercial Pt GDE (IRD Fuel Cell Technology), creating an MEA with a Pt GDE on one side and a $[Mo_3S_4]^{4+}$ GDE on the other side.

2.4.2. Electrochemical measurements of the MEA

The MEA was tested in a fuel cell test setup, where pre-humidified H_2 (99.9999 %) was passed over the GDE's. All measurements were performed at room temperature, with a gas flow of 20 mL/min over both electrodes and at a scan rate of 5 mV/s. The Pt GDE was used as both reference (effectively a NHE electrode) and counter electrode.

2.5. Scanning Tunneling Microscopy (STM)

STM was performed using a Pico SPM instrument (Molecular Imaging Co., USA). Pt/Ir tips (80/20, Ø 0.25 mm) were prepared by electrochemical etching[11]. The sharpness of the tips was checked by recording HOPG images with atomic resolution. $[Mo_3S_4]^{4+}$/HOPG samples were characterized to single-molecule resolution by STM in air.

2.6. X-ray Photoelectron Spectroscopy (XPS)

XPS was performed using a Perkin-Elmer surface analysis system (Physical Electronics Industries Inc., USA). Al-K radiation (1486.6 eV) was used for excitation. High-resolution scans were recorded with a pass energy of 25 eV, a step size of 0.2 eV, and 500 ms/step. Base pressure of the chamber was 10^{-10} Torr. Spectra were calibrated to C 1*s* at 284.5 eV.

3. Results and Discussion

3.1. Electrochemical characterization of $[Mo_3S_4]^{4+}$ in a fuel cell setup

3.1.1 Electrochemical fuel cell behaviour of carbon-supported $[Mo_3S_4]^{4+}$ multi-layers

The $[Mo_3S_4]^{4+}$ were initially deposited on high surface area carbon (xc72), which allowed us to test the electrocatalytic activity in a Membrane Electrode Assembly (MEA). The xc72 is a highly defected high surface area carbon and was chosen to anchor the $[Mo_3S_4]^{4+}$ to defects, eventually creating an MEA with a high dispersion of $[Mo_3S_4]^{4+}$. The MEA was tested in a fuel cell test setup enabling testing for the activity of both the HER and the HOR (hydrogen oxidation reaction). One particular concern of a metal sulfide in an acidic environment (such as Nafion®) is its irreversible oxidation at anodic potentials. However, $[Mo_3S_4]^{4+}$ showed no sign of irreversible oxidation at anodic potentials up to 1 V vs. NHE in the initial electrochemical measurements, Figure 2A. This is in contrast to MoS_2 which is known to oxidize irreversibly at these potentials[32, 33]. We did, however, notice a reversible oxidation feature at 0.73 V vs. NHE that we assign to desorption and re-adsorption of the $[Mo_3S_4]^{4+}$. Cathodic desorption of the $[Mo_3S_4]^{4+}$ has been observed previously in an aqueous solution by Kristensen et al [11]. The fact that we observe a re-adsorption peak, located at 0.65 V vs. NHE in Figure 2A, is most likely due to the slow diffusion of $[Mo_3S_4]^{4+}$ into the electrolyte (Nafion) where desorbed $[Mo_3S_4]^{4+}$ is maintained in close proximity to the electrode unlike the case reported by Kristensen et al. on a sub-monolayer of $[Mo_3S_4]^{4+}$. The desorption/re-adsorption ($[Mo_3S_4]^{4+}$ mobility) scenario is furthermore consistent with our observations that the Nafion membrane used for this study turned green, the same colour as $[Mo_3S_4]^{4+}$ in the H_2SO_4 solution. At anodic potentials we did not measure any evidence of the hydrogen oxidation reaction, see Figure 2A. We did however find that hydrogen was evolved at low cathodic overpotentials (approx. -150 mV). A comparison of the overpotentials is shown in Figure 2B. It is noted that the $[Mo_3S_4]^{4+}$ overpotential is similar to that of nanoparticulate MoS_2 [27, 28]. It should also be noted that the

current at high cathodic potentials decreases for every cathodic sweep while the overpotential remains constant. This could be caused by dissolution or agglomeration of the clusters.

Based on the similarity in overpotentials for the HER, the $[Mo_3S_4]^{4+}$ appear to have an activation barrier for the HER comparable to that of the previously studied MoS_2 system. $[Mo_3S_4]^{4+}$ could thus be a promising electrocatalyst for the HER. However, in order to compare the two systems more directly, studies of well defined $[Mo_3S_4]^{4+}$-samples with known quantity and dispersion are essential, as reported the following section.

3.1.2. Electrochemical preparation and STM imaging of carbon-supported $[Mo_3S_4]^{4+}$ sub-monolayers on HOPG

The preparation of well-dispersed molecular scale catalytic units with minimal agglomeration is critical to all nano-scale materials studied. A significant challenge in the present work was the preparation of an electrode with a high loading of $[Mo_3S_4]^{4+}$-molecules while maintaining independent moieties. HOPG was chosen as the support material as (1) it is an atomically flat substrate suitable for high-resolution (i.e. atomic) mapping by STM and (2), it is electrochemically inert within the potential window under investigation. The strong two-dimensional bonding within the sheets of graphite and inherently low defect density results, however, in rather weak bonding with surface adsorbates, which are typically physisorbed through van der Waals forces only. STM imaging of drop-casted $[Mo_3S_4]^{4+}$ on freshly cleaved HOPG surface thus revealed significant agglomeration with large mounds of $[Mo_3S_4]^{4+}$ (images not shown). High $[Mo_3S_4]^{4+}$ surface mobility presumably results from weak interactions between the adsorbate and the pristine HOPG surface.

In order to prevent surface diffusion of the clusters, we activated a freshly cleaved HOPG surface electrochemically by an anodic pulse procedure developed previously[31]. Surface functional groups such as –OH, –C=O, –COOH which serve to anchor the $[Mo_3S_4]^{4+}$ (by electrostatic interaction or ligand substitution) as well as to improve surface hydrophilicity could be introduced in this way.

Figure 3 shows STM images of this surface after drop-casting an aliquot of the aqueous $[Mo_3S_4]^{4+}/H_2SO_4$ solution. Only insignificant agglomeration is seen. Verifying the predominance of independently adsorbed $[Mo_3S_4]^{4+}$ (approx. 2 nm diameter which includes the H_2O/SO_4^{2-} coordination shell), was a crucial step needed to directly correlate the structure and function of these molecular entities at the level of the single $[Mo_3S_4]^{4+}$-molecule catalyst. Furthermore, STM offered a quantitative measure of the surface coverage, which was determined to be 1.6 ($\pm$ 0.2) x 10^{-11} mol $[Mo_3S_4]^{4+}$ / cm^2 HOPG, corresponding to a surface density of 1.0 ($\pm$ 0.1) x 10^{13} $[Mo_3S_4]^{4+}$-molecules / cm^2.

3.1.3. Electrocatalysis of the HER by a $[Mo_3S_4]^{4+}$ sub-monolayer in a three-electrode cell: Electroatalytic efficiency per single-molecule $[Mo_3S_4]^{4+}$

After STM imaging of the sub-monolayer of $[Mo_3S_4]^{4+}$ on the activated HOPG had established that the sample indeed consisted of a sub-monolayer of independent molecules, exactly the same sample was characterized electrochemically in a three-electrode cell. Figure 4 shows a series of CVs. Hydrogen is evolved in the initial sweeps at more cathodic potentials than -0.15 V vs NHE. This is the same region where the HER on the high surface area carbon supported supported $[Mo_3S_4]^{4+}$ was observed. The Tafel plot in the inset of Figure 4 yields an exchange current density of 2.2 *10^{-7} A/$cm^2_{geometric}$ with a Tafel slope of 120 mV/dec.

The combination of electrochemistry and STM resolved to the level of the single molecule,enables direct conversion to the turnover frequency per molecule. We have previously exploited this combination to assess the number of redox metalloproteins on (bio)electrochemical surfaces[27,28,34,35] .The turnover frequency per $[Mo_3S_4]^{4+}$-molecule was found to be 0.07 s^{-1}. We do not know the exact number of active sites per $[Mo_3S_4]^{4+}$-molecule, but this value is comparable to or even better than the turnover frequency of 0.02^{-1} reported for a single site on the edge of MoS_2 nanoparticles[27]. The turnover frequency is, however, smaller than for the turnover frequency per atom of the archetypical HER catalyst[24] (Pt, Pd). In addition there are many more active atoms on the Pt metal surface than $[Mo_3S_4]^{4+}$

even in a densely packed monolayer. The per molecule activity is, on the other hand larger compared with commonly considered non-precious metal HER catalysts[24], say Ni, Cu or W.

A reduction peak is seen around -0.12 V vs. NHE in the first sweep. This peak could be due to cathodic desorption of $[Mo_3S_4]^{4+}$ as previously proposed[11], but no conclusive evidence exist on the exact nature of this peak.

3.2 XPS data

Spectroscopic evidence of $[Mo_3S_4]^{4+}$ on the surface is crucial, as this ensures that catalytic activity of the $[Mo_3S_4]^{4+}$-molecules is addressed and not that of a contaminant or an oxidized Mo species. XPS holds clues to such assessments. XPS data from both a bulk sample with multilayers of $[Mo_3S_4]^{4+}$to verify that the $[Mo_3S_4]^{4+}$-molecules have the expected electronic structure, and from sub-monolayer $[Mo_3S_4]^{4+}$ evaluated for catalytic activity are compared below.

3.2.1. Bulk $[Mo_3S_4]^{4+}$

XPS data of $[Mo_3S_4]^{4+}$ immobilized on "activated" HOPG offers important insight in the electronic states of the Mo- and S-atoms of the active catalyst molecule. As a reference, XPS of bulk $[Mo_3S_4]^{4+}/SO_4^{2-}$ was first recorded, Figure 5. The deconvoluted Mo 3d, S 2s, and S 2p regions of the XPS spectra of this film are shown in Figures 5A and 5B. Niemantsverdriet et. al[36], reported XPS of $K_5[Mo_3S_4(CN)_9]\cdot 3KCN\cdot 4H_2O$, which contains the same $Mo_3S_4^{4+}$-core, albeit with cyano ligands and potassium cations rather than aqua ligands and sulfate anions. The sulfate anion present in our system gives additional sulfur lines. At first glance these appear to distinguish our spectra from those of[36], but peak deconvolution discloses that the two $[Mo_3S_4]^{4+}$-films are in fact spectroscopically similar (see Table 1).

The energy window shown in Figure 5B, containing overlapping Mo 3d and S 2s transitions, has been deconvoluted into six distinct peaks: S 2s of $[Mo_3S_4]^{4+}$, S 2s of SO_4^{2-}, and two Mo-components leading to two sets of Mo 3d doublets, with a major (84%) and a minor component (16%, shifted 1.75 eV

positive). The S $2p$ lines of $[Mo_3S_4]^{4+}$ and SO_4^{2-}, shown in Figure 5A, are readily distinguished from one another. The lower intensity broad peak at 233.1 eV was assigned to the S $2s$ line in SO_4^{2-}, consistent with reference[37] and verified by XPS experiments in which H_2SO_4 was drop-cast alone onto an HOPG surface (data not shown). This line, not present in the system studied by Niemantsverdriet et. al[36] coincides with the Mo $3d_{3/2}$ line that they assign to $[Mo_3S_4]^{4+}$. Deconvolution of the peaks was undertaken using Gaussian peak shapes and the following data fitting constraints: Splitting: S $2p$=1.19 eV, Mo $3d$=3.15 eV; Intensity ratios: Mo $3d_{3/2}$ = 2/3 × Mo $3d_{5/2}$, S $2p_{1/2}$=0.5 × S $2p_{3/2}$, S $2s([Mo_3S_4]^{4+})$/S $2s(SO_4^{2-})$ = S $2p([Mo_3S_4]^{4+})$/S $2p(SO_4^{2-})$, and finally the Gaussian peak full width half maximum (FWHM) was fixed for the same species in the same energy window (e.g. FWHM Mo $3d_{5/2}$= FWHM Mo $3d_{3/2}$). Apart from the S $2s$ and S $2p$ lines assigned to SO_4^{2-}, and the Mo $3d$ doublet of the minor Mo-component, our data and that of reference[36] are quite similar. The Mo $3d_{5/2}$ line at 229.70 eV indicates that molybdenum is in the formal 4+ state[32], while the S^{2-} ligands of $[Mo_3S_4]^{4+}$, observed as the S $2p$ line at 161.76 eV, is close to the S^{2-} ligands in MoS_2. Only small differences between the spectra reported with thick $Mo_3S_4^{4+}$ film and those in reference[36] are thus found, presumably caused by the different ligands and counter ions. We shall discuss the nature of the minor Mo-component in Section 3.2.2.

3.2.2. XPS: bulk vs. sub-monolayer [Mo₃S₄]⁴⁺

3.2.2. XPS: bulk vs. sub-monolayer $[Mo_3S_4]^{4+}$

XPS of the sub-monolayer $[Mo_3S_4]^{4+}$ on "activated" HOPG was recorded, the survey spectra (not shown) showed no evidence of contamination. Figure 6 shows the deconvoluted S $2p$ spectrum (Figure 6A) which corresponds well with that of bulk $[Mo_3S_4]^{4+}$. The S $2p$ peak of SO_4^{2-} is of lower intensity (relative to the $2p$ of $[Mo_3S_4]^{4+}$) than for bulk $[Mo_3S_4]^{4+}$, this being due to the difference in film preparation. Excess drop-casted reagent (1.8mM $[Mo_3S_4]^{4+}$ in 0.4 M H_2SO_4) was not thoroughly rinsed off in bulk $[Mo_3S_4]^{4+}$-film preparation whereas this was the case for sub-monolayer $[Mo_3S_4]^{4+}$. However, a more notable difference in the XPS is observed for the deconvoluted Mo $3d$ and S $2s$ regions. Compared to the bulk case, two sets of Mo $3d$ doublets are now easily distinguished; the major

(59%) doublet at 230.14 eV and 233.29 eV line up with the Mo $3d_{5/2}$ and Mo $3d_{3/2}$ of bulk $[Mo_3S_4]^{4+}$, while the minor (41%) set of peaks at 232.41 eV and 235.56 eV are shifted by 2.27 eV towards higher binding energies. The intensity of the major set of peaks relative to the minor set of peaks is significantly lower in this sample compared to the bulk sample. We find that the intensity ratio between the set Mo $3d$ peaks (major + minor compontent) and the S $2p$ peak at 162.44 eV, all related to $[Mo_3S_4]^{4+}$, is very similar to the bulk case (Figure 5). This shows that there is no loss of sulfur in the sub-monolayer $[Mo_3S_4]^{4+}$.

The minor, high binding energy Mo $3d$-component we observe in both the sub-monolayer and multilayer sample is not likely due to oxidation of Mo $^{+4}$ to Mo $^{6+}$(say,MoO_3)[32, 33], or due to replacement of S^{2-} ligands in the cluster by O^{2-}, studied by Shibahara et al. for $[Mo_3O_{4-n}S_n]^{4+}$ (n = 0-4) clusters[38]. This is because we obtain near identical sulfur-to-Mo ratio in $[Mo_3S_4]^{4+}$ for the sub-monolayer and multilayer sample although the ratio between major and minor Mo $3d$ component is drastically different. We instead assign the minor Mo $3d$ component to distinct differences in local environment of Mo atoms in the adsorbed $[Mo_3S_4]^{4+}$ structures. Such differences can arise from: (1) lower coordination of the clusters giving rise to a lower final state screening in XPS, (2) a difference in number (concentration) of SO_4^{2-} counter ions, or (3) O adsorption on the clusters. The lower concentration of the minor Mo $3d$ high binding energy component in the multilayer $[Mo_3S_4]^{4+}$-sample compared to the sub-monolayer sample is likely due to the fact that such local environment differences only are found at the outmost surface layer(s) in the multilayer case.

3.2.3. XPS: sub-monolayer $[Mo_3S_4]^{4+}$ *after cyclic voltammetry*

The loss in catalytic activity of $[Mo_3S_4]^{4+}$ on HOPG after voltammetric sweeps, was also investigated by XPS, Figure 7. The S $2p$ and S $2s$ peaks that correspond to SO_4^{2-} were still strongly visible in the XPS spectra recorded subsequent to cyclic voltammetric. The Mo $3d$ and S $2p$ peaks assigned to $[Mo_3S_4]^{4+}$, however, decreased significantly. Little or no Mo is left on the surface.

4. Conclusions and Perspectives

$[Mo_3S_4]^{4+}$-type clusters are long known as a crucial part of polynuclear Mo-S chemistry. $[Mo_3S_4]^{4+}$ is, one example, a prototype cluster in a broader class of $[Mo_3MS_4]^{n+}$ cluster types with a variety of hetero-metal ions. Catalytic $[Mo_3MS_4]^{4+}$-based activity in hydrodesulfurization, N-N cleavage of hydrazine and other organic chemical reactions are notable.

We have introduced $[Mo_3S_4]^{4+}$ as a novel prototype catalyst in heterogeneous catalysis, specifically in the electrocatalytic evolution of hydrogen on different graphite supports of direct relevance to fuel cell electrode surfaces. $[Mo_3S_4]^{4+}$ immobilized on electrode surfaces by electrochemical pulse pre-treatment to create molecular surface functionalities were found, firstly to act as an efficient electrocatalyst for the HER in the electrochemical fuel cell-like environment. The $[Mo_3S_4]^{4+}$-based catalytic efficiency, compares well with the recently reported high electrocatalytic efficiency of identified MoS_2 edge surface sites. The observed catalysis displayed some instability on successive potential scanning but this was largely due to desorption of the catalyst molecules from the surface rather than decomposition, and can be improved on further optimization of the immobilization procedure. Secondly, the unique combination of electrochemistry and STM resolved to the level of the single molecule, could directly convert the catalytic efficiency to the single-molecule scale. In this way the electrocatalytic activity *per molecule* was found to be comparable with that of the edge sites of MoS_2. Through the multifarious and tunable $[Mo_3S_4]^{4+}$-unit extendable to the whole class of heterometallic cluster compounds, these observations have opened novel routes to a new and potentially powerful class of interfacial electrocatalysts useable for one of the altogether most important electrochemical processes, the electrochemical HER reaction.

Our study rests on a comprehensive approach. In addition to cyclic voltammetry, chemical surface immobilization and electrochemical *in situ* STM, we have characterized the electronic properties of the $[Mo_3S_4]^{4+}$ by XPS, used to investigate both bulk and sub-monolayers of $[Mo_3S_4]^{4+}$. XPS of macroscopic $[Mo_3S_4]^{4+}/SO_4^{2-}$ film samples showed the expected majority of 3 $d_{5/2}$ and 3 $d_{3/2}$ spectral peak features for Mo in the formal 4+ oxidation state and a minority of 3 $d_{5/2}$ and 3 $d_{3/2}$ spectral peak features for Mo at higher binding energies as well as the 2 s and 2 $p_{3/2}$ and 2 $p_{1/2}$ S signals. In addition corresponding

signals of the SO_4^{2-} anion were observed. These data showed, interestingly that the $[Mo_3S_4]^{4+}$-core structure is similar to that for a related but different Mo-complex studied by Niemantsverdriet and associates[36].

The sub-monolayers of $[Mo_3S_4]^{4+}$ were found to differ from $[Mo_3S_4]^{4+}$ in the bulk state. The Mo $3d$ peaks at higher binding energies were more pronounced than in the bulk sample indicating that part of the Mo-atoms in the $[Mo_3S_4]^{4+}$ are present in a different local environment. We cannot presently offer a precise rationale for this difference, but the mixed-valence nature of $[Mo_3S_4]^{4+}$ in the (strongly) adsorbed state can be a rationale for the observed electrocatalytic activity. Such "tunable" electronic properties are often prerogatives for efficient electronic transmission in chemical and biological charge transfer processes.

XPS finally substantiated that $[Mo_3S_4]^{4+}$-desorption is the primary cause of the apparent gradual catalytic deactivation on successive voltammetric scanning.

In conclusion, a new class of polynuclear Mo-S cluster-based catalyst has been found to show very high per-molecule catalytic efficiency in the electrochemical HER on carbon-based electrode surfaces. The prototype representative, i.e. the incomplete cubane-type cluster, $[Mo_3S_4]^{4+}$, has been in focus but is otherwise representative of the broader class of homologous heterometallic cubane-type clusters, $[Mo_3MS_4]^{4+}$. Once the observed electrocatalytic stability issue has been rectified, this class may offer new prospects as a broad and electronically versatile class of electrocatalysts in practical working environments.
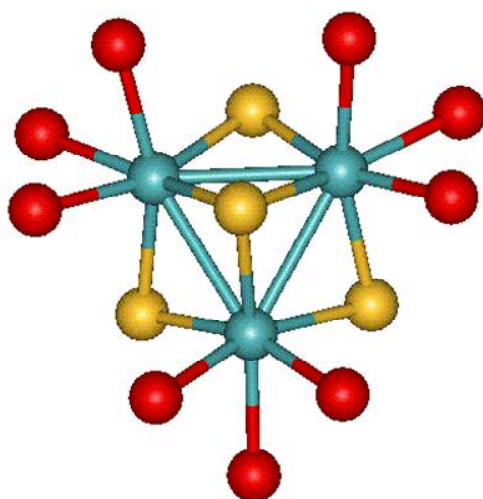
ACKNOWLEDGMENTS

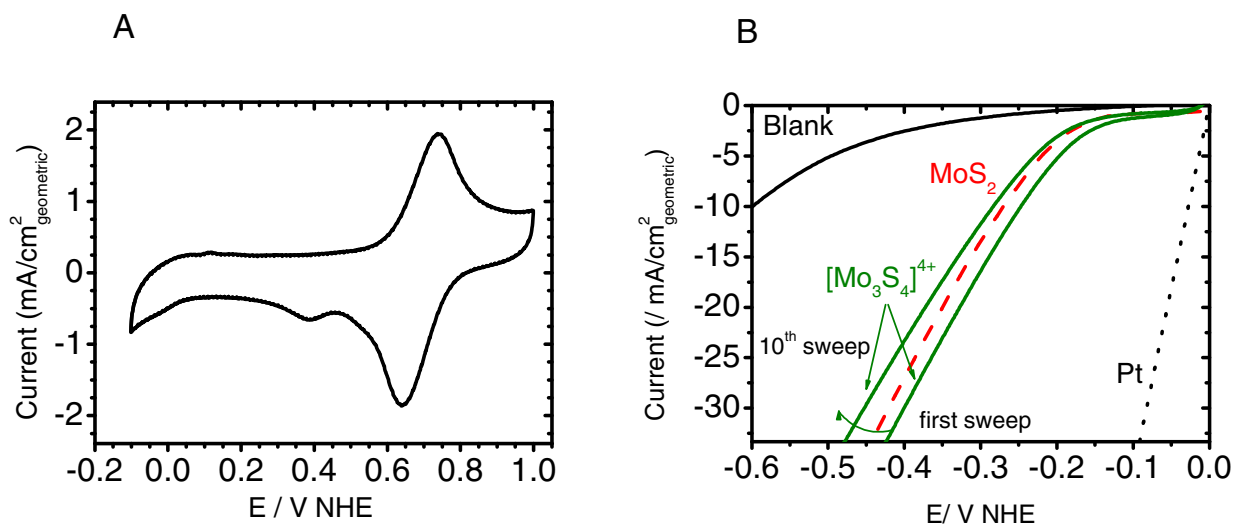**Figure 1:** Molecular structure of $[Mo_3S_4]^{4+}$. Blue (Mo), yellow (S) and red (O from water ligands).

Figure 2: Electrochemical characterization of vulcan xc72 supported $[Mo_3S_4]^{4+}$ in a membrane electrode assembly. The potential is measured with respect to a Pt electrode which serves as both the reference and the counter electrode. A: cyclic voltammogram in the anodic region, showing a reversible oxidation feature at ca. 0.7 V. B: Polarisation curves in the cathodic region where hydrogen is evolved. The activity of $[Mo_3S_4]^{4+}$ is compared with a blank electrode only containing xc72, a sample with Pt and a sample with MoS_2. Hydrogen where passed over both electrodes and the scanrate was 5 mV/s.
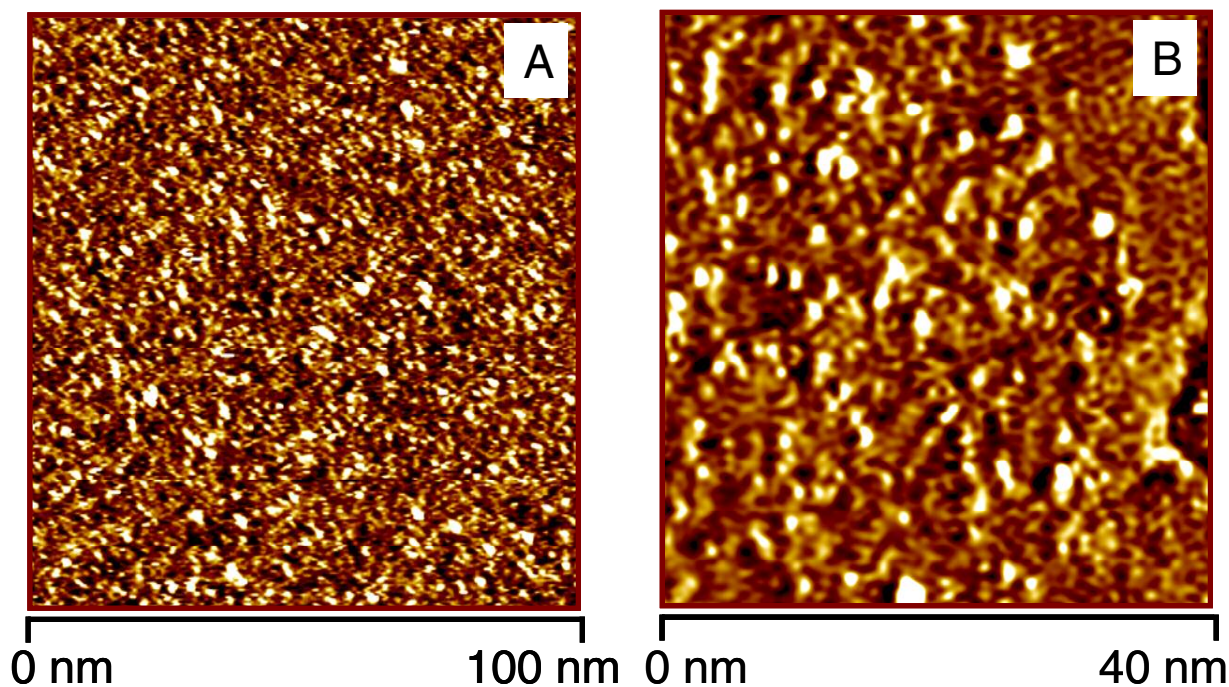
Figure 3: STM image of HOPG supported $[Mo_3S_4]^{4+}$. The coverage of the $[Mo_3S_4]^{4+}$ molecule (most likely including ligands) on HOPG is about 1.0 ($\pm$0.1)x10^{13} molecules /cm^2, corresponding to 1.6 ($\pm$0.2) x 10^{-11} mol/cm^2. Each molecule is ~2.0($\pm$0.5) nm in diameter from STM measurement, and an ideal close packed surface contains ~3.2 ($\pm$0.8)x10^{13} molecules /cm^2 .
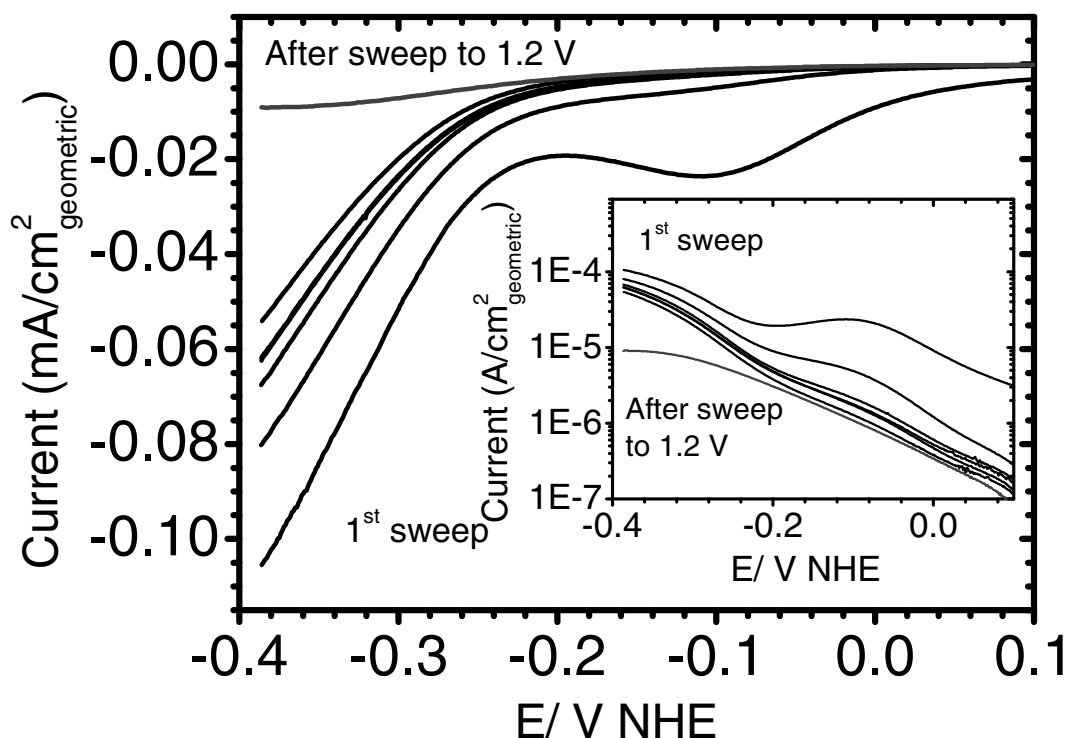

Figure 4: Electrochemical characterization of the submonolayer of $[Mo_3S_4]^{4+}$ on HOPG. Main: Polarization curve in the anodic region showing hydrogen evolution. The decrease in activity is most likely due to anodic desorption of the clusters. After a sweep to high cathodic potentials (1.2 V vs. NHE), the clusters desorb and the activity is only caused by the activated HOPG. Inset: the corresponding Tafel plot. The scanrate was 5 mV/s.
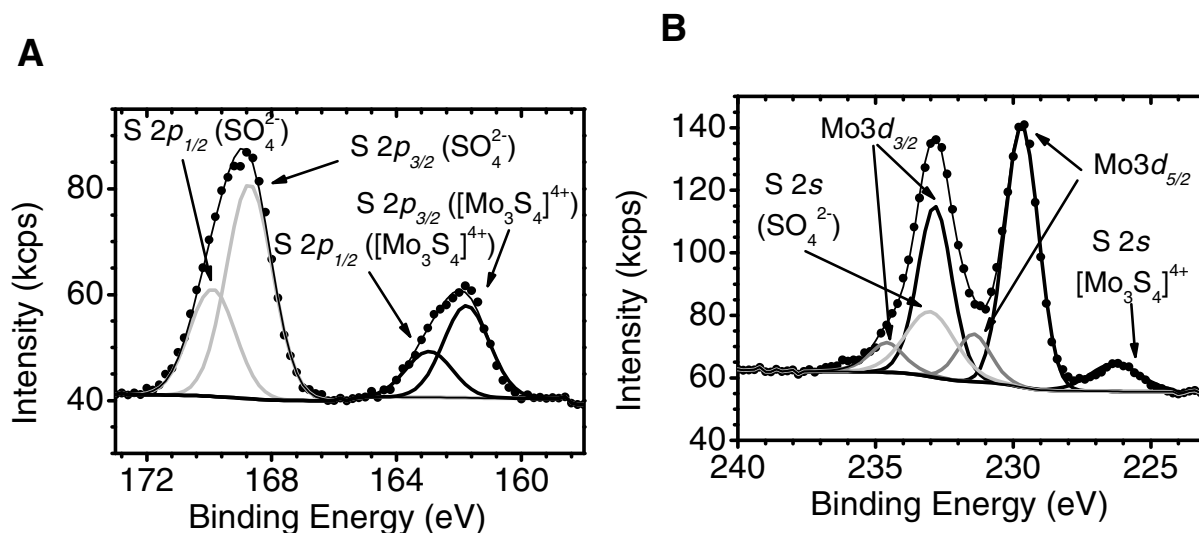
Figure 5: XPS spectra of multilayers of $[Mo_3S_4]^{4+}$ on HOPG. A: The S 2p region of SO_4^{2-} and $[Mo_3S_4]^{4+}$. B: The S 2s of SO_4^{2-} and $[Mo_3S_4]^{4+}$ and the Mo 3d region of $[Mo_3S_4]^{4+}$.
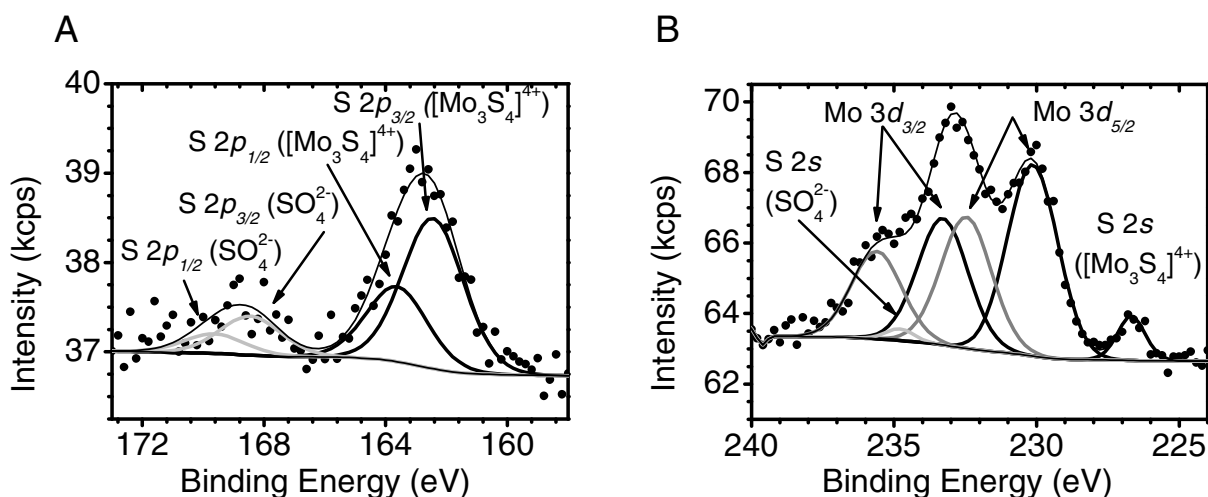

Figure 6: XPS spectra of a submolayer of $[Mo_3S_4]^{4+}$ on HOPG. A: The S 2p region of SO_4^{2-} and $[Mo_3S_4]^{4+}$. B: The S 2s of SO_4^{2-} and $[Mo_3S_4]^{4+}$ and the Mo 3d region of $[Mo_3S_4]^{4+}$.

Figure 7: XPS spectra of a submolayer of $[Mo_3S_4]^{4+}$ on HOPG before (Gray) and after electrochemical measurements (Black). A: The S 2p region of SO_4^{2-} and $[Mo_3S_4]^{4+}$. B: The S 2s of SO_4^{2-} and $[Mo_3S_4]^{4+}$ and the Mo 3d region of $[Mo_3S_4]^{4+}$.
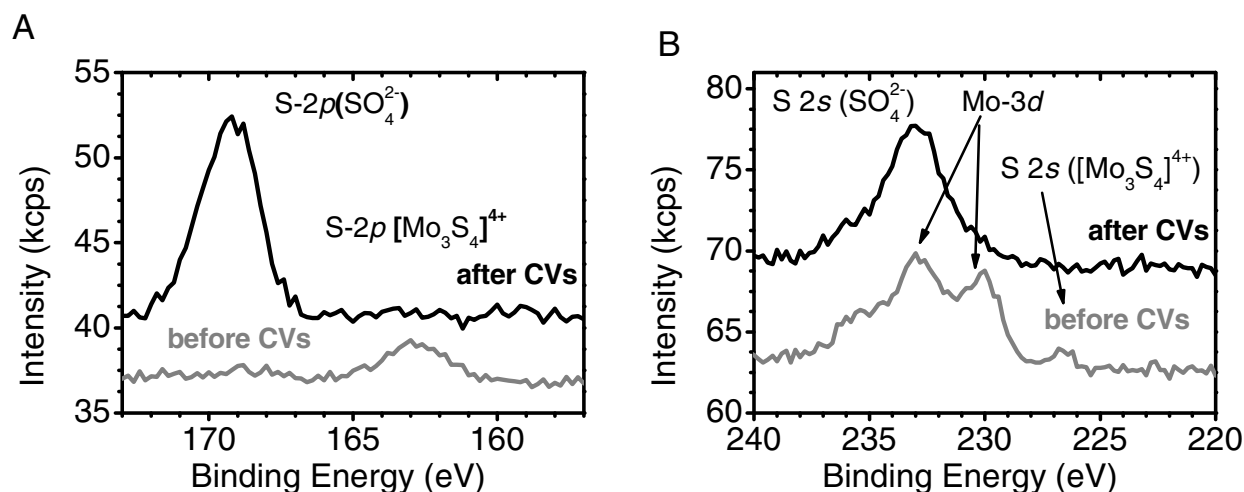
Assigned Species	Spectral Line	FWHM This work (sub monolayer)	Binding Energy (eV) This work (sub-monolayer)	FWHM This work (multi-layer)	Binding Energy (eV) This work (multi-layer)	Binding Energy(eV) Niemantsverdriet[36](values read off raw spectra)
$[Mo_3S_4]^{4+}$	S $2p_{3/2}$	2.36	162.44 ± 0.1	1.74	161.76 ± 0.1	~161.6
$[Mo_3S_4]^{4+}$	S $2p_{1/2}$	2.36	163.63 ± 0.1	1.74	162.95 ± 0.1	~162.6
$[Mo_3S_4]^{4+}$	S $2s$	1.14	226.68 ± 0.1	2.13	226.29 ± 0.1	~226.0
$[Mo_3S_4]^{4+}$	Mo $3d_{5/2}$	2.09	230.14 ± 0.1	1.46	229.70 ± 0.1	~229.3
$[Mo_3S_4]^{4+}$	Mo $3d_{3/2}$	2.09	233.29 ± 0.1	1.46	232.85 ± 0.1	~232.5
SO_4^{2-}	S $2p_{3/2}$	2.36	168.45 ± 0.55	1.74	168.71 ± 0.1	

SO$_4$$^{2-}$	S 2$p_{1/2}$	2.36	169.64 ± 0.55	1.74	169.90 ± 0.1
SO$_4$$^{2-}$	S 2s	1.14	234.80 ± 0.37	2.13	232.99 ± 0.1
[Mo$_3$S$_4$]$^{4+}$ minor	Mo 3$d_{5/2}$	2.09	232.41 ± 0.1	1.46	231.44 ± 0.1
[Mo$_3$S$_4$]$^{4+}$ minor	Mo 3$d_{3/2}$	2.09	235.56 ± 0.1	1.46	234.59 ± 0.1

Table 1: XPS data for a sub-monolayer of [Mo$_3$S$_4$]$^{4+}$ and a "thick", multi-layer [Mo$_3$S$_4$]$^{4+}$ film deposited on HOPG.

Refererences:

(1) Steele, B. C. H.; Heinzel, A. *Nature* **2001**, *414*, 345-352.

(2) Scott, T. A.; Berlinguette, C. P.; Holm, R. H.; Zhou, H. C. *Proc. Natl. Acad. Sci. U. S. A.* **2005**, *102*, 9741-9744.

(3) Lee, S. C.; Holm, R. H. *Chem. Rev.* **2004**, *104*, 1135-1157.

(4) Rao, P. V.; Holm, R. H. *Chem. Rev.* **2004**, *104*, 527-559.

(5) Hernandez-Molina, R.; Sokolov, M. N.; Sykes, A. G.. *Acc. Chem. Res.* **2001**, *34*, 223-230.

(6) Shibahara, T.; Kuroya, H. *Polyhedron* **1986**, *5*, 357-361.

(7) Takei, L.; Dohki, K.; Kobayashi, K.; Suzuki, T.; Hidai, M. *Inorg. Chem.* **2005**, *44*, 3768-3770.

(8) Wakabayashi, T.; Ishii, Y.; Ishikawa, K.; Hidai, M. A *Angewandte Chemie-International Edition in English* **1996**, *35*, 2123-2124.

(9) Taniguchi, M.; Imamura, D.; Ishige, H.; Ishii, Y.; Murata, T.; Hidai, M.; Tatsumi, T. *Journal of Catalysis* **1999**, *187*, 139-150.

(10) Wakabayashi, T.; Ishii, Y.; Murata, T.; Mizobe, Y.; Hidai, M. *Tetrahedron Lett.* **1995**, *36*, 5585-5588.

(11) Kristensen, J.; Zhang, J. D.; Chorkendorff, I.; Ulstrup, J.; Ooi, B. L. *Dalton Transactions* **2006**, , 3985-3990.

(12) Armstrong, F. A. *Curr. Opin. Chem. Biol.* **2005**, *9*, 110-117.

(13) Vincent, K. A.; Parkin, A.; Armstrong, F. A. *Chem. Rev.* **2007**, *107*, 4366-4413.

(14) Hammerich, O.; Ulstrup, J., Eds.; In *Bioinorganic electrochemistry;* Springer: Dordrecht, **2008**; , pp xiv, 310.

(15) Shigehara, K.; Anson, F.C. *J. Phys. Chem.* **1982**, *86*, 2776-2783.

(16) Jiang, R.; Dong, S. *Electrochim. Acta* **1990**, *35*, 1227-1232.

(17) Younathan, J.N.; Wood, K.S.; Meyer, T.J. *Inorg. Chem.* **1992**, *3*1, 3280-3285.

(18) Lei, J.; Ju, H.; Ikeda, O. *Electrochim. Acta* **2004,** 49, 2453-2460.

(19) De Groot, M.T.; Merkx, M.; Wonders, A.H.; Koper , M.T.M. *J. Am. Chem. Soc.* **2005**, *127*, 7579-7586.

(20) Abild-Pedersen, F.; Greeley, J.; Studt, F.; Rossmeisl, J.; Munter, T. R.; Moses, P. G.; Skulason, E.; Bligaard, T.; Nørskov, J. K. *Phys. Rev. Lett.* **2007**, *99*, 016105.

(21) Bligaard, T.; Nørskov, J. K.; Dahl, S.; Matthiesen, J.; Christensen, C. H.; Sehested, J. *Journal of Catalysis* **2004**, *224*, 206-217.

(22) Dresselhaus, M. S.; Thomas, I. L. *Nature* **2001**, *414*, 332-337.

(23) Parsons, R. *Transactions of the Faraday Society* **1958**, *54*, 1053-1063.

(24) Nørskov, J. K.; Bligaard, T.; Logadottir, A.; Kitchin, J. R.; Chen, J. G.; Pandelov, S.; Stimming, U. *J. Electrochem. Soc.* **2005**, *152*, J23.

(25) Greeley, J.; Nørskov, J. K.; Kibler, L. A.; El-Aziz, A. M.; Kolb, D. M. *Chemphyschem* **2006**, *7*, 1032-1035.

(26) Greeley, J.; Jaramillo, T. F.; Bonde, J.; Chorkendorff, I. B.; Nørskov, J. K. *Nature Materials* **2006**, *5*, 909-913.

(27) Jaramillo, T. F.; Jørgensen, K. P.; Bonde, J.; Nielsen, J. H.; Horch, S.; Chorkendorff, I. *Science* **2007**, *317*, 100-102.

(28) Hinnemann, B.; Moses, P. G.; Bonde, J.; Jørgensen, K. P.; Nielsen, J. H.; Horch, S.; Chorkendorff, I.; Nørskov, J. K. *J Am Chem Soc* **2005**, *127*, 5308-5309.

(29) Sakane, G.; Shibahara, T. *Inorganic Syntheses, Vol 33* **2002**, *33*, 144-149.

(30) Martinez, M.; Ooi, B. L.; Sykes, A. G. *J. Am. Chem. Soc.* **1987**, *109*, 4615-4619.

(31) Zhang, J. D.; Chi, Q. J.; Dong, S. J.; Wang, E. K. *Bioelectrochem. Bioenerget.* **1996**, *39*, 267-274.

(32) Bonde, J.; Moses, P. G.; Jaramillo, T. F.; Nørskov, J. K.; Chorkendorff, I. *Submitted Faraday Discuss.* **2008**, .

(33) Jaegermann, W.; Schmeisser, D. *Surface Science,* **1986**, *165*, 143-160.

(34) Chi, Q. J.; Zhang, J. D.; Jensen, P. S.; Christensen, H. E. M.; Ulstrup, J. *Faraday Discuss.* **2006**, *131*, 181-195.

(35) Chi, Q. J.; Farver, O.; Ulstrup, J. *Proc. Natl. Acad. Sci. U. S. A.* **2005**, *102*, 16203-16208.

(36) Muijsers, J. C.; Weber, T.; vanHardeveld, R. M.; Zandbergen, H. W.; Niemantsverdriet, J. W. *Journal of Catalysis* **1995**, *157*, 698-705.

(37) C.D. Wagner, A. V. Naumkin, A. Kraut-Vass, J. W. Allison, C. J. Powerll and J. R. Rumble Jr., *NIST X-Ray Photoelectron Spectroscopy Database, Standard Reference Database 20, Version 3.4* **,2008,** *http://srdata.nist.gov/xps.*

(38) Shibahara, T.; Tsuru, H.; Kuroya, H. *Inorg. Chim. Acta* **1988**, *150*, 167-168.